

Copyright Warning & Restrictions

The copyright law of the United States (Title 17, United States Code) governs the making of photocopies or other reproductions of copyrighted material.

Under certain conditions specified in the law, libraries and archives are authorized to furnish a photocopy or other reproduction. One of these specified conditions is that the photocopy or reproduction is not to be “used for any purpose other than private study, scholarship, or research.” If a user makes a request for, or later uses, a photocopy or reproduction for purposes in excess of “fair use” that user may be liable for copyright infringement,

This institution reserves the right to refuse to accept a copying order if, in its judgment, fulfillment of the order would involve violation of copyright law.

Please Note: The author retains the copyright while the New Jersey Institute of Technology reserves the right to distribute this thesis or dissertation

Printing note: If you do not wish to print this page, then select “Pages from: first page # to: last page #” on the print dialog screen

The Van Houten library has removed some of the personal information and all signatures from the approval page and biographical sketches of theses and dissertations in order to protect the identity of NJIT graduates and faculty.

ABSTRACT

COMPUTATIONAL METHODS FOR TWO-PHASE FLOW WITH SOLUBLE SURFACTANT

by
Kuan Xu

A mathematical model is formulated and solved for the two-phase flow of a viscous drop or inviscid bubble in an immiscible, viscous surrounding fluid in the zero Reynolds number or Stokes flow limit. A surfactant that is present on the interface is also soluble in the exterior fluid, and the drop is deformed by an imposed linear flow. The geometry is two-dimensional and Cartesian.

The dissolved surfactant is considered in the physically realistic limit of large bulk Péclet number. That is, it convects and diffuses as a passive scalar in the bulk flow where the ratio of its convection to diffusion is large. The large bulk Péclet number limit presents a significant challenge for traditional numerical methods, since it implies that large gradients of bulk surfactant concentration can develop in a spatially narrow boundary or transition layer adjacent to the drop interface. The layer structure needs to be resolved accurately so that the bulk-interface surfactant exchange, surface surfactant concentration, and interfacial surface tension can be evaluated to determine the drop's dynamics and evolution.

To resolve this computational difficulty, the dynamics of the transition layer are modeled by a leading order singular perturbation reduction of the conservation law for dissolved surfactant that is derived in the large bulk Péclet number limit.

Two versions of the boundary integral equation for two-phase Stokes flow are presented and used as an underlying fluid solver in the absence of surfactant effects. To evaluate the influence of soluble surfactant the boundary integral solver is coupled to the evolution of surface surfactant concentration and the transition layer equation. The transition layer equation is first solved by a mesh-based numerical method that

has a spectrally accurate equal arc length frame for discretization of the interface and a second order time-step. Results of numerical simulations are presented for a range of different physical parameters. An analytical solution of the transition layer equation by a Green's function representation is also derived, which leads to a second, mesh-free algorithm. Numerical results of the mesh-based and mesh-free methods are compared.

**COMPUTATIONAL METHODS FOR TWO-PHASE FLOW WITH
SOLUBLE SURFACTANT**

by
Kuan Xu

**A Dissertation
Submitted to the Faculty of
New Jersey Institute of Technology and
Rutgers, The State University of New Jersey – Newark
in Partial Fulfillment of the Requirements for the Degree of
Doctor of Philosophy in Mathematical Sciences**

**Department of Mathematical Sciences, NJIT
Department of Mathematics and Computer Science, Rutgers-Newark**

August 2010

Copyright © 2010 by Kuan Xu

ALL RIGHTS RESERVED

APPROVAL PAGE

**COMPUTATIONAL METHODS FOR TWO-PHASE FLOW WITH
SOLUBLE SURFACTANT**

Kuan Xu

Michael Booty, Ph.D., Dissertation Co-Advisor Date
Professor, Department of Mathematical Sciences, NJIT

Michael Siegel, Ph.D., Dissertation Co-Advisor Date
Professor, Department of Mathematical Sciences, NJIT

Lou Kondic, Ph.D., Committee Member Date
Professor, Department of Mathematical Sciences, NJIT

Yuan-Nan Young, Ph.D., Committee Member Date
Associate Professor, Department of Mathematical Sciences, NJIT

David S. Rumschitzki, Ph.D., Committee Member Date
Herbert G. Kayser Professor, Department of Chemical Engineering, the City College
of New York

BIOGRAPHICAL SKETCH

Author: Kuan Xu
Degree: Doctor of Philosophy
Date: August 2010

Undergraduate and Graduate Education:

- Doctor of Philosophy in Mathematical Sciences,
New Jersey Institute of Technology, Newark, New Jersey, 2010
- Bachelor of Science in Mathematics,
Beijing University of Aeronautics and Astronautics, Beijing, China, 2005

Major: Mathematical Sciences

Presentations and Publications:

- K. Xu, M. Booty, and M. Siegel, “A Hybrid Numerical Method for Two-Phase Flow with Soluble Surfactant,” *2010 SIAM Annual Meeting (SIAM-AN10)*, Pittsburgh, PA, July 2010.
- K. Xu, M. Booty, and M. Siegel, “A New Numerical Algorithm for Fluid Interfaces with Soluble Surfactant,” *The Applied Math Days (AMD '10)*, Troy, NY, March 2010.
- K. Xu, M. Booty, and M. Siegel, “Efficient Numerical Computation of Fluid Interfaces with Soluble Surfactant,” *The 62nd Annual Meeting of the American Physical Society's Division of Fluid Dynamics (APS-DFD)*, Minneapolis, MN, November 2009.

Dedicated to

Dr. Tsien Hsue-shen

and

Dr. Kuo Yung-huai

谨以此博士学位论文

献给

钱学森和郭永怀先生

以及我深爱着的中国

ACKNOWLEDGMENT

Professor Michael Booty and Professor Michael Siegel have gone far beyond the call of duty as dissertation advisors. This dissertation could certainly not have been written without them and I am deeply grateful for their guidance, patience, and encouragement through the last few years.

Thanks also to my committee members Professor Lou Kondic, Professor Yuan-Nan Young, Professor Linda Cummings and Professor David Rumschitzki for their significant input and helpful suggestions along the way.

I would like to extend my gratitude to Professor Shidong Jiang for sharing his wide expertise in scientific computation with me and for the intense discussions we engaged in together. I would like to express my gratitude to all the professors whom I took classes from at NJIT, and special thanks go to Professor Wooyoung Choi, Professor Roy Goodman, Professor Peter Petropoulos, Professor Robert Miura, and Professor Gregory Kriegsmann for their excellence in teaching.

I am deeply indebted to Dr. Saland for his advice, patience, and care. In the last fifteen month, he has made me a more resilient person.

I would also like to thank all of the graduate students in the Department of Mathematical Sciences whom I have got to know in the last five years. Thank you to Hui Wu, Zhi Liang, Xinxian Huang, Esmond Siew, Lingyan Cao, Shuchi Agrawal, Manmeet Kaur, Yogesh Joshi, Bhaumik Patel, Matthew Wright, Jacek Wróbel, and Matthew Causley for sharing joy and frustration with me through my graduate life. My friendships with Yu Zhang, Te-Sheng Lin, Chunsheng Yang, Yiming Cheng, Xiaoni Fang, and Qiyi Zhou are so precious and will last forever.

Lian Duan and Jingyuan Cao have been my closest friends for many years; I can not imagine life without their support and encouragement.

Finally, I would like to thank my family for their support and encouragement. I especially thank Xiaonan Wang, my dear cousin, for his endless love and support from all the way across the continent. Mom and Dad, I owe them everything.

TABLE OF CONTENTS

Chapter	Page
1 INTRODUCTION	1
2 MATHEMATICAL FORMULATION	5
2.1 The Governing Equations	5
2.2 Nondimensionalization	9
2.3 The Large Bulk Péclet Number Limit	13
2.4 A Note on the Bulk Péclet Number and Reynolds Number in Some Typical Applications	20
3 THE BOUNDARY INTEGRAL METHOD	24
3.1 The Sherman-Lauricella Formulation	24
3.2 The Primitive Variable Formulation	34
4 NUMERICAL METHOD	38
4.1 Tracking the Motion of the Interface	38
4.1.1 The Equal Arc Length Frame	38
4.1.2 Dealiasing	42
4.2 Spatial Discretization	44
4.2.1 The Boundary Integral Equation	44
4.2.2 The Convection-Diffusion Equation for the Bulk Surfactant Concentration in the Transition Layer	47
4.2.3 The Convection-Diffusion Equation for the Adsorbed Surfactant Concentration on the Interface	50
4.3 Time Marching	51
5 RESULTS OF NUMERICAL SIMULATION	54
6 SOLUTION OF THE TRANSITION LAYER EQUATION VIA A GREEN'S FUNCTION	69
6.1 The Analytical Solution by a Green's Function Representation	70
6.2 Numerical Method	77

TABLE OF CONTENTS
(Continued)

Chapter	Page
6.3 Results and Comparison of Numerical Simulations	85
7 CONCLUDING REMARKS AND FUTURE DIRECTIONS	90
APPENDIX A SHERMAN-LAURICELLA FORMULATION: THE PHYSICAL QUANTITIES IN TERMS OF GOURSAT FUNCTIONS	93
APPENDIX B REMOVABLE SINGULARITIES AND CAUCHY PRINCIPAL VALUE INTEGRALS IN THE BOUNDARY INTEGRAL EQUATIONS	97
REFERENCES	101

LIST OF TABLES

Table	Page
2.1 Surface Tension between Water and Various Fluids in CGS Units at 20°C (To convert to SI units multiply by 10^{-3})	20
2.2 Viscosity Data for Various Fluids in CGS Units at 15°C and One Atmosphere (To convert to SI units multiply μ by 10^{-1} and multiply ν by 10^{-4}) . .	21
2.3 Approximate Values of the Bulk Péclet Number Pe and Reynolds Number Re for a Drop of Radius 0.1 mm Based on the Capillary Velocity and a Typical Bulk Surfactant Diffusivity of $D = 5 \times 10^{-10}$ m ² /sec	22
A.1 Expressions for Physical Quantities in the Exterior Region Ω and Interior Region Ω^i	96

LIST OF FIGURES

Figure	Page	
2.1	A drop with viscosity $\lambda\mu$ is enclosed by fluid of viscosity μ . The unit normal \mathbf{n} on the interface $\partial\Omega$ points from Ω^i to Ω , the unit tangent vector \mathbf{s} points in the direction shown, and θ is the angle measured counter-clockwise positive from the positive x -axis to \mathbf{s} . The curvature $\kappa = -\frac{\partial\theta}{\partial s}$ is positive for a convex shape.	6
2.2	The Eulerian frame has origin O and spatial coordinates x and y . The intrinsic frame has origin O' and spatial coordinates ξ and n	14
3.1	Indentation of the contour $\partial\Omega$, (a) as $z \rightarrow \tau^+$, and (b) as $z \rightarrow \tau^-$. Notice that since $\partial\Omega$ is traversed clockwise in the complex ζ -plane, the orientation on the small indentation is counter-clockwise with respect to τ when $z \rightarrow \tau^+$ and is clockwise with respect to τ when $z \rightarrow \tau^-$. On the indentation, $\zeta = \tau + re^{i\phi}$ where $r \rightarrow 0^+$	31
4.1	The computational domain of the transition layer equation (2.21). A periodic boundary condition is applied in the α -direction and we impose the far-field boundary condition $C = 1$ at an artificial boundary N_f , which is set to $N_f = 20$ in our numerical simulations.	47
5.1	Scenario 1: An inviscid bubble driven by pure straining flow with $Q = 0.25$. The evolution of the bubble interface (left panel) and the surface surfactant concentration (right panel) are plotted from $t = 0$ to $t = 3.0$ in increments of 0.5. The horizontal line in the right panel indicates the initial concentration of the surfactant on the interface.	57
5.2	Scenario 1: Logarithm of the error of bubble area versus time t	58
5.3	Scenario 1: Bubble shape and bulk surfactant concentration C at $t = 1.0$ (upper panel) and $t = 3.0$ (lower panel). $Pe = 4,000$	59
5.4	Scenario 1: Bubble shape and bulk surfactant concentration C at $t = 3.0$ for $Pe = 1,600$ (upper panel) and $Pe = 12,000$ (lower panel).	61
5.5	Scenario 2: A viscous drop in a pure strain with $Q = 0.2$. The interior-exterior viscosity ratio is $\lambda = 0.8$. The evolution of the bubble interface (upper left panel) and the surface surfactant concentration (upper right panel) are shown from $t = 0$ to $t = 8.0$ in increments of 1.0. The horizontal line in the upper right panel indicates the initial surfactant concentration on the interface. The bulk surfactant concentration C at $t = 8.0$ is shown in the lower panel for $Pe = 20,000$	62
5.6	Scenario 2: The logarithm of the error in drop area versus time t	63

LIST OF FIGURES
(Continued)

Figure	Page	
5.7	Scenario 3: An inviscid bubble is stretched by a linear shear flow with shear rate $G = -2B = -0.5$. The evolution of the bubble profile (upper left panel) and the surface surfactant concentration (upper right panel) are shown from $t = 0$ to $t = 4.0$ in increments of 0.5. The lower panel shows the logarithm of the error in drop area versus time t	64
5.8	Scenario 3: Bulk surfactant concentration C at $t = 4.0$ with $Pe = 8,000$. The markers on the interface indicate the location of stagnation points. A cross indicates a stagnation point with converging flow on the interface and a triangle indicates a stagnation point with diverging flow on the interface.	65
5.9	Scenario 4: A viscous drop is stretched by a linear shear flow with shear rate $G = -2B = -1$. The interior-exterior viscosity ratio is 1.2. The evolution of the bubble profile (left panel) and the surface surfactant concentration (right panel) are shown from $t = 0$ to $t = 20.0$ in increments of 1.0. The lower panel shows the logarithm of the error in drop area versus time t	66
5.10	Scenario 4: Bulk surfactant concentration C at $t = 10.0$ (upper panel) and $t = 20.0$ (lower panel) for $Pe = 15,000$. Note the decrease in aspect ratio at later times.	67
6.1	A return to Scenario 1 of Chapter 5. Comparison of simulation results using the Green's function method with simulation using the mesh-based method. The mesh-based method is shown by blue solid lines and the Green's function method is shown by red solid markers. The evolution of the bubble interface (upper left panel) and the surface surfactant concentration (upper right panel) are plotted from $t = 0$ to $t = 3.0$ in increments of 0.5. The lower panel gives a closeup of the spikes in Γ	87
6.2	A return to Scenario 3 of Chapter 5. Comparison of simulation results using the Green's function method with simulation using the mesh-based method. The mesh-based method is shown by blue solid lines and the Green's function method is shown by red solid markers. The evolution of the bubble interface (upper left panel) and the surface surfactant concentration (upper right panel) are plotted from $t = 0$ to $t = 4.0$ in increments of 0.5. The lower panel gives a closeup of the spikes in Γ	89

CHAPTER 1

INTRODUCTION

It is well-established that surfactants, i.e., surface active agents, alter the deformation and breakup of drops by reducing the interfacial tension of fluid-fluid interfaces. This leads to many applications of surfactants, including the synthesis of micron-sized droplets, stabilization of emulsions, and medical treatments for embolisms, to name just a few. In this dissertation the simulations we report are for surfactant effects on drops that are stretched in an imposed flow, which is reminiscent of the classical four-roller mill experiments of G.I. Taylor [45]. However, the geometry is two-dimensional and Cartesian.

There is an extensive literature devoted to the study of drop deformation with a clean interface, i.e., in the absence of surfactant, see for example [8, 44] and the reviews by Acrivos [1] and Rallison [37]. There are also many studies on the influence of surfactant on interfacial flow or multiphase fluid systems where the surfactant is insoluble, see, for instance, [38, 39, 42] and the reviews by Basaran [4], Eggers [15], Quere [36], and Stone [41].

In this dissertation, we consider the effect that the solubility of a surfactant can have on interfacial flow dynamics, that is, where surfactant can be transferred between a fluid interface and the bulk phase. Among the few pioneering works on surfactant solubility, Milliken and Leal [31] studied the influence of soluble surfactant on the deformation and breakup of a viscous drop in a uniaxial extensional flow. They point out that the transfer of surfactant to and from the interface mitigates many of the effects observed with insoluble surfactant by reducing the magnitude of surfactant gradients. They also point out that the dynamics of a fluid interface with soluble surfactant generally lies between that of an interface with insoluble surfactant

and that of an interface that is either clean or has a constant and uniform surfactant coverage. However, in their investigation the transport of surfactant in the bulk phase is assumed to be solely by molecular diffusion with convection neglected. In other words, they consider the limit of fast bulk diffusion or small bulk Péclet number.

In practice, the bulk Péclet number Pe , which measures the ratio of bulk convective to diffusive transport is large, typically 10^5 or larger. At these high values of Pe , a narrow transition layer can form adjacent to the fluid interface across which the surfactant concentration varies rapidly. Accurately resolving the layer is a significant challenge for traditional numerical methods but is essential to evaluate the exchange of surfactant between the interface and bulk flow. Previous studies have either used artificially small Pe , which is physically unrealistic, or finely adapted grids in specific static geometries.

Front tracking [52, 32], diffuse interface [47], and volume of fluid [24] numerical methods have recently been developed to study the effect of soluble surfactant in examples of interfacial flow. These have the computational complexity of an adaptive mesh or the computational expense of a very fine mesh near a fluid interface unless the value of Pe is taken to be artificially small. For time-dependent flow these methods require the computational grid to be re-meshed at each time step, further adding to their complexity and expense.

To overcome these difficulties, Booty and Siegel [7] took advantage of the slenderness of the transition layer, treating it on a different spatial scale from that in the bulk. A separate, singular perturbation analysis of the dynamics in the transition layer combined with an intrinsic surface-fitted orthogonal curvilinear coordinate system allows the transition layer to be resolved. This multiscale approach promises to make a fast and accurate numerical method possible. In [7], the boundary integral formulation via conformal mapping is used to solve the fluid-fluid system with an inviscid interior fluid. In work that is similar to the present study, Tryggvason and

coworkers (private communication) have combined a front tracking numerical method with a boundary layer analysis to study mass transfer in a chemically reacting flow in the limit of large Péclet number.

Among the new contributions of this dissertation relative to the study by Booty and Siegel [7] are: (i) consideration of a two-phase fluid system with arbitrary values of the ratio of interior or drop viscosity to exterior or surrounding fluid viscosity. Although conformal mapping techniques may be applied in this case, they become less efficient relative to their use in the inviscid limit, and this leads us to use the boundary integral method instead. (ii) A complex version of the boundary integral equation using primitive variables is introduced. (iii) Both the underlying fluid solver, for flow without surfactant, and the effects of surfactant and surfactant solubility are solved with spectral accuracy in space using a mesh-based method. (iv) A mesh-free method that is based on a Green's function representation of the bulk surfactant concentration is derived and implemented.

Both the boundary integral method with primitive variables and a complex variable boundary integral method, leading to what is referred to as the Sherman-Lauricella equation, are discussed. We also derive an equivalent complex version of the boundary integral equation with primitive variables that is seen to be closely related to the Sherman-Lauricella equation.

The solution of the Sherman-Lauricella equation closely follows the study of Kropinski [26, 27], which is spectrally accurate in space. The complex version of the primitive variable boundary integral equation that is derived here is also spectrally accurate in space, and we believe it is the first two-dimensional primitive variable formulation of Stokes flow to be so.

In solving for the evolution of the interface with the boundary integral method we use an equal arc length frame, i.e., with marker points equally spaced along the interface. The integrals that occur are evaluated by the Nyström method with

trapezoidal quadrature, which ensures that the numerical computation is spectrally accurate in space. To include the effect of soluble surfactant, we use a mesh-based numerical solution of the transition layer equation with a Chebyshev-Lobatto mesh constructed in the direction normal to the interface.

We also report on an exact solution for the bulk surfactant concentration in the transition layer that is expressed in terms of a Green's function. This offers a solution procedure for the study of solubility effects that is completely free of the need for a volume-filling mesh. A preliminary version of a numerical algorithm using this approach shows potential for the speed-up or improved efficiency in the numerical simulations.

The underlying boundary integral fluid solvers were validated against the work of Siegel [38] for an inviscid bubble with insoluble surfactant and the work of Kropinski [26] and Tanveer and Vasconcelos [44] for a viscous drop in the absence of surfactant.

The dissertation is organized as follows. The problem formulation and governing equations are given in Chapter 2 together with the singular perturbation, large bulk Péclet number limit, transition layer equation. In Section 2.4, we include a brief note on typical values of the bulk Péclet number and Reynolds number in applications. In Chapter 3, the boundary integral method in both primitive variables and the Sherman-Lauricella formulation are discussed. We describe the numerical method in Chapter 4, including the equal arc length frame, the solution of the boundary integral equation, the mesh construction in the transition layer, and the time marching scheme. Numerical results of the mesh-based solution procedure are presented in Chapter 5. In Chapter 6, we introduce a Green's function representation for the solution in the transition layer. In Section 6.2 we describe the numerical algorithm developed to evaluate it, and in Section 6.3 we report on the numerical results given using it. Chapter 7 contains concluding remarks and suggestions for future directions.

CHAPTER 2

MATHEMATICAL FORMULATION

In this chapter, we first formulate the problem both in dimensional and non-dimensional form, then we address the large bulk Péclet number limit.

2.1 The Governing Equations

We consider a fluid drop of viscosity $\lambda\mu$ placed in an exterior or suspending fluid of viscosity μ . Hence λ is the ratio of the viscosity of the drop to the viscosity of the exterior fluid, and when $\lambda = 0$ the interior fluid is of negligible viscosity or inviscid. The drop is neutrally buoyant, that is, we assume that the drop and the exterior fluid have the same density so that the gravitational effects are ignored. We denote the drop or interior region enclosed by the interface by Ω^i and the unbounded exterior region by Ω (see Figure 2.1), while the fluid interface between Ω^i and Ω is denoted by $\partial\Omega$. The geometry is two-dimensional. We follow the convention that the unit normal vector \mathbf{n} on $\partial\Omega$ points from Ω^i to Ω , the unit tangent vector \mathbf{s} on $\partial\Omega$ points in the direction such the interior Ω^i is to the right as $\partial\Omega$ is traversed clockwise, and θ is the angle measured counter-clockwise positive from the positive x -axis to \mathbf{s} .

We take the zero Reynolds number or Stokes flow limit, in which the governing equations for momentum and mass transport in Ω are

$$\begin{aligned}\mu\nabla^2\mathbf{u} &= \nabla p & \mathbf{x} \in \Omega \\ \nabla \cdot \mathbf{u} &= 0,\end{aligned}$$

where \mathbf{u} is the velocity of the exterior fluid and p is its pressure. The flow inside the drop Ω_i is governed similarly by

$$\begin{aligned}\lambda\mu\nabla^2\mathbf{u}^i &= \nabla p^i & \mathbf{x} \in \Omega^i \\ \nabla \cdot \mathbf{u}^i &= 0,\end{aligned}\tag{2.1}$$

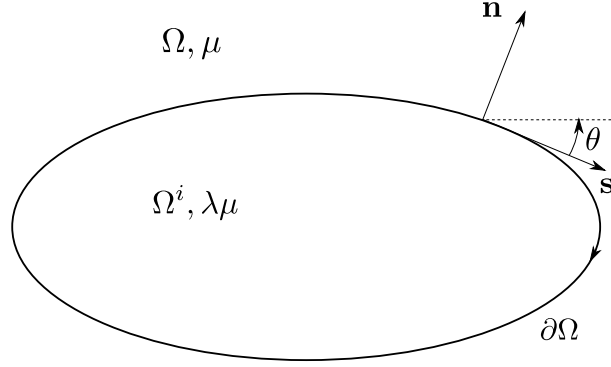


Figure 2.1 A drop with viscosity $\lambda\mu$ is enclosed by fluid of viscosity μ . The unit normal \mathbf{n} on the interface $\partial\Omega$ points from Ω^i to Ω , the unit tangent vector \mathbf{s} points in the direction shown, and θ is the angle measured counter-clockwise positive from the positive x -axis to \mathbf{s} . The curvature $\kappa = -\frac{\partial\theta}{\partial s}$ is positive for a convex shape.

where \mathbf{u}^i denotes the velocity of the interior fluid and p^i is its pressure.

At the interface $\partial\Omega$, the velocity of the interior and exterior fluids is continuous, that is,

$$\mathbf{u}|_{\partial\Omega}(\mathbf{x}, t) = \mathbf{u}^i|_{\partial\Omega}(\mathbf{x}, t) \quad \mathbf{x} \in \partial\Omega.$$

The motion of the interface is also subject to the kinematic condition, that for points \mathbf{x} on the interface

$$\frac{d\mathbf{x}}{dt} = \mathbf{u}(\mathbf{x}, t), \quad \mathbf{x} \in \partial\Omega,$$

so that the velocity of a point on $\partial\Omega$ is equal to the velocity of the fluid at that point. In the inviscid limit, $\lambda = 0$, from the first of equation (2.1), the interior pressure $p^i(t)$ is a function of time t alone, independent of \mathbf{x} , and the interior velocity \mathbf{u}^i is not specified. The condition of continuity of velocity across $\partial\Omega$ is then dropped and the kinematic condition alone is applied.

The stress-balance boundary condition on $\partial\Omega$ can be written as

$$-(p - p^i)\mathbf{n} + 2\mu(\mathbf{e} - \lambda\mathbf{e}^i) \cdot \mathbf{n} = \sigma\kappa\mathbf{n} - \nabla_{\mathbf{s}}\sigma, \quad \mathbf{x} \in \partial\Omega, \quad (2.2)$$

where \mathbf{e} is the rate-of-strain tensor, whose entries are

$$e_{ij} = \frac{1}{2} \left(\frac{\partial u_i}{\partial x_j} + \frac{\partial u_j}{\partial x_i} \right),$$

and κ is the local curvature of the interface $\partial\Omega$. Here σ is the surface tension, which depends on the adsorbed or surface concentration of surfactant Γ through an equation of state which we write in general as

$$\sigma = \sigma(\Gamma).$$

The presence of surfactant reduces surface tension and two specific choices for the equation of state that are widely used are the Langmuir equation and a linearized version of the Langmuir equation. The more precise models for the equation of state, such as the Langmuir equation

$$\sigma = \sigma_0 + RT\Gamma_\infty \ln \left(1 - \frac{\Gamma}{\Gamma_\infty} \right), \quad (2.3)$$

have a nonlinear dependence of σ on Γ . Here σ_0 is the surface tension of a clean or surfactant-free interface and R , T , and Γ_∞ are, respectively, the universal gas constant, uniform temperature, and the maximum monolayer packing concentration of the surface surfactant concentration. The linearized version of (2.3) for small Γ is

$$\sigma = \sigma_0 - RT\Gamma_\infty$$

The last term on the right hand side of (2.2) is called the Marangoni stress and is due to the non-zero spatial gradient of the interfacial surface tension that is caused when the distribution of the adsorbed surfactant on the interface is not spatially uniform.

We consider the case when the surfactant is soluble, that is, it can dissolve in the bulk flow away from the interface, where it is transported as a passive scalar. We take the surfactant to be soluble only in Ω , without much loss of generality, so that

the surfactant concentration C in the bulk satisfies

$$\frac{\partial C}{\partial t} + \mathbf{u} \cdot \nabla C = D \nabla^2 C \quad \mathbf{x} \in \Omega,$$

where D is the surfactant's diffusivity in the bulk flow.

The evolution of surfactant that is adsorbed on the interface Γ is governed by the convection-diffusion equation

$$\frac{\partial \Gamma}{\partial t} \Big|_{\xi} - \frac{\partial \mathbf{X}}{\partial t} \Big|_{\xi} \cdot \nabla_{\mathbf{s}} \Gamma + \nabla_{\mathbf{s}} \cdot (\Gamma \mathbf{u}_{\mathbf{s}}) + \Gamma \kappa u_n = D_s \nabla_{\mathbf{s}}^2 \Gamma + D \mathbf{n} \cdot \nabla C|_{\partial \Omega} \quad \mathbf{x} \in \partial \Omega, \quad (2.4)$$

where $\nabla_{\mathbf{s}}$ is the surface gradient, $\mathbf{u}_{\mathbf{s}}$ is the projection of the flow velocity vector onto the tangent plane at the interface, $u_n = \mathbf{u} \cdot \mathbf{n}$ is the normal component of velocity of the interface, $\mathbf{x} = \mathbf{X}(\xi, t)$ is a parametric representation of the interface, and D_s denotes the surfactant's surface diffusivity [50]. On the left hand side of equation (2.4), the first two terms together ensure that if the interface moves then the time derivative of Γ is taken in the direction normal to the interface, while the next two terms account for the change in surfactant concentration due to advective flux along the interface and due to change in area of the interface caused by motion along its normal. The first term on the right hand side represents the change in Γ due to surface diffusion, while the second term accounts for the transfer or exchange of surfactant between its dissolved form in the bulk flow immediately adjacent to the interface $\partial \Omega$ and its adsorbed form on the interface.

In fact, exchange of surfactant between the bulk phase and interface is a two-step process [14]. In the bulk, surfactant is transported relative to material particles on the interface by diffusion, while exchange between the bulk and the interface occurs via adsorption-desorption kinetics. The combination of these two steps is the net flux

$$j = \kappa_a(\Gamma_{\infty} - \Gamma)C|_{\partial \Omega} - \kappa_d \Gamma = D \mathbf{n} \cdot \nabla C|_{\partial \Omega},$$

where κ_a and κ_d are the kinetic rate coefficients for the adsorption and desorption processes, respectively.

In the far-field, we assume that the bulk surfactant concentration approaches a constant reference value

$$C \rightarrow C_\infty, \quad \text{as } |\mathbf{x}| \rightarrow \infty. \quad (2.5)$$

We impose a boundary condition at infinity that corresponds to an arbitrary imposed linear flow field,

$$\mathbf{u} = \begin{pmatrix} Q_\infty & B_\infty - G_\infty/2 \\ B_\infty + G_\infty/2 & -Q_\infty \end{pmatrix} \cdot \mathbf{x} + O(|\mathbf{x}|^{-2}) \quad \text{as } |\mathbf{x}| \rightarrow \infty. \quad (2.6)$$

Here G_∞ is the vorticity of the imposed flow, while Q_∞ and B_∞ characterize its strain rate.

2.2 Nondimensionalization

There are two ways to non-dimensionalize the problem, which differ by the choice of the characteristic velocity scale U . One choice is to set $U = \alpha_\infty a_0$, where a_0 is a well-defined length scale which we take to be the radius of an unstrained circular drop of the same area and α_∞ is a well-defined measure of the imposed strain rate given in terms of the coefficients Q_∞ , B_∞ , and G_∞ in (2.6). Another choice is to choose the intrinsic velocity scale of the capillary force $U = \sigma_0/\mu$. In this dissertation we make the latter choice, and note that the dimensionless problem resulting from one choice of U can be mapped to the other by a simple rescaling. The present choice for U follows that of Siegel [38], Kropinski [26, 27], and Tanveer and Vasconcelos [44].

The governing equations and boundary conditions are made non-dimensional by setting

$$\begin{aligned} \mathbf{x} &= a_0 \tilde{\mathbf{x}}, & \mathbf{u} &= U \tilde{\mathbf{u}} = \frac{\sigma_0}{\mu} \tilde{\mathbf{u}}, & p &= \frac{\sigma_0}{a_0} \tilde{p}, \\ \sigma &= \sigma_\infty \tilde{\sigma}, & t &= \frac{a_0 \mu}{U} \tilde{t} = \frac{a_0 \mu}{\sigma_0} \tilde{t}, & \Gamma &= \Gamma_\infty \tilde{\Gamma}, & C &= C_\infty \tilde{C}, \end{aligned}$$

and a tilde denotes that a quantity is dimensionless. When tildes on dimensionless quantities are dropped, the dimensionless version of the Stokes equations becomes

$$\nabla^2 \mathbf{u} = \nabla p, \quad \nabla \cdot \mathbf{u} = 0 \quad \mathbf{x} \in \Omega, \quad (2.7a)$$

$$\lambda \nabla^2 \mathbf{u}^i = \nabla p^i, \quad \nabla \cdot \mathbf{u}^i = 0 \quad \mathbf{x} \in \Omega^i. \quad (2.7b)$$

The influence of gravity is neglected here. It may be important for the dynamics of an inviscid or nearly inviscid bubble that is sufficiently large, and the neglect of gravity is justified in the limit when the Bond number $Bo = \sigma_0 / (\rho g a_0^2)$ is large. That is, when the ratio of the buoyancy force on the bubble, $\rho g a_0^3$ is small relative to typical surface tension forces $\sigma_0 a_0$.

The non-dimensional stress-balance boundary condition becomes

$$-(p - p^i) \mathbf{n} + 2(\mathbf{e} - \lambda \mathbf{e}^i) \cdot \mathbf{n} = \sigma \kappa \mathbf{n} - \nabla_{\mathbf{s}} \sigma \quad \mathbf{x} \in \partial\Omega \quad (2.8)$$

where we note that our choice of orientation of the tangent vector \mathbf{s} and the angle θ implies that for a convex drop the curvature $\kappa = -\frac{\partial\theta}{\partial s} > 0$. In dimensionless form, the different forms that we consider for the equation of state are

$$\sigma = \begin{cases} 1 + E \ln(1 - \Gamma) & \text{the Langmuir equation of state} \\ 1 - E\Gamma & \text{a linear equation of state} \end{cases}. \quad (2.9)$$

Here, $E = RT\Gamma_\infty / \sigma_0$ is the elasticity parameter, which is a dimensionless measure of the sensitivity of surface tension to adsorbed surfactant concentration.

The surfactant concentration C in the bulk flow is governed by

$$\frac{\partial C}{\partial t} + \mathbf{u} \cdot \nabla C = \frac{1}{Pe} \nabla^2 C \quad \mathbf{x} \in \Omega, \quad (2.10)$$

where the bulk Péclet number $Pe = Ua_0/D$ is the ratio of advective to diffusive transport effects in the bulk.

In dimensionless form, the equation for the surface concentration of surfactant is

$$\left. \frac{\partial \Gamma}{\partial t} \right|_{\xi} - \left. \frac{\partial \mathbf{X}}{\partial t} \right|_{\xi} \cdot \nabla_{\mathbf{s}} \Gamma + \nabla_{\mathbf{s}} \cdot (\Gamma \mathbf{u}_{\mathbf{s}}) + \Gamma \kappa u_n = \frac{1}{Pe_s} \nabla_{\mathbf{s}}^2 \Gamma + J \mathbf{n} \cdot \nabla C|_{\partial \Omega}, \quad (2.11)$$

where the surface Péclet number $Pe_s = Ua_0/D_s$. The dimensionless parameter $J = DC_{\infty}/U\Gamma_{\infty}$ can be written

$$J = \frac{DC_{\infty}/a_0}{U\Gamma_{\infty}/a_0}$$

and is therefore a measure of the diffusive flux for exchange of surfactant between the bulk and interface relative to the convective flux of adsorbed surfactant on the interface. The parameter J can be thought of as measuring the efficiency of the exchange or transfer of surfactant between the bulk and the interface relative to transport on the interface.

The net flux of surfactant exchange between the interface and the bulk in dimensionless form is

$$J \mathbf{n} \cdot \nabla C|_{\partial \Omega} = Bi(K(1 - \Gamma)C|_{\partial \Omega} - \Gamma). \quad (2.12)$$

In (2.12), the dimensionless parameter $K = \kappa_a C_{\infty}/\kappa_d$ is an equilibrium partition coefficient and the Biot number $Bi = a_0 \kappa_d/U$ is the ratio of the time scale of the flow a_0/U to the time scale of the kinetic desorption process $1/\kappa_d$. In this dissertation, we take the limit $Bi \rightarrow \infty$, which is realistic in practice, and is referred to as the diffusion-controlled regime. In this limit, the time scale for adsorption-desorption

kinetics is much less than the time scale of the flow, so that the surface exchange kinetics are effectively in equilibrium. This implies the boundary condition

$$C|_{\partial\Omega} = \frac{\Gamma}{K(1 - \Gamma)}, \quad (2.13)$$

for C at the interface, which is the equilibrium adsorption relation of the Langmuir isotherm. From (2.5) the dimensionless form of the boundary condition for C in the far-field is

$$C \rightarrow 1 \quad \text{as} \quad |\mathbf{x}| \rightarrow \infty. \quad (2.14)$$

If we also prescribe the initial distribution of C to be spatially uniform and in equilibrium with this far-field value, we have the initial data for C

$$C(\mathbf{x}, 0) = 1 \quad \text{for} \quad \mathbf{x} \in \Omega. \quad (2.15)$$

The dimensionless form of the kinematic condition at the interface is

$$\frac{d\mathbf{x}}{dt} = \mathbf{u}(\mathbf{x}, t) \quad \mathbf{x} \in \partial\Omega, \quad (2.16)$$

while the boundary condition at infinity now reads

$$\mathbf{u}^\infty = \begin{pmatrix} Q & B - G/2 \\ B + G/2 & -Q \end{pmatrix} \cdot \mathbf{x} + O(|\mathbf{x}|^{-2}) \quad \text{as} \quad |\mathbf{x}| \rightarrow \infty, \quad (2.17)$$

where the dimensionless parameters Q , G , and B are given by

$$Q = \frac{a_0 Q_\infty}{U} = \frac{a_0 Q_\infty \mu}{\sigma_0}, \quad B = \frac{a_0 B_\infty}{U} = \frac{a_0 B_\infty \mu}{\sigma_0}, \quad G = \frac{a_0 G_\infty}{U} = \frac{a_0 G_\infty \mu}{\sigma_0}.$$

Two typical examples of the linear far-field flow that we will use for numerical simulation are:

(i) Pure Strain or Hyperbolic Flow

When $B = G = 0$, the dimensionless far-field boundary condition is

$$\mathbf{u} = Q(x_1, -x_2) + O(|\mathbf{x}|^{-2}) \quad \text{as } |\mathbf{x}| \rightarrow \infty,$$

where Q is the capillary number, or equivalently a dimensionless imposed strain rate. This imposed flow is referred to as a pure strain, a uniaxial extension, or a hyperbolic flow.

(ii) Simple Shear

A simple shear flow is given by setting $Q = 0$ and $G = -2B \neq 0$. Then the boundary condition at infinity is

$$\mathbf{u} = -G(x_2, 0) + O(|\mathbf{x}|^{-2}) \quad \text{as } |\mathbf{x}| \rightarrow \infty,$$

where G is a capillary number, or equivalently the dimensionless shear rate. When $G > 0$, the vorticity of the imposed flow is $\boldsymbol{\omega} = \nabla \wedge \mathbf{u} = \langle 0, 0, G \rangle$, which is in the direction of the positive x_3 axis.

2.3 The Large Bulk Péclet Number Limit

In applications, the bulk Péclet number can be as large as 10^5 to 10^6 . When the bulk Péclet number Pe has such a large value a narrow transition layer in the bulk surfactant concentration C can develop adjacent to the interface. The layer has spatial width of order $Pe^{-1/2}$ in which the normal gradient of C is large. In this section we use the analysis due to Booty and Siegel [7] with slight modification to accommodate the current 2D geometry. To analyze the dynamics within the transition layer it is convenient to introduce an intrinsic or surface-fitted orthogonal curvilinear coordinate system (ξ, n) that is attached to the moving interface for all time (see Figure 2.2). Here

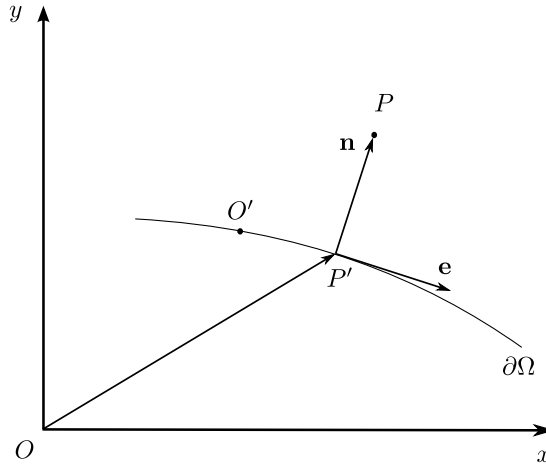


Figure 2.2 The Eulerian frame has origin O and spatial coordinates x and y . The intrinsic frame has origin O' and spatial coordinates ξ and n .

the ξ -direction is tangential to $\partial\Omega$ and n is distance along the normal measured from $\partial\Omega$. The transformation between Eulerian coordinates \mathbf{x} and intrinsic coordinates is uniquely invertible sufficiently close to $\partial\Omega$ provided $\partial\Omega$ is smooth. Analysis based on intrinsic coordinates attached to a moving surface has been used before, for example, in Matalon et al. [29] and Yao and Stewart [51].

Here we review the transformation of the material derivative, and quote results for other operators. The origin of the Eulerian and intrinsic coordinate systems are O and O' , respectively, and the position vector \mathbf{x} of a point P in space relative to O is written in the two coordinate systems as

$$\mathbf{x} = \mathbf{X}(\xi, t) + n\mathbf{n}(\xi, t)$$

where $\mathbf{X} = \overrightarrow{OP'}$ is the position vector relative to O of the projection, P' , of P onto $\partial\Omega$ in the direction of the unit normal \mathbf{n} , so that $\partial\Omega$ has equation $\mathbf{x} = \mathbf{X}(\xi, t)$. The unit vector \mathbf{e} tangential to $\partial\Omega$ in the direction of increasing ξ is $\mathbf{e} = \frac{1}{a} \frac{\partial \mathbf{X}}{\partial \xi}$ where $a = \left| \frac{\partial \mathbf{X}}{\partial \xi} \right|$. It is a fundamental result in differential geometry that, with t fixed, $\frac{\partial \mathbf{n}}{\partial \xi} = \kappa \frac{\partial \mathbf{X}}{\partial \xi}$, which

is referred to as Rodrigues' formula. The change in \mathbf{x} corresponding to increments in the intrinsic coordinates (ξ, n) with time fixed is therefore

$$d\mathbf{x} = l d\xi \mathbf{e} + dn \mathbf{n}, \text{ where } l = a(1 + n\kappa).$$

The convention for \mathbf{n} and \mathbf{e} implies that the curvature κ is positive when the curve is convex on the side to which \mathbf{n} points, and is negative otherwise, equivalently $\kappa = -\frac{\partial\theta}{\partial s}$.

With P fixed relative to O , the time derivative in the Eulerian frame transforms as

$$\frac{\partial}{\partial t} \mapsto \frac{\partial}{\partial t} + \mathbf{q} \cdot \nabla_t + \frac{\partial n}{\partial t} \frac{\partial}{\partial n}. \quad (2.18)$$

Here ∂_t on the right hand side is in the moving frame, i.e., with intrinsic coordinates fixed,

$$\nabla_t = \frac{1}{l} \frac{\partial}{\partial \xi} \mathbf{e}$$

is the projection of the gradient onto the tangent plane at P , and

$$\mathbf{q} = l \frac{\partial \xi}{\partial t} \mathbf{e},$$

so that \mathbf{q} is the velocity of P relative to O' projected onto the tangent plane at P . Since P is fixed relative to O , this is also $\mathbf{q} = -\mathbf{U}_s$, where \mathbf{U}_s is the velocity of O' relative to O projected onto the tangent plane at P . Also, $-\frac{\partial n}{\partial t}$ is the normal speed of the surface $\partial\Omega$ relative to O in the direction of \mathbf{n} , which was written earlier in (2.4) as u_n .

The fluid velocity \mathbf{u} at an arbitrary point P in the Eulerian frame is written in terms of its projection onto the tangent plane \mathbf{u}_t and its component in the normal direction u_p as $\mathbf{u} = \mathbf{u}_t + u_p \mathbf{n}$. The gradient operator is written similarly as $\nabla = \nabla_t + \mathbf{n} \frac{\partial}{\partial n}$, so that $\mathbf{u} \cdot \nabla = \mathbf{u}_t \cdot \nabla_t + u_p \frac{\partial}{\partial n}$. As $n \rightarrow 0$ and $\partial\Omega$ is approached the surface quantities are recovered, so that with the same notation as in equations (2.4),

$\mathbf{u}_t \rightarrow \mathbf{u}_s$, $u_p \rightarrow u_n$ and $\nabla_t \rightarrow \nabla_s$. Then from equation (2.18) the material derivative transforms as

$$\frac{D}{Dt} \mapsto \frac{\partial}{\partial t} + \mathbf{v}_t \cdot \nabla_t + v_p \frac{\partial}{\partial n},$$

where $\mathbf{v}_t = \mathbf{u}_t - \mathbf{U}_s$ is the fluid velocity relative to O' projected onto the tangent plane at P and $v_p = u_p - u_n$ is the normal component of the fluid velocity relative to $\partial\Omega$.

In the interface-attached intrinsic frame, equation (2.10) for the transport of surfactant in the bulk flow is therefore

$$\frac{\partial C}{\partial t} + \mathbf{v}_t \cdot \nabla_t C + v_p \frac{\partial C}{\partial n} = \epsilon^2 \nabla_s^2 C, \quad (2.19)$$

where $\epsilon = Pe^{-1/2}$ and the Laplacian ∇_s^2 is expressed in intrinsic coordinates. In the limit of large Pe , i.e., small ϵ , the bulk surfactant concentration C in the narrow transition layer adjacent to $\partial\Omega$ depends on a local normal coordinate N , where $n = \epsilon N$ and $N = O(1)$ as $\epsilon \rightarrow 0$. While $C = C(\xi, N, t; \epsilon)$ within the layer, there is no mechanism available to support a similar separation of spatial scales for the fluid velocity, so that $\mathbf{v} = \mathbf{v}_t + v_p \mathbf{n} = \mathbf{v}(\xi, n, t; \epsilon)$.

An approximate equation for the evolution of C within the layer is given by keeping only the leading terms in an expansion for small ϵ . In this approximation, the tangential velocity \mathbf{v}_t is replaced by its value on $\partial\Omega$,

$$\mathbf{v}_s = \mathbf{u}_s - \mathbf{U}_s \quad (2.20)$$

which is of order $O(1)$ except, for example, near stagnation points on the surface, and ∇_t is replaced by ∇_s . Since $\partial\Omega$ is a fluid interface, the kinematic condition implies that v_p vanishes on $\partial\Omega$, so that it is replaced by the first non-zero term of its Taylor expansion, $\epsilon N \partial_n v_p|_s$ where the normal derivative $\partial_n v_p|_s$ is evaluated on $\partial\Omega$. The small $O(\epsilon)$ estimate in size of this coefficient in equation (2.19) multiplies the normal

gradient of C , which is approximated by $(1/\epsilon)\partial_N C(\xi, N, t; 0)$. In a similar way, the small diffusion coefficient of equation (2.19) is magnified by the Laplacian of C within the layer, so that the right hand side of (2.19) is approximated by $\partial_N^2 C(\xi, N, t; 0)$. The reduced equation that results for the evolution of a first approximation to C within the layer is therefore

$$\frac{\partial C}{\partial t} + \mathbf{v}_s \cdot \nabla_s C + \frac{\partial v_p}{\partial n} \Big|_{\partial\Omega} N \frac{\partial C}{\partial N} = \frac{\partial^2 C}{\partial N^2}. \quad (2.21)$$

Consideration of higher order terms in the expansion implies that the error in approximating C by the solution of this equation is of order $O(\epsilon)$ as $\epsilon \rightarrow 0$.

The large Pe limit implies that outside the transition layer $(\partial_t + \mathbf{u} \cdot \nabla)C = 0$ to within $O(\epsilon)$, so that to this order C is constant on particle paths. The initial condition (2.15), which holds for all \mathbf{x} then implies that $C \equiv 1$ outside the transition layer for all time, so that (2.21) has initial, boundary and matching conditions

$$\begin{aligned} C(\xi, N, 0) &= 1, & C|_{N=0} &= \frac{\Gamma}{K(1-\Gamma)}, \\ C(\xi, N, t) &\rightarrow 1 \text{ as } N \rightarrow \infty, & t &> 0. \end{aligned} \quad (2.22)$$

At a first glance, the coefficient $\partial_n v_p|_s$ in equation (2.21) appears to require the evaluation of off-surface data to compute the normal derivative. However, from the incompressibility condition $\nabla \cdot \mathbf{u} = 0$ written in the orthogonal curvilinear, intrinsic frame

$$\frac{1}{a} \frac{\partial}{\partial \xi} ((1 + n\kappa)u_t) + \frac{\partial}{\partial n} ((1 + n\kappa)u_p) = 0$$

where u_t is the magnitude of the tangential velocity \mathbf{u}_t , i.e., $\mathbf{u}_t = u_t \mathbf{e}$ and $u_p = v_p + u_n$. When the incompressibility condition is evaluated in the limit as $n \rightarrow 0$, the first term tends to the surface divergence $\nabla_s \cdot \mathbf{u}_s$, and since the normal speed u_n of the surface is independent of n , so that $\partial_n u_p = \partial_n v_p$, the condition implies that

$$\frac{\partial v_p}{\partial n} \Big|_{\partial\Omega} = -\kappa u_n - \nabla_s \cdot \mathbf{u}_s, \quad (2.23)$$

where the right hand side contains surface data alone.

The transfer coefficient J in the bulk-interface surfactant exchange term $J\mathbf{n}\cdot\nabla C|_{\partial\Omega}$ is rescaled by putting $J = \epsilon J_0$ where $J_0 = O(1)$, so that in equation (2.4) for conservation of adsorbed surfactant the exchange term remains $O(1)$ when expressed in terms of the rescaled coordinate N . The equation becomes

$$\left.\frac{\partial\Gamma}{\partial t}\right|_{\xi} - \left.\frac{\partial\mathbf{X}}{\partial t}\right|_{\xi} \cdot \nabla_s\Gamma + \nabla_s \cdot (\Gamma\mathbf{u}_s) + \Gamma\kappa u_n = \frac{1}{Pe_s}\nabla_s^2\Gamma + J_0 \left.\frac{\partial C}{\partial N}\right|_{\partial\Omega}. \quad (2.24)$$

The initial boundary value problem (2.21) and (2.22) for C within the transition layer and the rescaled bulk-interface exchange term of (2.24) have been constructed by a leading order, singular perturbation rescaling of the full equations in the limit $Pe \rightarrow \infty$. As a result, the expansion parameter Pe does not appear in the rescaled model. In the remainder of this dissertation, we will consider the rescaled model and numerical methods that are designed for its solution.

Treatment of the equation for bulk surfactant transport in the large bulk Péclet number Pe limit by the singular perturbation approach just described is a central theme of this thesis. We note, however, that the surface diffusion of adsorbed surfactant, which is represented by the term $Pe_s^{-1}\nabla_s^2\Gamma$ in equation (2.24), does not require the same sort of treatment. Further, although its influence can be included in the analysis and simulations we present its influence is considered to be sufficiently small that it will be neglected. In short, although it is important to treat the term $Pe^{-1}\nabla^2C$ in equation (2.10) with care we reason here that the term $Pe_s^{-1}\nabla_s^2\Gamma$ in equation (2.24) can safely be neglected.

To explain this, we note first that the surface diffusivity of surfactant D_s is considered to be a difficult quantity to measure accurately, since it is difficult to isolate the effect of surface diffusion from other effects in an experiment, but the data in the study [11] by Chang and Franses, which is believed to be among the most accurate available, indicates that surface diffusivities D_s and bulk diffusivities D are

approximately equal, and typically about 5×10^{-10} m²/sec. This implies that values of the inverse surface and bulk Péclet numbers, Pe_s^{-1} and Pe^{-1} respectively, are also similar, and as explained in more detail in the note of Section 2.4 below with typical values given in Table 2.3, these are in the range 10^{-7} to 0.25×10^{-4} .

The difference in treatment of the bulk and surface diffusive effects hinges on the different orders of magnitude of $\nabla^2 C$ and $\nabla_s^2 \Gamma$. Large first and second order derivatives of C in the direction normal to the interface are to be expected since both Pe^{-1} is small and the on-surface value of $C|_{N=0} = \Gamma/K(1 - \Gamma)$ and the far-field value $C = 1$ as $N \rightarrow \infty$ of (2.22) are generally not equal. The singular perturbation method accounts for and resolves these large gradients using what is primarily an analytic approach.

On the other hand, large gradients of the surface surfactant concentration Γ are not expected to develop, that is $\nabla_s^2 \Gamma$ is never large, so that the smallness of Pe_s^{-1} implies the surface diffusion effect can be neglected. The main effect that mitigates against large surface gradients of Γ occurring is the Marangoni stress. The elasticity parameter $E = |\partial_\Gamma \sigma|_{\Gamma=0}$ typically lies in the range (0.3, 0.5) and this is sufficiently large that if an appreciable surface gradient of Γ develops the surface gradient of surface tension, i.e., Marangoni stress, that accompanies it is sufficiently large to act and it acts in the direction that tends to reduce the gradients. An additional effect that can also act to reduce surface gradients in Γ is surfactant solubility, since it provides a mechanism whereby surfactant can leave and then re-enter the interface by desorption and adsorption at the interface and transport through the bulk.

2.4 A Note on the Bulk Péclet Number and Reynolds Number in Some Typical Applications

The bulk Péclet number Pe , which appears in equation (2.10), and the Reynolds number Re are defined by

$$Pe = \frac{Ua_0}{D} \quad \text{and} \quad Re = \frac{Ua_0}{\nu},$$

respectively. As mentioned at the beginning of Section 2.2, the velocity scale $U = \sigma_0/\mu$ is the capillary velocity of a surfactant-free interface, where μ is the viscosity, sometimes called the molecular or dynamic viscosity, of the exterior fluid. In the definition of Pe , D is the bulk surfactant diffusivity, and in the definition of Re , ν is the kinematic viscosity of the exterior fluid. It is worth noting that the ratio

$$\frac{Re}{Pe} = \frac{D}{\nu} = \frac{1}{Sc}$$

where $Sc = \nu/D$ is the Schmidt number.

The length scale a_0 is the radius of the equivalent unstretched or circular drop, and is an extrinsic quantity. It appears in the definition of Pe and Re , and both are directly proportional to a_0 . On the other hand, the velocity scale U and the ratio of Re to Pe are intrinsic properties of the fluid system. That is, they depend only on the choice of the interior and exterior immiscible fluids and the soluble surfactant, not on a_0 .

Table 2.1 Surface Tension between Water and Various Fluids in CGS Units at 20°C (To convert to SI units multiply by 10^{-3})

	olive oil	benzene	CCl_4	light mineral oil
σ_0 dyn/cm	20	35	45	52.5

Table 2.1 shows data for the clean surface tension σ_0 between water and common sample liquids, and Table 2.2 shows data for the viscosity μ and kinematic viscosity ν . The data is taken from [5], except in the case of the light mineral oil, for which data is taken from [2] for the specific oil used in the microfluidic device of the experiments described there. In this case, the data we give for ν is based on the data of [2] for μ and our estimate for the density of 0.9 gm/cm^3 .

The data imply a capillary velocity U in the range from 20 m/sec for a drop of olive oil in water to 50 m/sec for light mineral oil in water. This is decreased if the oil is the exterior or matrix fluid to give a capillary velocity of 0.2 m/sec for a drop of water in olive oil or 1.25 m/sec for water in light mineral oil.

Table 2.2 Viscosity Data for Various Fluids in CGS Units at 15°C and One Atmosphere (To convert to SI units multiply μ by 10^{-1} and multiply ν by 10^{-4})

	water	olive oil	CCl_4	light mineral oil
$\mu \text{ } 10^{-2} \text{ gm/cm sec}$	1.1	99	1.0	40
$\nu \text{ } 10^{-2} \text{ cm}^2/\text{sec}$	1.1	108	0.65	44

Data for the diffusivity of various surfactants in water that are believed to be in the diffusion-controlled regime are given in Table 2.2 of [11]. This includes data for both ionic and nonionic surfactants, and surfactants that are classified either as alcohols or detergents. The value given for the bulk diffusivity D does not vary much over the nineteen different surfactant species for which data is given. Most values of D are reported as being between $2 \times 10^{-10} \text{ m}^2/\text{sec}$ and $8 \times 10^{-10} \text{ m}^2/\text{sec}$, with a very small number of data around $10^{-9} \text{ m}^2/\text{sec}$ being considered unreliable and a typical figure of $5 \times 10^{-10} \text{ m}^2/\text{sec}$ suggested as representative. We adopt this representative value of $D = 5 \times 10^{-10} \text{ m}^2/\text{sec}$ here for the surfactant diffusivity in the aqueous medium.

This implies a value for the ratio $Re/Pe = D/\nu$ that ranges from 5×10^{-4} when the exterior fluid is water to 1.1×10^{-5} or 5×10^{-6} when the exterior fluid is light mineral oil or olive oil, respectively. We note briefly that in the latter two cases, since the data for D is for surfactant that is soluble in the aqueous phase, the surfactant is dissolved in the drop or interior fluid, and this is not the set-up for which we consider the dynamics in this dissertation - we consider the surfactant to be soluble in the exterior phase alone.

To fix values of Pe and Re we need to choose a value of the undisturbed drop radius or length scale a_0 . Although any value of a_0 that is much greater than the molecular scale, near which the approximations of continuum mechanics begin to fail, can be chosen, we choose a specific value of a_0 equal to 0.1 mm (i.e., 100 μm) as sufficiently small not to give unrealistically large values of Pe and to be about the smallest drop size that would be visible to the unaided eye. This gives values for the bulk Péclet number Pe in the range from 4×10^4 for a drop of water in olive oil to 10^7 for a drop of light mineral oil in water.

Table 2.3 Approximate Values of the Bulk Péclet Number Pe and Reynolds Number Re for a Drop of Radius 0.1 mm Based on the Capillary Velocity and a Typical Bulk Surfactant Diffusivity of $D = 5 \times 10^{-10}$ m²/sec

	water in olive oil	water in light mineral oil	olive oil in water	light mineral oil in water
Pe	4×10^4	2.5×10^5	4×10^6	10^7
Re/Pe	5×10^{-6}	1.1×10^{-5}	5×10^{-4}	
Re	0.2	2.8	2×10^3	5×10^3

Data for Pe , the ratio Re/Pe , and Re are given in Table 2.3. From this it is seen that the bulk Péclet number can be considered as large across the chosen range of typical fluid systems, but the Reynolds number is only small or moderate when oil

is the suspending fluid and is in fact quite large for a drop of oil in water. Nonetheless, we will proceed with the zero Reynolds number or Stokes flow limit of the momentum equation, bearing in mind that there are applications where it does not apply.

CHAPTER 3

THE BOUNDARY INTEGRAL METHOD

The Boundary Integral Method (BIM) is generally recognized as one of the most accurate and efficient fluid solvers for linearized Navier-Stokes flow. In this chapter, we discuss two different versions of the boundary integral method, including their formulation and solvability. The first one, termed the Sherman-Lauricella formulation uses complex variables and is referred to as an indirect method, while the second version is a traditional formulation by primitive variables which is a direct method and is more widely used. We show that the primitive variable formulation is equivalent to another complex variable formulation, which can facilitate its numerical computation.

3.1 The Sherman-Lauricella Formulation

The classical Sherman-Lauricella integral equation and its solution have been widely used in problems of static elasticity in 2D and, to the best of our knowledge, were first introduced to solve Stokes' equations for fluid flow by Greengard et al. [19]. Here we follow the slightly later development due to Kropinski [26, 27] but with some modifications.

Let the velocity of the exterior flow be $\mathbf{u} = (u_1, u_2)$ and the velocity of the interior flow be $\mathbf{u}^i = (u_1^i, u_2^i)$, then we introduce a stream function for each region, so that

$$\begin{aligned}(u_1, u_2) &= (W_{x_2}, -W_{x_1}) \quad \mathbf{x} \in \Omega, \\(u_1^i, u_2^i) &= (W_{x_2}^i, -W_{x_1}^i) \quad \mathbf{x} \in \Omega^i.\end{aligned}$$

Since the formulation in both regions is similar, we focus on the exterior region Ω and only give the analogous results for the interior region as needed. The curl of equation

(2.7a) implies that

$$\nabla^4 W = 0 \quad \mathbf{x} \in \Omega,$$

that is, $W(x_1, x_2)$ is a biharmonic function. Similarly $W^i(x_1, x_2)$ is biharmonic on Ω^i .

The stream function $W(x_1, x_2)$, therefore has a Goursat representation, that is,

$$W(x_1, x_2) = \text{Re}(\bar{z}f(z) + h(z)), \quad z \in \Omega,$$

where $f(z)$ and $h(z)$ are analytic functions of the complex variable $z = x_1 + ix_2$ on Ω , [10, 30]. The functions $f(z)$ and $g(z) = h'(z)$ are known as Goursat functions. Then

$$W^i(x_1, x_2) = \text{Re}(\bar{z}f^i(z) + h^i(z)), \quad z \in \Omega^i,$$

where $f^i(z)$ and $h^i(z)$, with $g^i(z) = h^{i'}(z)$, are analytic on Ω^i .

All physical quantities in the exterior and interior regions can be expressed in terms of the Goursat functions on their respective domains, see, for example, [26] or the derivation in Appendix A. For example, the velocity is given by

$$-u_2 + iu_1 = f(z) + z\overline{f'(z)} + \overline{g(z)} \quad z \in \Omega, \quad (3.1a)$$

$$-u_2^i + iu_1^i = f^i(z) + z\overline{f^{i'}(z)} + \overline{g^i(z)} \quad z \in \Omega^i. \quad (3.1b)$$

The vorticity and pressure are given by

$$q + ip = -4f'(z) \quad z \in \Omega, \quad (3.2a)$$

$$q^i + i\frac{p^i}{\lambda} = -4f^{i'}(z) \quad z \in \Omega^i, \quad (3.2b)$$

where we note the factor λ dividing the interior pressure p^i . In the rate of strain tensors, we have

$$e_{11} + ie_{12} = -e_{22} + ie_{21} = -i\left(z\overline{f''(z)} + \overline{g'(z)}\right) \quad z \in \Omega \quad (3.3a)$$

$$e_{11}^i + ie_{12}^i = -e_{22}^i + ie_{21}^i = -i\left(z\overline{f^{i''}(z)} + \overline{g^{i'}(z)}\right) \quad z \in \Omega^i. \quad (3.3b)$$

The left hand side of equation (3.2a) can be evaluated as $|z| \rightarrow \infty$ by using the far-field behavior of the velocity field (2.17). This implies that the vorticity $q = G + O(|z|^{-3})$ and that the pressure $p = p_\infty + O(|z|^{-3})$ as $z \rightarrow \infty$ and where the ambient pressure p_∞ can be set to zero without loss of generality. Then

$$f(z) = -\frac{G}{4}z + H_1(t) + O(|z|^{-2}) \quad \text{as } |z| \rightarrow \infty, \quad (3.4)$$

where $H_1(t)$ is as yet an arbitrary function of time. From (2.17), in terms of its components, the behavior of the velocity at infinity is

$$\begin{aligned} u_1 &= Qx_1 + \left(B - \frac{G}{2}\right)x_2 + O(|z|^{-2}), \\ u_2 &= \left(B + \frac{G}{2}\right)x_1 - Qx_2 + O(|z|^{-2}). \end{aligned} \quad (3.5)$$

Next, the far-field behavior of $f(z)$ at (3.4) and the velocity at (3.5) give the far-field behavior of $g(z)$ via the representation (3.1a) for the velocity in terms of the Goursat functions. Specifically,

$$g(z) = -z(B + iQ) - \overline{H_1(t)} + O(|z|^{-2}) \quad \text{as } |z| \rightarrow \infty.$$

In presentations of the Sherman-Lauricella integral equation in the literature, at this stage the Goursat functions are written in terms of Cauchy-type integrals that contain a single complex density $\omega(z)$, which is only defined on the interface $\partial\Omega$, where the integrals give the modification to the imposed far-field flow that is caused by the presence of the drop. In [18] the authors note that “the choice of such a representation is not obvious, but is analogous to the more familiar single and double layer potentials used in the solution of Laplace’s equation”. The representation that has been used by a number of authors including Kropinski [26] is such that, if we

introduce

$$f^o(z) = \frac{1}{2\pi i} \int_{\partial\Omega} \frac{\omega(\zeta, t)}{\zeta - z} d\zeta - \frac{Gz}{4} + H_1(t), \quad (3.6a)$$

$$g^o(z) = \frac{1}{2\pi i} \int_{\partial\Omega} \frac{-\overline{\omega(\zeta, t)} d\zeta + \omega(\zeta, t) d\bar{\zeta}}{\zeta - z} - \frac{1}{2\pi i} \int_{\partial\Omega} \frac{\bar{\zeta}\omega(\zeta, t)}{(\zeta - z)^2} d\zeta - z(B + iQ) - \overline{H_1(t)}, \quad (3.6b)$$

then the Goursat functions are given by

$$(f(z), g(z)) = (f^o(z), g^o(z)) \quad \text{when } z \in \Omega, \quad (3.7)$$

$$(f^i(z), g^i(z)) = (f^o(z), g^o(z)) \quad \text{when } z \in \Omega^i. \quad (3.8)$$

Here z is an arbitrary point in the complex plane away from the interface $\partial\Omega$ and ζ is the variable of integration around the interface. In the definition (3.6a) and (3.6b), $\int_{\partial\Omega}$ can denote integration around $\partial\Omega$ in either the counter-clockwise direction, as is the usual convention in the complex plane, or clockwise, the difference can be resolved simply by changing the sign of $\omega(z)$. In this dissertation, we choose the latter, i.e., clockwise direction. Here and elsewhere, the time dependence of $\omega(\zeta, t)$ and $H_1(t)$ is indicated, while the time dependence of the Goursat functions $f(z)$ and $g(z)$ is not indicated but is taken to be understood, and a prime denotes $\frac{d}{dz}$. Recall that time enters the problem only via the time derivatives in the kinematic condition (2.16) and in the equation for surface and bulk concentration of surfactant (2.11) and (2.10), and, as we may also choose, parametrically via the parameters Q , B , and G of the boundary condition at infinity (2.17).

From the Cauchy-type integrals in the definitions (3.6a) and (3.6b), we see that the Goursat functions are analytic functions of z except for z on the contour $\partial\Omega$. They are also singular as $z \rightarrow \infty$ to accommodate the imposed linear flow.

In terms of Cartesian components we put $\mathbf{n} = (n_1, n_2)$ and $\mathbf{s} = (s_1, s_2)$, then the stress-balance boundary condition (2.8) implies

$$- (p - p^i) n_1 + 2 (e_{1j} - \lambda e_{1j}^i) n_j = \sigma \kappa n_1 - \frac{\partial \sigma}{\partial s} s_1, \quad (3.9a)$$

$$- (p - p^i) n_2 + 2 (e_{2j} - \lambda e_{2j}^i) n_j = \sigma \kappa n_2 - \frac{\partial \sigma}{\partial s} s_2. \quad (3.9b)$$

Adding (3.9a) to i times (3.9b) we have

$$\begin{aligned} & -p(n_1 + in_2) + 2(e_{1j} + ie_{2j})n_j - [-p^i(n_1 + in_2) + 2\lambda(e_{1j}^i + ie_{2j}^i)n_j] \\ & = \sigma \kappa (n_1 + in_2) - \frac{\partial \sigma}{\partial s} (s_1 + is_2). \end{aligned} \quad (3.10)$$

If we consider the first two terms on the left hand side of this last equation, recalling that $e_{11} = -e_{22}$ and $e_{12} = e_{21}$, we have the following sequence of manipulations

$$\begin{aligned} & -p(n_1 + in_2) + 2(e_{1j} + ie_{2j})n_j \\ & = -p(n_1 + in_2) + 2(e_{11}n_1 + e_{12}n_2 + ie_{21}n_1 + ie_{22}n_2) \\ & = -p(n_1 + in_2) + 2(e_{11} + ie_{12})(n_1 - in_2) \\ & = 4 \operatorname{Im}(f'(z))n - 2i \left(z \overline{f''(z)} + \overline{g'(z)} \right) \bar{n} \\ & = -2i \left(f'(z) - \overline{f'(z)} \right) n - 2i \left(z \overline{f''(z)} + \overline{g'(z)} \right) \bar{n} \\ & = 2 \left[\left(f'(z) - \overline{f'(z)} \right) \tau_s - \left(z \overline{f''(z)} + \overline{g'(z)} \right) \overline{\tau_s} \right] \\ & = 2 \frac{\partial}{\partial s} \left(f(z) - z \overline{f'(z)} - \overline{g(z)} \right), \end{aligned} \quad (3.11)$$

where τ denotes a point on the interface $\partial\Omega$ and s is arc length. Here we have introduced the Goursat functions using equations (3.2a) and (3.3a), and we have then used the fact that with the present choice of orientation the unit normal and tangent vectors \mathbf{n} and \mathbf{s} are associated with their complex counterparts $n = n_1 + in_2$ and $s_T = s_1 + is_2$, with $s_T = \frac{\partial \tau}{\partial s} = -in$. In evaluating (3.11) on the interface, the limit is to be taken as $z \rightarrow \tau^+$, i.e., as the field point z approaches the interface from

the domain Ω of the exterior fluid. An analogous sequence of steps applies to the last two terms on the left hand side of equation (3.10), but where a factor λ appears multiplying (3.11), and the limit is to be taken as $z \rightarrow \tau^-$, i.e., as the interface is approached from the domain Ω^i of the interior fluid.

$$-p^i (n_1 + in_2) + 2\lambda (e_{1j}^i + ie_{2j}^i) n_j = 2\lambda \frac{\partial}{\partial s} \left(f^i(z) - z\overline{f^{i'}(z)} - \overline{g^i(z)} \right), \quad (3.12)$$

Let us now consider the right hand side of (3.10). The Frenet-Serret formula $\frac{\partial \mathbf{s}}{\partial s} = -\kappa \mathbf{n}$ in complex form is

$$\frac{\partial s_T}{\partial s} = \tau_{ss} = -\kappa n,$$

which allows us to simplify the right hand side as

$$\begin{aligned} & \sigma \kappa (n_1 + in_2) - \frac{\partial \sigma}{\partial s} (s_1 + is_2) \\ &= -\sigma \tau_{ss} - \frac{\partial \sigma}{\partial s} \tau_s \\ &= -\frac{\partial}{\partial s} (\tau_s \sigma). \end{aligned} \quad (3.13)$$

At this point, the stress-balance boundary condition (2.8), or its complex variable form (3.10) becomes

$$\frac{\partial}{\partial s} \left[\lim_{z \rightarrow \tau^+} \left(f(z) - z\overline{f'(z)} - \overline{g(z)} \right) - \lambda \lim_{z \rightarrow \tau^-} \left(f^i(z) - z\overline{f^{i'}(z)} - \overline{g^i(z)} \right) \right] = -\frac{1}{2} \frac{\partial}{\partial s} (\tau_s \sigma).$$

So that an integration with respect to s gives

$$\lim_{z \rightarrow \tau^+} \left(f(z) - z\overline{f'(z)} - \overline{g(z)} \right) - \lambda \lim_{z \rightarrow \tau^-} \left(f^i(z) - z\overline{f^{i'}(z)} - \overline{g^i(z)} \right) = -\frac{\tau_s \sigma}{2} + H_2(t), \quad (3.14)$$

where $H_2(t)$ is a constant of integration which depends on time t alone.

Substituting the representations for $f(z)$ and $g(z)$ of (3.7), (3.6a), and (3.6b) into the terms of the first limit in (3.14), we have

$$\begin{aligned}
& f(z) - z\overline{f'(z)} - \overline{g(z)} \\
&= \frac{1}{2\pi i} \int_{\partial\Omega} \frac{\omega(\zeta, t)}{\zeta - z} d\zeta - \frac{1}{2\pi i} \int_{\partial\Omega} \frac{\omega(\zeta, t)}{\bar{\zeta} - \bar{z}} d\bar{\zeta} + \frac{1}{2\pi i} \int_{\partial\Omega} \frac{\overline{\omega(\zeta, t)}}{\bar{\zeta} - \bar{z}} d\zeta \\
&+ \frac{1}{2\pi i} \int_{\partial\Omega} \frac{(z - \zeta)\overline{\omega(\zeta, t)}}{(\bar{\zeta} - \bar{z})^2} d\bar{\zeta} + \bar{z}(B - iQ) + 2H_1(t). \tag{3.15}
\end{aligned}$$

This contains Cauchy-type integrals that appear to be singular when z approaches the interface from either side, but the singularities are integrable. To see this, we list four preliminary results. If we let a point z that is away from the contour approach a point τ on the contour, then

$$\lim_{z \rightarrow \tau^+} \frac{1}{2\pi i} \int_{\partial\Omega} \frac{\omega(\zeta)}{\zeta - z} d\zeta = \frac{1}{2}\omega(\tau) + \frac{1}{2\pi i} \int_{\partial\Omega} \frac{\omega(\zeta)}{\zeta - \tau} d\zeta \tag{3.16a}$$

$$\lim_{z \rightarrow \tau^-} \frac{1}{2\pi i} \int_{\partial\Omega} \frac{\omega(\zeta)}{\zeta - z} d\zeta = -\frac{1}{2}\omega(\tau) + \frac{1}{2\pi i} \int_{\partial\Omega} \frac{\omega(\zeta)}{\zeta - \tau} d\zeta \tag{3.16b}$$

$$\lim_{z \rightarrow \tau^+} \frac{1}{2\pi i} \int_{\partial\Omega} \frac{\omega(\zeta)}{\bar{\zeta} - \bar{z}} d\bar{\zeta} = -\frac{1}{2}\omega(\tau) + \frac{1}{2\pi i} \int_{\partial\Omega} \frac{\omega(\zeta)}{\bar{\zeta} - \bar{\tau}} d\bar{\zeta} \tag{3.16c}$$

$$\lim_{z \rightarrow \tau^-} \frac{1}{2\pi i} \int_{\partial\Omega} \frac{\omega(\zeta)}{\bar{\zeta} - \bar{z}} d\bar{\zeta} = \frac{1}{2}\omega(\tau) + \frac{1}{2\pi i} \int_{\partial\Omega} \frac{\omega(\zeta)}{\bar{\zeta} - \bar{\tau}} d\bar{\zeta} \tag{3.16d}$$

where $\int_{\partial\Omega}$ denotes a principal value integral. In writing the results (3.16a-3.16d), we note that the indentation of $\partial\Omega$ around τ is as shown in Figure 3.1. We remark here that identities (3.16a) and (3.16b) are exactly the Plemelj formulae, from which one can deduce (3.16c) and (3.16d) by taking the complex conjugate.

Using (3.16a) and (3.16c), we find that the first two integrals on the right hand side of (3.15) contain non-zero local contributions from the indentation of the contour as ζ passes τ . However, the last two Cauchy-type integrals in (3.15) make no local contribution from the indentation of the contour. To see this, we let $\zeta = \tau + re^{i\phi}$, then

$$\frac{d\zeta}{\zeta - \bar{\tau}} = ie^{2i\phi} d\phi \qquad \frac{(\tau - \zeta)d\bar{\zeta}}{(\bar{\zeta} - \bar{\tau})^2} = ie^{2i\phi} d\phi \tag{3.17}$$

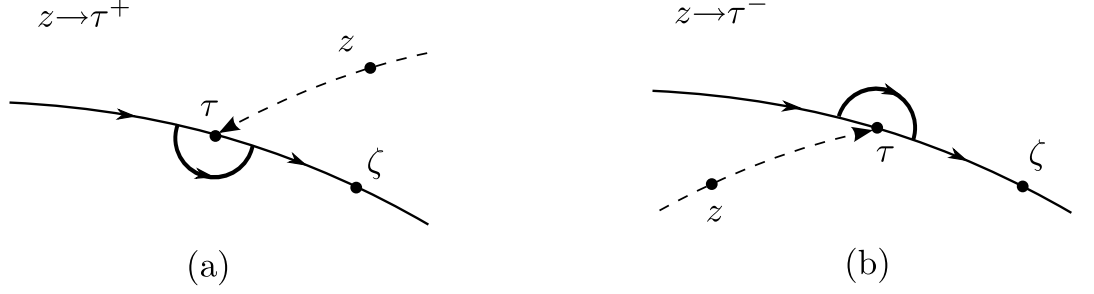


Figure 3.1 Indentation of the contour $\partial\Omega$, (a) as $z \rightarrow \tau^+$, and (b) as $z \rightarrow \tau^-$. Notice that since $\partial\Omega$ is traversed clockwise in the complex ζ -plane, the orientation on the small indentation is counter-clockwise with respect to τ when $z \rightarrow \tau^+$ and is clockwise with respect to τ when $z \rightarrow \tau^-$. On the indentation, $\zeta = \tau + re^{i\phi}$ where $r \rightarrow 0^+$.

so that the local contributions around the indentation in the last two integrals vanish when ϕ changes by an increment of π . Thus, the limit of (3.15) as $z \rightarrow \tau^+$ is

$$\begin{aligned} & \lim_{z \rightarrow \tau^+} f(z) - z\overline{f'(z)} - \overline{g(z)} \\ &= \omega(\tau, t) + \frac{1}{2\pi i} \int_{\partial\Omega} \omega(\zeta, t) d \ln \frac{\zeta - \tau}{\zeta - \bar{\tau}} + \frac{1}{2\pi i} \int_{\partial\Omega} \overline{\omega(\zeta, t)} d \frac{\zeta - \tau}{\zeta - \bar{\tau}} + \bar{\tau}(B - iQ) + 2H_1(t), \end{aligned} \quad (3.18)$$

where we have used the identities

$$d \ln \frac{\zeta - \tau}{\zeta - \bar{\tau}} = \frac{d\zeta}{\zeta - \tau} - \frac{d\bar{\zeta}}{\bar{\zeta} - \bar{\tau}}, \quad (3.19a)$$

$$d \frac{\zeta - \tau}{\zeta - \bar{\tau}} = \frac{d\zeta}{\zeta - \bar{\tau}} - \frac{(\zeta - \tau) d\bar{\zeta}}{(\bar{\zeta} - \bar{\tau})^2}. \quad (3.19b)$$

Similarly, the limit of (3.15) as $z \rightarrow \tau^-$ is

$$\begin{aligned} & \lim_{z \rightarrow \tau^-} f^i(z) - z\overline{f^{i'}(z)} - \overline{g^i(z)} \\ &= -\omega(\tau, t) + \frac{1}{2\pi i} \int_{\partial\Omega} \omega(\zeta, t) d \ln \frac{\zeta - \tau}{\zeta - \bar{\tau}} + \frac{1}{2\pi i} \int_{\partial\Omega} \overline{\omega(\zeta, t)} d \frac{\zeta - \tau}{\zeta - \bar{\tau}} \\ & \quad + \bar{\tau}(B - iQ) + 2H_1(t). \end{aligned} \quad (3.20)$$

We note that the Cauchy principal value integrals in (3.18) and (3.20) contain singularities that are integrable. This follows on observing that, as ζ passes τ on $\partial\Omega$,

$$\lim_{\zeta \rightarrow \tau} d \ln \frac{\zeta - \tau}{\bar{\zeta} - \bar{\tau}} = -i\kappa ds, \quad (3.21a)$$

$$\lim_{\zeta \rightarrow \tau} d \frac{\zeta - \tau}{\bar{\zeta} - \bar{\tau}} = -i\kappa(\zeta_s)^2 ds, \quad (3.21b)$$

where these two results are shown in Appendix B. Finally, combining (3.14), (3.18), and (3.20) yields the Sherman-Lauricella integral equation for $\omega(\tau, t)$

$$\begin{aligned} \omega(\tau, t) + \frac{\beta}{2\pi i} \int_{\partial\Omega} \omega(\zeta, t) d \ln \frac{\zeta - \tau}{\bar{\zeta} - \bar{\tau}} + \frac{\beta}{2\pi i} \int_{\partial\Omega} \overline{\omega(\zeta, t)} d \frac{\zeta - \tau}{\bar{\zeta} - \bar{\tau}} \\ + \beta \bar{\tau} (B - iQ) + H(t) = -\frac{\iota}{2} \left(\frac{\partial \tau}{\partial s} \sigma(\Gamma) \right) \end{aligned} \quad (3.22)$$

where $\beta = \frac{1-\lambda}{1+\lambda}$, $\iota = \frac{1}{1+\lambda}$, and $H(t) = 2\beta H_1(t) - H_2(t)$.

Noticing the fact that when $\beta = 1$, the Sherman-Lauricella equation (3.22) is not invertible and the term $H(t)$ can be arbitrarily prescribed as a function of t , Greengard et al. [19] suggested setting

$$\begin{aligned} H(t) = \int_{\partial\Omega} \omega(\zeta) ds(\zeta) + 2 \ln |\tau - z_c| \int_{\partial\Omega} \omega(\zeta) ds(\zeta) \\ - \frac{\tau - z_c}{\bar{\tau} - \bar{z}_c} \int_{\partial\Omega} \overline{\omega(\zeta) ds(\zeta)} + \frac{2i}{\bar{\tau} - \bar{z}_c} \operatorname{Re} \left(\int_{\partial\Omega} \omega d\bar{\zeta} \right), \end{aligned} \quad (3.23)$$

where z_c is a point in Ω^i that can be chosen arbitrarily. Later, Kropinski [26] proposed a simpler form for $H(t)$ by taking only the first term of (3.23), that is,

$$H(t) = \int_{\partial\Omega} \omega(\zeta) ds(\zeta). \quad (3.24)$$

By using either (3.23) or (3.24), the Sherman-Lauricella equation (3.22) is found to be invertible. It is also found that after we have solved (3.22) and substituted the solution for ω back into (3.23) or (3.24), $H(t)$ turns out to be zero.

Once the Sherman-Lauricella equation (3.22) for the density $\omega(\tau, t)$ has been solved, physical quantities such as the pressure and velocity can be found. It is for

this reason that this version of boundary integral method is referred to as indirect. For example, substituting the expression for $f(z)$ of (3.7) and (3.6a) into (3.2a), we find that the pressure of the exterior flow is given by

$$p = \frac{2}{\pi} Re \int_{\partial\Omega} \frac{\omega(\zeta, t)}{(\zeta - z)^2} d\zeta,$$

which can be used to find the rate of decay of the pressure that is caused by the presence of the drop as z tends to infinity.

The representations for $f(z)$ and $g(z)$ of (3.7), (3.6a), and (3.6b) with (3.1a) give an expression for the fluid velocity when $z \in \Omega$, viz.

$$\begin{aligned} u_1 + iu_2 &= -i \left(f(z) + z\overline{f'(z)} + \overline{g(z)} \right) \\ &= -\frac{1}{2\pi} \int_{\partial\Omega} \frac{\omega(\zeta, t)}{\zeta - z} d\zeta - \frac{1}{2\pi} \int_{\partial\Omega} \frac{(\zeta - z)\overline{\omega(\zeta, t)}}{(\bar{\zeta} - \bar{z})^2} d\bar{\zeta} \\ &\quad - \frac{1}{2\pi} \int_{\partial\Omega} \frac{\omega(\zeta, t) d\bar{\zeta} - \overline{\omega(\zeta, t)} d\zeta}{\bar{\zeta} - \bar{z}} + \bar{z}(Q + iB) + \frac{iG}{2}z. \end{aligned} \quad (3.25)$$

Similarly, from (3.8) the right hand side of (3.25) also gives the fluid velocity $u_1^i + u_2^i$ when $z \in \Omega^i$. Then, using (3.16a) to (3.16d) and the same type of reasoning that takes us from equation (3.15) to (3.18) and (3.20), we find that if z approaches the interface from either the exterior or interior region, the velocity at a point τ on the interface is given by

$$\begin{aligned} \mathbf{u} &= u_1 + iu_2|_{\partial\Omega} \\ &= -\frac{1}{2\pi} \int_{\partial\Omega} \omega(\zeta, t) \left(\frac{d\zeta}{\zeta - \tau} + \frac{d\bar{\zeta}}{\bar{\zeta} - \bar{\tau}} \right) \\ &\quad + \frac{1}{2\pi} \int_{\partial\Omega} \overline{\omega(\zeta, t)} d \left(\frac{\zeta - \tau}{\bar{\zeta} - \bar{\tau}} \right) + \bar{\tau}(G + iB) + \frac{iQ}{2}\tau. \end{aligned}$$

This verifies that the formulation satisfies the physical boundary condition of continuity of velocity across the interface. In the second integral, the singularity for ζ near τ on $\partial\Omega$ is integrable, which follows from (3.21b). However, the first integral is a Cauchy

principal value integral, the numerical evaluation of which will be discussed in the next chapter.

The normal velocity component u_n and the tangential velocity component u_s on the interface are such that $\mathbf{u} = u_n \mathbf{n} + u_s \mathbf{s}$. Since the complex quantities corresponding to the unit vectors \mathbf{n} and \mathbf{s} are n and s_T , respectively, with $s_T = -in$, we find that

$$u_n = \text{Re} \{ (u_1 + iu_2) \bar{n} \} , \quad (3.26)$$

$$u_s = -\text{Im} \{ (u_1 + iu_2) \bar{n} \} . \quad (3.27)$$

3.2 The Primitive Variable Formulation

The boundary integral formulation in primitive variables has been used widely since about the 1970's. In two dimensions the velocity \mathbf{u} of the interface between two immiscible fluids is the solution of the boundary integral equation [33, 34]

$$\begin{aligned} u_i(\mathbf{x}) - \frac{\beta}{2\pi} \int_{\partial\Omega} u_j(\mathbf{y}) T_{ijk}(\mathbf{y}, \mathbf{x}) n_k(\mathbf{y}) ds(\mathbf{y}) + \frac{\beta}{\chi} n_i(\mathbf{x}) \int_{\partial\Omega} u_j(\mathbf{y}) n_j(\mathbf{y}) ds(\mathbf{y}) \\ = \nu u_i^\infty(\mathbf{x}) - \frac{\nu}{4\pi} \int_{\partial\Omega} \Delta f_j(\mathbf{y}) G_{ij}(\mathbf{y}, \mathbf{x}) ds(\mathbf{y}), \end{aligned} \quad (3.28)$$

where $\nu = \frac{2}{1+\lambda}$ and $\beta = \frac{1-\lambda}{1+\lambda}$. Here, $\mathbf{x} = (x_1, x_2)$ is an arbitrary point on the interface, $\mathbf{y} = (y_1, y_2)$ is a dummy variable of integration around the interface, and the dependence on time is not indicated explicitly but is taken to be understood. In (3.28), $\Delta \mathbf{f} = (\Delta f_1, \Delta f_2) = \sigma \kappa \mathbf{n} - \nabla_s \sigma$ is the discontinuity or jump in the interfacial surface traction that appears in the stress-balance boundary condition (2.8) and χ is the total arc length of the interface. The kernel $G_{ij}(\mathbf{y}, \mathbf{x})$ is the free space Green's function for unbounded flow, while $T_{ijk}(\mathbf{y}, \mathbf{x})$ is the stress tensor corresponding to $G_{ij}(\mathbf{y}, \mathbf{x})$, that is,

$$G_{ij}(\mathbf{y}, \mathbf{x}) = -\delta_{ij} \ln |\mathbf{y} - \mathbf{x}| + \frac{(y_i - x_i)(y_j - x_j)}{|\mathbf{y} - \mathbf{x}|^2}, \quad (3.29)$$

$$T_{ijk}(\mathbf{y}, \mathbf{x}) = -\frac{4(y_i - x_i)(y_j - x_j)(y_k - x_k)}{|\mathbf{y} - \mathbf{x}|^4}, \quad (3.30)$$

where $i = 1, 2$, $j = 1, 2$, $k = 1, 2$, and δ_{ij} is the Kronecker delta. The second term on the left hand side of (3.28) accounts for the difference in viscosity between the exterior and interior fluids, while the first term on the right hand side account for the imposed flow in the far-field and the second represents the influence due to surface forces, i.e., surface tension. This latter integral is to be interpreted as a Cauchy principal value integral. It is worth noting that the third term on the left hand side is included to make the equation solvable when $\beta = 1$, that is, in the limit where the interior fluid is inviscid. Also, although the integrand is equal to the normal velocity of the interface and is therefore not usually zero point-to-point, the term and integral around the interface are zero by incompressibility.

Instead of using (3.28) directly, in the remainder of this section we try to derive its complex equivalent which we will solve numerically. The two components of (3.28) corresponding to subscript $i = 1$ and $i = 2$, respectively, are

$$\begin{aligned} u_1(\mathbf{x}) - \frac{\beta}{2\pi} \int_{\partial\Omega} u_j(\mathbf{y}) T_{1jk}(\mathbf{y}, \mathbf{x}) n_k(\mathbf{y}) ds(\mathbf{y}) + \frac{\beta}{\chi} n_1(\mathbf{x}) \int_{\partial\Omega} u_j(\mathbf{y}) n_j(\mathbf{y}) ds(\mathbf{y}) \\ = \nu u_1^\infty(\mathbf{x}) - \frac{\nu}{4\pi} \int_{\partial\Omega} \Delta f_j(\mathbf{y}) G_{1j}(\mathbf{y}, \mathbf{x}) ds(\mathbf{y}) \end{aligned} \quad (3.31a)$$

and,

$$\begin{aligned} u_2(\mathbf{x}) - \frac{\beta}{2\pi} \int_{\partial\Omega} u_j(\mathbf{y}) T_{2jk}(\mathbf{y}, \mathbf{x}) n_k(\mathbf{y}) ds(\mathbf{y}) + \frac{\beta}{\chi} n_2(\mathbf{x}) \int_{\partial\Omega} u_j(\mathbf{y}) n_j(\mathbf{y}) ds(\mathbf{y}) \\ = \nu u_2^\infty(\mathbf{x}) - \frac{\nu}{4\pi} \int_{\partial\Omega} \Delta f_j(\mathbf{y}) G_{2j}(\mathbf{y}, \mathbf{x}) ds(\mathbf{y}), \end{aligned} \quad (3.31b)$$

Multiplying (3.31a) by the imaginary unit i then subtracting (3.31b) and letting $w = iu_1 - u_2$ gives an equivalent complex form of (3.28). In deriving this complex formulation, we let $x = x_1 + ix_2$ be an arbitrary point on the interface and $y = y_1 + iy_2$ denote the variable of integration around the interface. Since the interface is traversed clockwise, with our choice of orientation of \mathbf{n}

$$\mathbf{n}(\mathbf{x}) = (n_1, n_2) = \left(-\frac{dx_2}{ds}, \frac{dx_1}{ds} \right). \quad (3.32)$$

In the resulting complex form, the first term on the left hand side is

$$TL_1 = iu_1 - u_2 = w(x, t). \quad (3.33)$$

The second term on the left hand side turns out to be

$$\begin{aligned} TL_2 &= -\frac{\beta}{2\pi} \left[i \int_{\partial\Omega} u_j(\mathbf{y}) T_{1jk}(\mathbf{y}, \mathbf{x}) n_k(\mathbf{y}) ds(\mathbf{y}) - \int_{\partial\Omega} u_j(\mathbf{y}) T_{2jk}(\mathbf{y}, \mathbf{x}) n_k(\mathbf{y}) ds(\mathbf{y}) \right] \\ &= \frac{i\beta}{2\pi} \left(\int_{\partial\Omega} w(y, t) d \ln \frac{y-x}{\bar{y}-\bar{x}} - \int_{\partial\Omega} \overline{w(y, t)} d \frac{y-x}{\bar{y}-\bar{x}} \right) \end{aligned} \quad (3.34)$$

after some manipulation, where we have used (3.30). The third term on the left hand side is

$$\begin{aligned} TL_3 &= \frac{i\beta n}{\chi} \int_{\partial\Omega} u_j(\mathbf{y}) n_j(\mathbf{y}) ds(\mathbf{y}) \\ &= \frac{i\beta n}{\chi} \int_{\partial\Omega} -u_1 dy_2 + u_2 dy_1 \\ &= \frac{\beta x_s}{\chi} \operatorname{Re} \int_{\partial\Omega} w(y, t) d\bar{y}, \end{aligned} \quad (3.35)$$

where, from (3.32), $n = n_1 + in_2 = ix_s$. When the far-field behavior for the exterior flow (2.17) is assumed, the first term on the right hand side becomes

$$TR_1 = \nu(iu_1^\infty - u_2^\infty) = \nu \left(iQ\bar{x} - B\bar{x} - \frac{G}{2}x \right). \quad (3.36)$$

To derive the second term on the right hand side, we let $\hat{y}_1 = y_1 - x_1$, $\hat{y}_2 = y_2 - x_2$, $\hat{y} = y - x$, and $r = |y - x|$ for convenience. Then

$$\begin{aligned} TR_2 &= -\frac{\nu}{4\pi} \int_{\partial\Omega} i\Delta f_j(\mathbf{y}) G_{1j}(\mathbf{y}, \mathbf{x}) - \Delta f_j(\mathbf{y}) G_{2j}(\mathbf{y}, \mathbf{x}) ds(\mathbf{y}) \\ &= \frac{\nu}{4\pi} \int_{\partial\Omega} (\Delta f_1 G_{21} + \Delta f_2 G_{22}) - i(\Delta f_1 G_{11} + \Delta f_2 G_{12}) ds(\mathbf{y}) \\ &= \frac{\nu}{4\pi} \int_{\partial\Omega} -\Delta f_2 \ln r + \Delta f_1 \frac{\hat{y}_1 \hat{y}_2}{r^2} + \Delta f_2 \frac{\hat{y}_2^2}{r^2} + i \left(\Delta f_1 \ln r - \Delta f_2 \frac{\hat{y}_1 \hat{y}_2}{r^2} - \Delta f_1 \frac{\hat{y}_1^2}{r^2} \right) ds(y) \\ &= \frac{i\nu}{4\pi} \left[\int_{\partial\Omega} (\Delta f_1 + i\Delta f_2) \ln r ds(y) - \frac{1}{2} \int_{\partial\Omega} (\Delta f_1 + i\Delta f_2) ds(y) \right. \\ &\quad \left. - \frac{1}{2} \int_{\partial\Omega} (\Delta f_1 - i\Delta f_2) \frac{y-x}{\bar{y}-\bar{x}} ds(y) \right] \end{aligned}$$

Similar to (3.13), it is found that $\Delta f_1 + i\Delta f_2 = -(y_s\sigma(\Gamma))_s$, from which TR_2 can be simplified to become

$$TR_2 = \frac{i\nu}{8\pi} \left[- \int_{\partial\Omega} \ln(r^2)(y_s\sigma)_s ds(y) + \int_{\partial\Omega} (y_s\sigma)_s ds(y) + \int_{\partial\Omega} (\bar{y}_s\sigma)_s \frac{y-x}{\bar{y}-\bar{x}} ds(y) \right] \quad (3.37a)$$

$$= \frac{i\nu}{8\pi} \left[\int_{\partial\Omega} y_s\sigma(\Gamma) \left(\frac{dy}{y-x} + \frac{d\bar{y}}{\bar{y}-\bar{x}} \right) + \int_{\partial\Omega} (\bar{y}_s\sigma(\Gamma))_s \frac{y-x}{\bar{y}-\bar{x}} ds(y) \right], \quad (3.37b)$$

where in the (3.37a) the first integral has been integrated by parts and the second integral vanishes by periodicity.

Combining all terms from (3.33) to (3.36) and (3.37b) together in complex form, we have

$$\begin{aligned} w(x, t) + \frac{i\beta}{2\pi} \left(\int_{\partial\Omega} w(y, t) d \ln \frac{y-x}{\bar{y}-\bar{x}} - \int_{\partial\Omega} \overline{w(y, t)} d \frac{y-x}{\bar{y}-\bar{x}} \right) + \frac{\beta x_s}{\chi} Re \int_{\partial\Omega} w(y, t) d\bar{y} \\ = \nu \left(iQ\bar{x} - B\bar{x} - \frac{G}{2}x \right) + \frac{i\nu}{8\pi} \left[\int_{\partial\Omega} y_s\sigma(\Gamma) \left(\frac{dy}{y-x} + \frac{d\bar{y}}{\bar{y}-\bar{x}} \right) \right. \\ \left. + \int_{\partial\Omega} (\bar{y}_s\sigma(\Gamma))_s \frac{y-x}{\bar{y}-\bar{x}} ds(y) \right]. \quad (3.38) \end{aligned}$$

The first integral on the right hand side is to be interpreted as a Cauchy principal value integral, while in all other integrals the integrand is regular.

Once the solution for w is found, we can quickly recover the interfacial velocity \mathbf{u} from (3.33). Also, the normal and tangential velocity can be calculated by the same identities (3.26) and (3.27) as used in the Sherman-Lauricella formulation.

CHAPTER 4

NUMERICAL METHOD

Numerical solution of the problem rests on two important aspects:

- The time-dependent evolution of the interface profile, the surfactant concentration on the interface, and the surfactant concentration in the bulk flow.
- The spatial discretization of the computational domains, including the interface and the transition layer.

4.1 Tracking the Motion of the Interface

4.1.1 The Equal Arc Length Frame

Tracking the motion of the interface by solving the kinematic condition

$$\frac{d\mathbf{x}}{dt} = \mathbf{u}(\mathbf{x}, t) = u_n \mathbf{n} + u_s \mathbf{s} \quad \mathbf{x} \in \partial\Omega \quad (4.1)$$

usually leads to either clustering or sparseness of the marker points, especially when large-time simulations accompanied by significant deformation of the interface are carried out. On the one hand, it can be seen from (4.7a) below that when we time-step (4.1) by using simple explicit schemes, such as the forward Euler method, the constraint on the time step Δt is that Δt should be of the same order as Δs , the step size of the discretization in space at the interface. This implies that solving (4.1) will be numerically stiff when the marker points congregate. On the other hand, sparseness of marker points leads to inadequate resolution of the interface profile.

To resolve this difficulty, we note that the shape of a moving interface is determined solely by its normal velocity $u_n = \mathbf{u} \cdot \mathbf{n}$, which is also the normal component of the fluid velocity, and is independent of the tangential fluid velocity $u_s = \mathbf{u} \cdot$

s. Hence, to update the location of the marker points we can choose an artificial tangential velocity u_s^E in the numerical condition that keeps the marker points equally spaced in arc length. This is the approach introduced by Hou et al. [23], and we see the benefit of using it in the following sections.

We first introduce a parametrization of $\partial\Omega$ so that the interface is described by $\tau = x_1(\alpha, t) + ix_2(\alpha, t)$, where $\alpha \in [0, 2\pi)$ is a renormalized arc length, so that at any instant in time a uniformly spaced mesh in $\alpha \in [0, 2\pi)$ corresponds to a uniformly spaced, i.e., equal arc length, mesh along the interface $\partial\Omega$. As above, we denote the arc length of the interface by s and the tangent angle by θ . It follows that the complex unit tangent and normal are

$$s_T = \frac{\tau_\alpha}{s_\alpha} = e^{i\theta}, \quad (4.2)$$

$$n = is_T = ie^{i\theta}, \quad (4.3)$$

where $s_\alpha = |\tau_\alpha|$. From (4.2), τ_α can be expressed as

$$\tau_\alpha = s_\alpha e^{i\theta}, \quad (4.4)$$

and differentiating with respect to time t , we have

$$\tau_{\alpha t} = s_{\alpha t} e^{i\theta} + s_\alpha \theta_t i e^{i\theta}. \quad (4.5)$$

To construct the equal arc length frame we recall that the kinematic condition at the interface in complex form is

$$\frac{d\tau}{dt} = u_n i e^{i\theta} + u_s e^{i\theta},$$

But now, although u_s is the normal velocity of both the interface and fluid, u_s is to be determined. This allows us to express $\tau_{\alpha t}$ in another form by differentiating with

respect to α , i.e.,

$$\tau_{\alpha t} = ((u_s)_\alpha - u_n \theta_\alpha) e^{i\theta} + ((u_n)_\alpha + u_s \theta_\alpha) i e^{i\theta}. \quad (4.6)$$

Equating (4.5) and (4.6) gives

$$s_{\alpha t} = (u_s)_\alpha - u_n \theta_\alpha, \quad (4.7a)$$

$$\theta_t = \frac{1}{s_\alpha} ((u_n)_\alpha + u_s \theta_\alpha), \quad (4.7b)$$

where $\partial\Omega$ is now described parametrically by $s = s(\alpha, t)$ and $\theta = \theta(\alpha, t)$ instead of $x_1 = x_1(\alpha, t)$ and $x_2 = x_2(\alpha, t)$.

It is clear that at any instant in time the arc length between any two consecutive marker points is the same provided that s_α is constant along the interface. To this end, we require s_α to be everywhere equal to its mean, that is,

$$s_\alpha(\alpha, t) = \frac{1}{2\pi} \int_0^{2\pi} s_\alpha(\alpha', t) d\alpha', \quad (4.8)$$

where α' is the variable of integration. It follows straight away that since s_α is independent of α , $\alpha \in [0, 2\pi)$ is a renormalized arc length. Differentiating (4.8) with respect to t gives

$$s_{\alpha t}(\alpha, t) = \frac{1}{2\pi} \int_0^{2\pi} s_{\alpha t}(\alpha', t) d\alpha',$$

and substituting the expression for $s_{\alpha t}$ of (4.7a) gives

$$(u_s)_\alpha - u_n \theta_\alpha = \frac{1}{2\pi} \int_0^{2\pi} (u_s)_{\alpha'} - u_n \theta_{\alpha'} d\alpha'. \quad (4.9)$$

Since $\int_0^{2\pi} (u_s)_{\alpha'} d\alpha' = 0$, (4.9) can be rewritten as

$$(u_s)_\alpha = u_n \theta_\alpha - \frac{1}{2\pi} \int_0^{2\pi} u_n \theta_{\alpha'} d\alpha', \quad (4.10)$$

and on integrating both sides of (4.10) with respect to α , we find that

$$u_s(\alpha, t) = -\frac{\alpha}{2\pi} \int_0^{2\pi} u_n \theta_{\alpha'} d\alpha' + \int_0^\alpha u_n \theta_{\alpha'} d\alpha' + u_{s0}(0, t), \quad (4.11)$$

where $u_{s0}(0, t)$ is an arbitrary function of time, which is the tangential velocity of the point corresponding to $\alpha = 0$ and is usually set to zero. Equation (4.11) gives the required tangential velocity u_s of the equal arc length frame.

The equal arc length mesh can be maintained provided it is set up at some initial time and the tangential velocity $u_s(\alpha, t)$ of equation (4.11) is enforced at each update of the marker points, that is at each time step, throughout the simulation. We now denote this constructed tangential velocity by u_s^E and save the notation u_s for the tangential velocity of the fluid at the interface obtained by (3.27). Thus,

$$u_s^E(\alpha, t) = -\frac{\alpha}{2\pi} \int_0^{2\pi} u_n \theta_{\alpha'} d\alpha' + \int_0^\alpha u_n \theta_{\alpha'} d\alpha' + u_s^E(0, t). \quad (4.12)$$

We note that u_s and u_s^E are different. The fluid tangential velocity on $\partial\Omega$, u_s , has physical significance, while u_s^E is an artificial quantity that is introduced solely to maintain an equal arc length frame. Also, we point out that when we use the artificial velocity u_s^E in (4.12) to maintain an equal arc length frame and parameterize $\partial\Omega$ by α so that $\mathbf{x} = \mathbf{X}(\alpha, t)$, the term $\frac{\partial \mathbf{X}}{\partial t} \Big|_\xi$ in (2.11) and $U_s = \mathbf{U}_s \cdot \mathbf{s}$ are u_s^E .

Finally, substituting (4.12) into (4.7a) and (4.7b) gives the system by which we track the dynamics of the interface,

$$s_{\alpha t} = -\frac{1}{2\pi} \int_0^{2\pi} u_n \theta_{\alpha'} d\alpha', \quad (4.13a)$$

$$\theta_t = \frac{1}{s_\alpha} \left[\theta_\alpha \left(\int_0^\alpha u_n \theta_{\alpha'} d\alpha' - \frac{\alpha}{2\pi} \int_0^{2\pi} u_n \theta_{\alpha'} d\alpha' \right) + (u_n)_\alpha \right]. \quad (4.13b)$$

At each time step, when (4.13a) and (4.13b) are integrated forward in time, we map (s_α, θ) to (x_1, x_2) in order to update the position of the interface marker points and proceed with the computation at the next time step. This map is given by integrating

(4.4) with respect to α , that is,

$$x_1(\alpha, t) = x_1(0, t) + s_\alpha(t) \int_0^\alpha \cos(\theta(\alpha', t)) d\alpha' \quad (4.14a)$$

$$x_2(\alpha, t) = x_2(0, t) + s_\alpha(t) \int_0^\alpha \sin(\theta(\alpha', t)) d\alpha', \quad (4.14b)$$

where $(x_1(0, t), x_2(0, t))$ is the position of the marker point corresponding to $\alpha = 0$ at time t .

All the required information contained in the kinematic condition (2.16) or (4.1) is contained in (4.13a) and (4.13b) via the normal velocity u_n of the interface.

4.1.2 Dealiasing

Since the increase in the total arc length of $\partial\Omega$ in time and the development of regions of high curvature on the interface necessitate an increase in the number of marker points M on $\partial\Omega$, so as to avoid aliasing error and a loss of accuracy, the time step Δt must also be reduced to avoid a numerical instability and to maintain high-order accuracy. To detect and measure the aliasing error and instability, we study the Fourier modes of the variable θ . Suppose that we have the discrete value of θ at M marker points along the interface $\partial\Omega$, then we compute the corresponding Fourier modes by taking a FFT and list them in the order

$$\hat{\theta}_0, \hat{\theta}_1, \hat{\theta}_2, \dots, \hat{\theta}_{M/2}, \hat{\theta}_{-M/2+1}, \hat{\theta}_{-M/2+2}, \dots, \hat{\theta}_{-2}, \hat{\theta}_{-1}.$$

Here, the subscripts in the sequence correspond to the wave numbers of the Fourier modes. Denoting the step size in α by h , the wavenumber $M/2 = \pi/h$ is usually termed the Nyquist frequency, and aliasing is avoided if the Nyquist frequency is greater than the bandwidth, or maximum component frequency, of the function being sampled.

For a mesh with fixed M that becomes more deformed, the Fourier modes of the independent variable θ grow rapidly near the Nyquist frequency. This is a typical

symptom of aliasing that can be observed in Fourier space. There are two means to deal with this. Kropinski [26] used the padding method, which eliminates the aliasing error exactly. When the locations of the M marker points are known, one can first compute the location of twice the number of marker points in physical space by A FFT and then calculate the velocity at these $2M$ marker points. Then, by truncating the Fourier modes of the velocity to the original size, M , the aliasing error can be removed. This method is rigorous but we consider it to be too expensive to implement.

The method we choose instead is to filter the aliasing via a 25th-order filter

$$\hat{\prod}[\theta](k) = e^{-10\left(\frac{|k|}{M/2}\right)^{25}} \hat{\theta}(k), \quad k = -\frac{M}{2} + 1, -\frac{M}{2} + 2, \dots, \frac{M}{2}, \quad (4.15)$$

see [23, 27]. After computing the profile at each time step, the aliasing error is filtered by exponentially damping the modes near the Nyquist frequency via this filter. The filtering method is much cheaper in terms of CPU time compared to padding. It is also worth mentioning that a Krasny filter [25] is applied to prevent the round-off error near the Nyquist frequency from growing and contaminating the computation as time increases. This is carried out by setting to zero all Fourier modes with magnitude below a tolerance threshold (Threshold 1), whose typical value is 10^{-12} .

The profile of the interface often turns out to be highly deformed after some time in most of our simulations, which leads to inadequate resolution of its profile. To overcome this, the Fourier spectrum is checked after each time step, and if the modes near the Nyquist frequency rise above a second threshold (Threshold 2), the number of nodes M is doubled by inserting M zeros at and above the Nyquist frequency and then transforming back to physical space. Kropinski [26, 27] used roundoff as Threshold 2, while we set this value as 10^{-13} .

4.2 Spatial Discretization

When the equal arc length frame is adopted, i.e., the distance in the arc length s between any two neighboring marker points is uniform, one can solve the boundary integral equation (3.22) or (3.38) with spectral accuracy by the Nyström method using the trapezoidal rule. In this section we describe the discretization of the boundary integral equation (3.38), the governing equation (2.21) for the dissolved bulk surfactant concentration C , and the equation (2.24) for the absorbed surfactant concentration Γ at the interface.

4.2.1 The Boundary Integral Equation

Here, we describe the discretization of the boundary integral equation (3.38) in detail. The Sherman-Lauricella equation (3.22) is discretized similarly.

If we use M marker points to resolve the interface, all of which are uniformly distributed in arc length, the step size in α is $h = \frac{2\pi}{M}$. When the evaluation point x and the integration point y are not coincident, the following identities can easily be derived

$$\begin{aligned} d \ln \frac{y-x}{\bar{y}-\bar{x}} &= \left(\frac{y_\alpha}{y-x} - \frac{\bar{y}_\alpha}{\bar{y}-\bar{x}} \right) d\alpha, \\ d \frac{y-x}{\bar{y}-\bar{x}} &= \left(\frac{y_\alpha}{\bar{y}-\bar{x}} - \frac{\bar{y}_\alpha(y-x)}{(\bar{y}-\bar{x})^2} \right) d\alpha. \end{aligned} \quad (4.16)$$

As noted at the end of Chapter 3, the singularities in the integrals on the left hand side of (3.38) and the last integral on the right hand side of (3.38) are removable. This is seen on noting that as the variable of integration y approaches the evaluation point x ,

$$\lim_{y \rightarrow x} d \ln \frac{y-x}{\bar{y}-\bar{x}} = -i\kappa ds = -i\kappa s_\alpha d\alpha, \quad (4.17a)$$

$$\lim_{y \rightarrow x} d \frac{y-x}{\bar{y}-\bar{x}} = -i\kappa y_s^2 ds = -i\kappa \frac{y_\alpha^2}{s_\alpha} d\alpha, \quad (4.17b)$$

$$\lim_{y \rightarrow x} \frac{y-x}{\bar{y}-\bar{x}} ds(y) = \frac{y_\alpha}{\bar{y}_\alpha} ds = \frac{y_\alpha^2}{s_\alpha} d\alpha. \quad (4.17c)$$

The first two of these results was noted earlier at (3.19a) and (3.19b), where we denoted the evaluation point by $x = \tau$ and the variable of integration by $y = \zeta$ there. Like these two results, the third result is shown in Appendix B.

As was also noted at the end of Chapter 3, the first integral on the right hand side of (3.38) is to be interpreted as a Cauchy principal value integral. Using Pullin's desingularization method, as discussed in [3] and [35], it can be evaluated by the trapezoidal rule with spectral accuracy. To set up the discretization we let $x = x(\alpha)$ be an arbitrary point on $\partial\Omega$ and denote the mesh points on $\partial\Omega$ in the complex plane by x_j , for $j = 1, \dots, M$. As previously, the time dependence of w etc. is not shown explicitly. Then the evaluation point is $x = x_j$ for some j while the variable of integration in (3.38) is $y = x_k$ with summation over the index k , and for example $w_j = w(x_j)$. The quadrature of the Cauchy principal value integral is then given by

$$\begin{aligned} & \int_{\partial\Omega} y_s \sigma \left(\frac{dy}{y-x} + \frac{d\bar{y}}{\bar{y}-\bar{x}} \right) \\ &= h \sum_{\substack{k=1 \\ k \neq j}}^M \left[\frac{(x_\alpha)_k}{x_k - x_j} + \frac{(\bar{x}_\alpha)_k}{\bar{x}_k - \bar{x}_j} \right] \frac{(x_\alpha \sigma)_k}{(s_\alpha)_k} + h \operatorname{Re} \left(\frac{x_{\alpha\alpha}}{x_\alpha} \right)_j \frac{(x_\alpha \sigma)_j}{(s_\alpha)_j} + 2h \frac{((x_\alpha \sigma)_\alpha)_j}{(s_\alpha)_j} \end{aligned} \quad (4.18)$$

where the index $j = 1, \dots, M$ indicates at which marker point the integral is evaluated and k is a dummy index. We defer the proofs of (4.17a)-(4.17c) and (4.18) in Appendix B.

Combining (4.16), (4.17a)-(4.17c), and (4.18) with (3.38), we obtain the discrete system

$$\begin{aligned}
w_j + \frac{i\beta h}{2\pi} & \left[2i \sum_{\substack{k=1 \\ k \neq j}}^M w_k \operatorname{Im} \left(\frac{(x_\alpha)_k}{x_k - x_j} \right) - i\kappa_j s_\alpha w_j - \sum_{\substack{k=1 \\ k \neq j}}^M \left(\frac{\bar{w}_k (x_\alpha)_k}{\bar{x}_k - \bar{x}_j} - \frac{\bar{w}_k (x_k - x_j) (\bar{x}_\alpha)_k}{(\bar{x}_k - \bar{x}_j)^2} \right) \right. \\
& \left. + i\kappa_j \bar{w}_j \frac{(x_\alpha)_j^2}{s_\alpha} \right] + \frac{\beta h (x_\alpha)_j}{\chi s_\alpha} \operatorname{Re} \left(\sum_{k=1}^M w_k (\bar{x}_\alpha)_k \right) = \nu \left(iQ\bar{x}_j - B\bar{x}_j - \frac{G}{2} x_j \right) \\
& + \frac{i\nu h}{8\pi s_\alpha} \left[2 \sum_{\substack{k=1 \\ k \neq j}}^M \operatorname{Re} \left(\frac{(x_\alpha)_k}{x_k - x_j} \right) (x_\alpha \sigma)_k + \operatorname{Re} \left(\frac{x_{\alpha\alpha}}{x_\alpha} \right)_j (x_\alpha \sigma)_j + 2((x_\alpha \sigma)_\alpha)_j \right. \\
& \left. + \sum_{\substack{k=1 \\ k \neq j}}^M ((\bar{x}_\alpha \sigma)_\alpha)_k \frac{x_k - x_j}{\bar{x}_k - \bar{x}_j} + ((\bar{x}_\alpha \sigma)_\alpha)_j \frac{(x_\alpha)_j^2}{s_\alpha^2} \right] \quad j = 1, \dots, M, \quad (4.19)
\end{aligned}$$

by solving which and using (3.33) the velocity of the interface at the marker points can be found.

To solve (4.19), we separate the real and complex parts to form a $2M \times 2M$ linear algebraic system $Ax = b$ which is solved by the generalized minimal residual method (GMRES). The benefit of forming the primitive boundary integral equation in complex form (3.38) as opposed to real form (3.28) is now clear. First, it is easier in complex form to find the limits as the integration point y approaches the evaluation point x and to evaluate the Cauchy principal value integral (4.18). Second, with the boundary integral equation in the form (3.38) it is easier to apply the 2D fast multipole method (FMM) which is usually coded in complex number arithmetic. In each iteration of GMRES, the FMM can significantly speed up the evaluation of Ax by reducing the operation number from $O(M^2)$ to $O(M)$. However, we have not implemented the FMM in this dissertation and save it for future work.

4.2.2 The Convection-Diffusion Equation for the Bulk Surfactant Concentration in the Transition Layer

The transition layer, where the convection-diffusion equation (2.21) holds, is defined on a rectangular domain, see Figure 4.1. If we use $\alpha \in [0, 2\pi)$ introduced in Section 4.1.1 to parametrize the interface $\partial\Omega$, the bulk surfactant concentration $C(\alpha, N, t)$ is 2π -periodic in the α -direction, that is, $C(0, N, t) = C(2\pi, N, t)$. For all time t , $C(\alpha, N, t)$ matches the far-field boundary condition $C(\alpha, \infty, t) = 1$ at the upper boundary of the domain, while at the lower boundary $C(\alpha, N, t)$ satisfies the boundary condition $C(\alpha, 0, t) = \Gamma(\alpha, t)/K(1-\Gamma(\alpha, t))$, where $\Gamma(\alpha, t)$ is the surfactant concentration at the interface. With the uniform initial condition given in (2.22) we patch up the problem for the concentration of the surfactant adsorbed in the transition layer

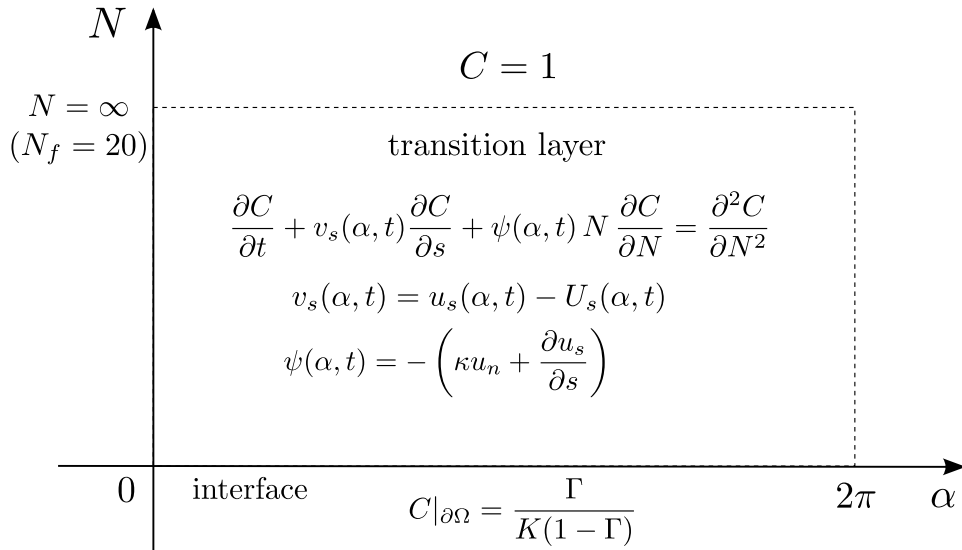


Figure 4.1 The computational domain of the transition layer equation (2.21). A periodic boundary condition is applied in the α -direction and we impose the far-field boundary condition $C = 1$ at an artificial boundary N_f , which is set to $N_f = 20$ in our numerical simulations.

as

$$\frac{\partial C}{\partial t} + v_s(\alpha, t) \frac{\partial C}{\partial s} + \psi(\alpha, t) N \frac{\partial C}{\partial N} = \frac{\partial^2 C}{\partial N^2}, \quad (4.20a)$$

where $v_s(\alpha, t) = u_s(\alpha, t) - U_s(\alpha, t)$

$$\text{and } \psi(\alpha, t) = - \left(\kappa u_n + \frac{\partial u_s}{\partial s} \right),$$

$$\text{initial condition: } C(\alpha, N, t = 0) = 1, \quad (4.20b)$$

$$\begin{aligned} \text{boundary conditions: } C(\alpha, N = 0, t) &= \frac{\Gamma(\alpha, t)}{K(1 - \Gamma(\alpha, t))} \\ \text{and } C(\alpha, N = \infty, t) &= 1. \end{aligned} \quad (4.20c)$$

Here, v_s , u_s , and U_s are respectively the projection of \mathbf{v}_s , \mathbf{u}_s , and \mathbf{U}_s on the tangential direction, i.e., $v_s = \mathbf{s} \cdot \mathbf{v}_s$, $u_s = \mathbf{s} \cdot \mathbf{u}_s$, and $U_s = \mathbf{s} \cdot \mathbf{U}_s$.

Now we consider the discretization of the problem defined by (4.20a)-(4.20c). Since the interface is represented by M points that are equally spaced in α to maintain the equal arc length frame, we discretize the computational domain in Figure 4.1 by M uniformly distributed points in α -direction.

Although the far-field boundary condition $C = 1$ is imposed as $N \rightarrow \infty$ we truncate the computational domain by applying the same boundary condition at finite $N = N_f$. A typical position of this artificial boundary is given by taking $N_f = 20$. When an artificially truncated domain is adopted, the domain is discretized by $m + 1$ Chebyshev-Lobatto points in the N -direction, that is,

$$N_j = \frac{N_f}{2} (\cos(j\pi/m) + 1), \quad j = 0, 1, \dots, m. \quad (4.21)$$

The collocation points are not uniformly distributed in the N -direction but cluster near $N = 0$ and $N = N_f$. Time-stepping (4.20a) by using fully explicit schemes is numerically stiff due to the presence of the diffusion term. Therefore, $\frac{\partial^2 C}{\partial N^2}$ is treated implicitly while the second and third terms on the left hand side of (4.20a) are calculated explicitly. In the second term on the left hand side, $\frac{\partial C}{\partial s}$ can be rewritten as

$\frac{C_\alpha}{s_\alpha}$, where C_α is the derivative of C with respect to α and s_α is uniform in α when the equal arc length frame is used. FFT is used to compute C_α with spectral accuracy.

Once the second term on the left hand side is computed explicitly, the problem (4.20a)-(4.20c) can be thought of as a one dimensional convection-diffusion equation with respect to the normal coordinate N alone for each α , that is,

$$\frac{\partial C}{\partial t} + \rho(t) + \psi(t) N \frac{\partial C}{\partial N} = \frac{\partial^2 C}{\partial N^2}, \quad (4.22a)$$

$$\text{where } \rho(t) = v_s(t) \frac{\partial C}{\partial s} \text{ and } \psi(t) = -\kappa u_n - \frac{\partial u_s}{\partial s},$$

$$\text{initial condition: } C(N, t = 0) = 1, \quad (4.22b)$$

$$\text{boundary condition: } C(N = 0, t) = \frac{\Gamma(t)}{K(1 - \Gamma(t))}$$

$$\text{and } C(N = \infty, t) = 1, \quad (4.22c)$$

where the dependence of the problem on α has been omitted. Now we turn to the computation of the third term on the left hand side of (4.22a). The normal derivative of the bulk concentration $\frac{\partial C}{\partial N}$ at the Chebyshev points (4.21) is computed via FFT again. Standard references on Chebyshev differentiation via FFT are [9] and [46].

Since the diffusion term on the right hand side of (4.22a) needs to be treated implicitly, we can not use FFT to compute the second derivative of C with respect to N . Instead, we use the differentiation matrix D_{m+1} corresponding to the $m + 1$ Chebyshev-Lobatto points given by (4.21), that is,

$$D_{m+1} = \frac{1}{N_f} D_{m+1}^e, \quad (4.23)$$

where D_{m+1}^e is the Chebyshev differentiation matrix which corresponds to the Chebyshev-Lobatto points N_j^e defined on $[-1, 1]$, that is,

$$N_j^e = \cos(j\pi/m) \quad \text{for } j = 0, 1, \dots, m.$$

The entries of the $(m + 1) \times (m + 1)$ matrix D_{m+1}^e are respectively

$$\begin{aligned} (D_{m+1}^e)_{00} &= \frac{2m^2 + 1}{6}, & (D_{m+1}^e)_{mm} &= -\frac{2m^2 + 1}{6}, \\ (D_{m+1}^e)_{jj} &= -\frac{N_j^e}{2(1 - (N_j^e)^2)}, & j &= 1, \dots, m - 1, \\ (D_{m+1}^e)_{ij} &= \frac{(-1)^{i+j} c_i}{c_j (N_i^e - N_j^e)}, & i \neq j, \quad i, j &= 0, \dots, m, \end{aligned}$$

where $c_j = \begin{cases} 2, & j = 0 \text{ or } m, \\ 1, & \text{otherwise.} \end{cases}$

The time marching of the problem will be discussed in Section 4.3.

4.2.3 The Convection-Diffusion Equation for the Adsorbed Surfactant Concentration on the Interface

We rewrite equation (2.24) to take advantage of the two-dimensional geometry as

$$\left. \frac{\partial \Gamma}{\partial t} \right|_{\alpha} - u_s^E \Gamma_s + (\Gamma u_s)_s + \Gamma \kappa u_n = \frac{1}{Pe_s} \Gamma_{ss} + J_0 \left. \frac{\partial C}{\partial N} \right|_{\partial \Omega}, \quad (4.24)$$

where u_s is the tangential velocity of the fluid at the interface and u_s^E is the tangential velocity of the marker points that is used to maintain the equal arc length frame. That is, in (2.24) the parameterization $\mathbf{x} = \mathbf{X}(\xi, t)$ of the interface is with the parameter $\xi = \alpha$. With this parameterization the equation is recast as

$$\left. \frac{\partial \Gamma}{\partial t} \right|_{\alpha} - u_s^E \frac{\Gamma_{\alpha}}{s_{\alpha}} + \frac{(\Gamma u_s)_{\alpha}}{s_{\alpha}} + \Gamma \kappa u_n = \frac{1}{Pe_s} \frac{\Gamma_{\alpha\alpha}}{s_{\alpha}^2} + J_0 \left. \frac{\partial C}{\partial N} \right|_{\partial \Omega}. \quad (4.25)$$

In (4.25), we treat the diffusion term explicitly since the inverse surface Peclet number Pe_s^{-1} and diffusion term are sufficiently small that the problem is not stiff. In fact, as mentioned at the end of Section 2.3, the effect of surface diffusion is sufficiently small that it is neglected in the simulations. Therefore, all the derivative with respect to α is computed via FFT. The normal derivative of the bulk surfactant concentration at the interface is evaluated explicitly by using the Chebyshev differentiation via FFT.

4.3 Time Marching

Since the time-dependent quantities are the interface position x which is uniquely determined by s_α and θ , the surfactant concentration on the interface Γ , and the bulk surfactant concentration C , we rewrite the problem in the form of (4.19) for u together with the system

$$\begin{aligned} \partial_t \begin{pmatrix} s_\alpha \\ \theta \\ \Gamma \end{pmatrix} &= \mathbf{R} \left(s_\alpha, \theta, \Gamma, \left. \frac{\partial C}{\partial N} \right|_{\partial\Omega} \right) \\ \partial_t C &= S(s_\alpha, \theta, \Gamma, C, N) + \frac{\partial^2 C}{\partial N^2}, \end{aligned}$$

where the definition of \mathbf{R} and S is given by referring to (4.13a) and (4.13b), (4.22a), and (4.25). Here we omit the dependence of \mathbf{R} and S on the tangential velocity u_s and the normal velocity u_n , since the velocity u can be obtained from the knowledge of s_α , θ , and Γ via the boundary integral equation. In this way, the boundary integral equation can be regarded as a linear map from the interface location and the surface surfactant concentration to the velocity of the interface at the same instant.

To obtain second order accuracy in time, we implement a two-step variation of the Crank-Nicolson method by first computing the intermediate values $(\tilde{s}_\alpha)_i^{n+1}$, $\tilde{\theta}_i^{n+1}$, $\tilde{\Gamma}_i^{n+1}$, and $\tilde{C}_{i,j}^{n+1}$ using a forward Euler scheme.

$$\begin{aligned} \begin{pmatrix} (\tilde{s}_\alpha)_i^{n+1} \\ \tilde{\theta}_i^{n+1} \\ \tilde{\Gamma}_i^{n+1} \end{pmatrix} &= \begin{pmatrix} (s_\alpha)_i^n \\ \theta_i^n \\ \Gamma_i^n \end{pmatrix} + \Delta t \mathbf{R}_i^n \\ \tilde{C}_{i,j}^{n+1} &= C_{i,j}^n + \Delta t \left(S_{i,j}^n + (D_{m+1}^2 \tilde{C}_i^{n+1})_j \right), \end{aligned} \tag{4.26}$$

where the superscript and the first and second subscripts are the indices for the time step, the marker point in the α -direction, and the marker point in the N -direction, respectively. Here, the operator D_{m+1} is the $(m+1) \times (m+1)$ Chebyshev differentiation

matrix defined in (4.23). Note that $C_{i,0}^n = \frac{\Gamma_i^n}{K(1-\Gamma_i^n)}$ and $C_{i,m}^n = 1$ from the boundary conditions (4.22c). Also we recall that calculation of $S_{i,j}^n$ which includes the second and third term on the left hand side of (4.20a) is fulfilled by using the discretization and technique discussed in Section 4.2.2.

The second step provides a second order correction for the first step.

$$\begin{pmatrix} (s_\alpha)_i^{n+1} \\ \theta_i^{n+1} \\ \Gamma_i^{n+1} \end{pmatrix} = \begin{pmatrix} (s_\alpha)_i^n \\ \theta_i^n \\ \Gamma_i^n \end{pmatrix} + \frac{\Delta t}{2} (\mathbf{R}_i^n + \tilde{\mathbf{R}}_i^{n+1}) \quad (4.27)$$

$$C_{i,j}^{n+1} = C_{i,j}^n + \frac{\Delta t}{2} \left(S_{i,j}^n + \tilde{S}_{i,j}^{n+1} + (D_{FFT}^2 C_i^n)_j + (D_{m+1}^2 C_i^{n+1})_j \right),$$

Here, since C^n is known the differentiation on vector C_j^n is taken via FFT and this operation is denoted by D_{FFT} .

The discretizations (4.26) and (4.27) are semi-implicit, and the resulting systems are solved by Gaussian elimination or GMRES. With the above schemes, the numerical simulation is spectrally accurate in space and second order in time.

We remark here that the numerical method discussed in this chapter can also be applied to the case of an axisymmetric three-dimensional drop that is subject to an axisymmetric extensional flow. Suppose that a general interface in three-dimensions $r = R(z, \theta)$ is parameterized by the axial coordinate z and the azimuthal angle θ in cylindrical coordinates. To obtain the fluid velocity and interface shape, we use the same boundary integral equation (3.28) but where the fundamental solutions $G_{ij}(\mathbf{y}, \mathbf{x})$ and $T_{ijk}(\mathbf{y}, \mathbf{x})$ are those of the axisymmetric geometry. Because of the axisymmetry, i.e., because the flow and interface shape are independent of the azimuthal angle θ , $r = R(z)$ and in the surface integrals over z and θ in the boundary integral equation the integration with respect to θ can be carried out analytically so that the integrals are reduced to integrals over z alone in a meridional plane. Hence, the

numerical method of this chapter can be extended to solve the axisymmetric case with high-order accuracy.

CHAPTER 5

RESULTS OF NUMERICAL SIMULATION

In this chapter, numerical results of simulations for the evolution of the drop shape or profile and the surfactant concentration both on the interface and in the bulk flow are presented in various examples.

In all simulations, the bulk surfactant concentration away from the transition layer is uniform with $C = 1$ for all t and the surface Péclet number is taken to be infinitely large.

The algorithm discussed in Chapter 4 is implemented in Matlab and all the computational times given below are for runs on a 2.4 GHz AMD Opteron Model processor.

Mechanistic description of drop dynamics with imposed flow and surfactant

When a drop or bubble is mildly strained or sheared in an imposed flow, the interfacial surface tension force tends to restore it to its equilibrium unstrained circular shape and oppose drop breakup. This holds with or without the presence of surfactant on the interface. From the stress-balance boundary condition (2.8), in the absence of surfactant the Marangoni stress $\nabla_s \sigma$ is zero and the only surface tension force is the capillary stress $\sigma \kappa \mathbf{n}$, which acts in the direction normal to the interface when the interface curvature $\kappa \neq 0$.

When surfactant is present on the drop interface, it reduces surface tension relative to its surfactant-free value. At relatively low surface surfactant concentrations, this reduction in surface tension implies that for a given strain-rate or given capillary number Q either a steady drop shape will be more elongated or the drop shape

becomes time-dependent and breaks up. In an extensional flow, there is a finite critical capillary number Q_c below which ($Q < Q_c$) a steady drop shape can occur and above which ($Q > Q_c$) the drop evolution is unsteady and the drop eventually breaks up. At relatively low surface surfactant concentration, Q_c decreases with increasing surface surfactant concentration, although Q_c tends to increase again at higher surface surfactant concentration. The physical significance of this non-monotone dependence of Q_c on surfactant concentration is discussed in [16] and [17], and additional data and discussion are given in [6].

The equation for evolution of surface surfactant is (2.11) in the general case or (2.24) in the large bulk Péclet number limit. As explained at the end of Section 2.3, the effect of surface diffusion is generally believed to be very small and is set to zero in the simulations of this dissertation, while solubility of surfactant is a central theme. In the absence of both surface diffusion and solubility, equations (2.11) and (2.22) imply that surfactant particles move as fluid particles on the interface. An imposed strain or shear therefore tends to convect or sweep surfactant with the flow at the interface, drawing it away from the relatively flat middle parts of the interface and concentrating it at the more highly curved downstream ends. This surface surfactant concentration gradient produces a Marangoni stress $\nabla_s \sigma$ which acts in the direction to oppose elongation of the drop. This is seen from the tangential component of the stress-balance boundary condition (2.8), where the net tangential viscous stress balances the Marangoni stress.

The presence of an insoluble diffusion-free surfactant on the surface of a strained drop therefore tends to promote drop breakup by reducing surface tension while the Marangoni stress acts to lessen or reduce this effect by opposing drop elongation.

Solubility of surfactant tends to reduce the gradient of surface surfactant concentration, and therefore reduce Marangoni stress. The mechanism for this is that, near the strained drop ends, the surface surfactant concentration Γ caused by

convection with the imposed flow becomes sufficiently high that the bulk surfactant concentration neighboring the interface $C|_{\partial\Omega}$ of equations (2.13) and (2.22) increases above the far field value $C = 1$ of equations (2.14) and (2.22). This induces a normal gradient in C that causes surfactant to leave the interface and enter the bulk, thereby reducing the local surface concentration. Conversely, on the relatively flat middle parts of the interface, from which Γ has been convected away by the imposed flow, Γ and $C|_{\partial\Omega}$ are below the far field value, so that surfactant tends to enter the interface from the bulk, thereby increasing the local surface concentration. We note that the influence of surface diffusion, if included, also tends to reduce gradients of Γ and thus reduce Marangoni stress.

The influence of the bulk-interface surfactant exchange parameter J of equation (2.11) or its scaled counterpart J_0 of equation (2.24) is such that in the limit of small J_0 the bulk and interface surfactant dynamics are decoupled, the surface surfactant behaves as though it is insoluble, and the dynamics for insoluble surfactant should be recovered. On the other hand, when J_0 is large surfactant exchanges readily between its dissolved or bulk form and its adsorbed or surface form, so that, as just explained above, surface concentration gradients are reduced. Then via the equation of state (2.9) surface tension gradients are reduced and the dynamics with reduced but constant surface tension, as in the surfactant-free case, should be recovered.

Scenario 1

We consider an inviscid drop, i.e., a bubble with $\lambda = 0$, suspended in a viscous surrounding fluid subject to an imposed strain with $Q = 0.25$ and $B = G = 0$. The bubble is initially circular with uniform distribution of surfactant on the interface $\Gamma(\alpha, t = 0) = 0.5$, while the surfactant concentration in the transition layer is $C(\alpha, N, t = 0) = 1$ at the initial time. We set the equilibrium partition coefficient $K = 1$, which implies that the surfactant concentration $\Gamma(\alpha, t = 0)$ on the interface and

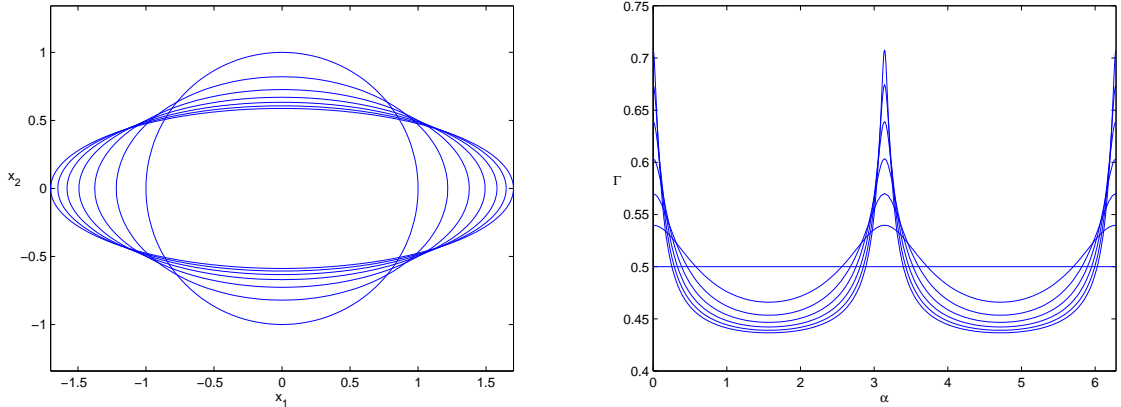


Figure 5.1 Scenario 1: An inviscid bubble driven by pure straining flow with $Q = 0.25$. The evolution of the bubble interface (left panel) and the surface surfactant concentration (right panel) are plotted from $t = 0$ to $t = 3.0$ in increments of 0.5. The horizontal line in the right panel indicates the initial concentration of the surfactant on the interface.

the surfactant concentration $C(\alpha, N = 0, t = 0)$ in the transition layer immediately adjacent to the interface are in equilibrium initially. In our simulation, the elasticity parameter $E = 0.1$ and the exchange coefficient $J_0 = 1$.

We use M equally spaced marker points to discretize the interface and the transition layer in the α -direction. Initially, we choose $M = 128$ in all examples presented in this chapter. At each time step, we check the Fourier modes of the interface profile and the surface surfactant concentration Γ by fast Fourier transform (FFT). If the Fourier modes near the Nyquist frequency of either quantity goes beyond Threshold 1 as introduced in Chapter 4, M is doubled as explained in Section 4.1.1.

Since no especially large gradients of the surfactant concentration are expected in the rescaled transition layer, a moderate number m of Chebyshev-Lobatto points can adequately resolve the surfactant concentration along the normal direction in the transition layer. For the results presented in this chapter, m is fixed in the course of each simulation and it can be chosen as small as $m = 64$.

The evolution of the bubble profile and the surface surfactant concentration are shown in Figure 5.1 from $t = 0$ to $t = 3.0$ in time increments of 0.5. By the end of the simulation M has been increased to 1024 while the time step Δt is constant with $\Delta t = 0.001$. As a check on the accuracy of the simulation, the relative error of the bubble area is less than 10^{-8} , see Figure 5.2. The CPU time required for this simulation is 2.4 hours.

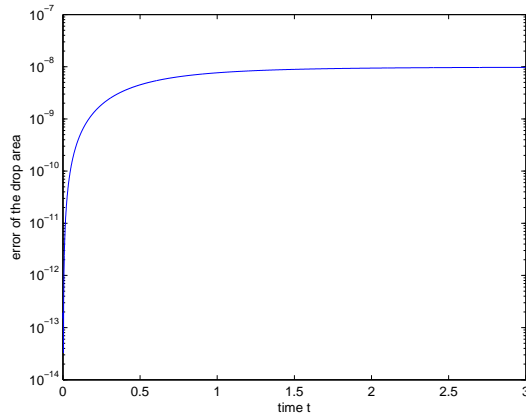


Figure 5.2 Scenario 1: Logarithm of the error of bubble area versus time t .

The thickness of the transition layer is scaled by $Pe^{-1/2}$. That is, the original normal distance coordinate n and the local normal coordinate N of the transition layer equation are related by

$$n = Pe^{-1/2}N. \quad (5.1)$$

This must be used to map the bulk concentration found in the computational domain of the transition layer back to the physical domain when presenting data for C . We show the bulk surfactant concentration with $Pe = 4,000$ at times $t = 1.0$ and $t = 3.0$ in Figure 5.3.

Consistent with the mechanistic description at the beginning of this chapter, we observe that a high concentration of surfactant occurs at the ends of the bubble in the

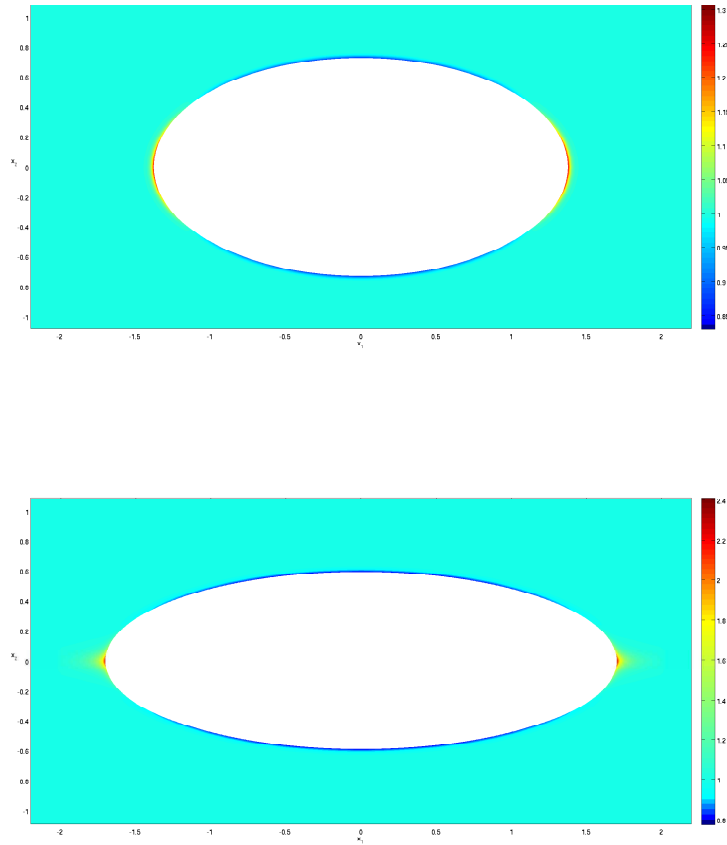


Figure 5.3 Scenario 1: Bubble shape and bulk surfactant concentration C at $t = 1.0$ (upper panel) and $t = 3.0$ (lower panel). $Pe = 4,000$.

transition layer, while a relatively low concentration develops at the ‘flat’ regions near the middle of the bubble. This occurs since the surfactant is “swept” or convected by the imposed flow to accumulate at the bubble ends, where it reaches a sufficiently high concentration to leave the interface due to surfactant solubility. This is borne out by comparing the right panel of Figure 5.1, which shows the evolution of Γ in time, with the bulk concentration seen in Figure 5.3. Initially, C and Γ are uniform and in equilibrium, but as time increases, on the flat middle parts of the interface Γ decreases so that $C|_{\partial\Omega}$ decreases below the far-field value of $C = 1$ and surfactant

enters the interface from the bulk, while near the interface ends the concentration of Γ increases to form a sharp peak or spike and the direction of exchange is reversed with surfactant leaving the interface for the bulk.

It is also important to note that the Péclet number Pe enters the problem via the scaling (5.1) alone, and is only needed after the simulation to present visual data for C . In other words, Pe is a post-process parameter for the simulation. The magnitude of the bulk Péclet number Pe has no impact on the evolution of the bubble profile and the surface surfactant concentration. This is counterintuitive at a first glance. However, it follows when we notice that Pe is scaled out of the problem by our using the leading order transition layer equation (2.21), which is valid in the limit of infinite Péclet number. Further, the bulk surfactant concentration for different finite Péclet numbers is generated by using the results from only one infinite Péclet number simulation. If we choose $Pe = 1,600$ or $Pe = 12,000$, the thickness of the transition varies since C rescales as a function of N from (5.1). Data for the bulk surfactant concentration C at $t = 3.0$ are given in Figure 5.4 for these two values of Pe .

In this example, since the viscosity ratio $\lambda = 0$ there is a theoretical result that implies the profile maintains a purely elliptical shape with only its aspect ratio changing in time, and this is found in the simulation up to round-off error. The result is given in [7] following an earlier version in [44] and is shown by using conformal mapping techniques. It states that for an inviscid interior, if the initial profile is circular or elliptical and the imposed flow is either a pure strain or a simple shear then the profile remains elliptical for all time. This holds with soluble or insoluble surfactant as well as in the surfactant-free case, although the presence of surfactant influences the aspect ratio of the ellipse.

Scenario 2

In this example, we present a simulation in which a viscous drop is suspended in a slightly more viscous surrounding fluid. The viscosity ratio is $\lambda = 0.8$, and the

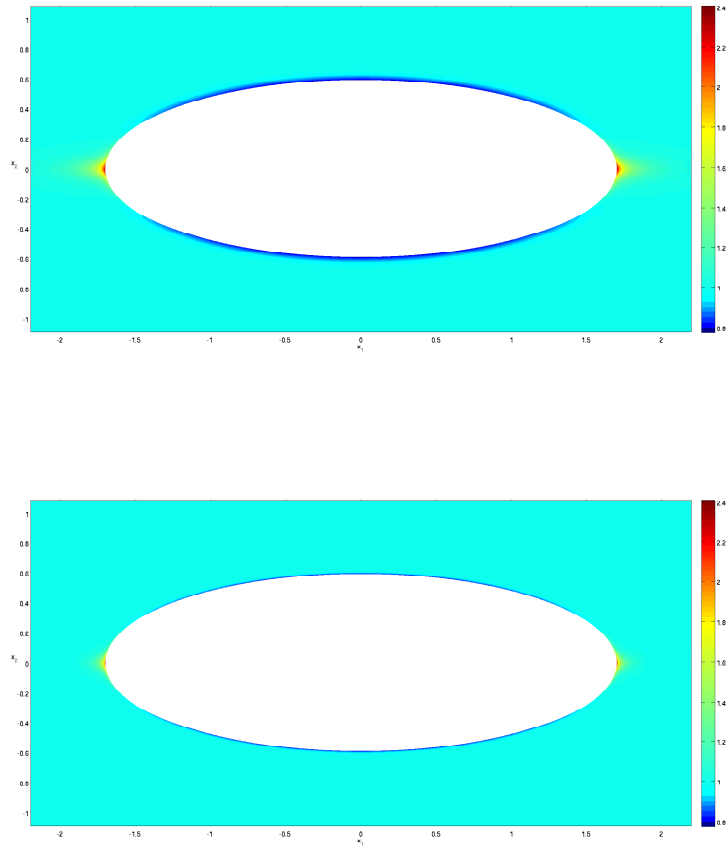


Figure 5.4 Scenario 1: Bubble shape and bulk surfactant concentration C at $t = 3.0$ for $Pe = 1,600$ (upper panel) and $Pe = 12,000$ (lower panel).

surface and bulk surfactant concentrations are not in equilibrium at the initial time, that is,

$$C(\alpha, N = 0, t = 0) \neq \frac{\Gamma(\alpha, t = 0)}{K(1 - \Gamma(\alpha, t = 0))}.$$

We choose $\Gamma(\alpha, t = 0) = 0.55$ for all α and $K = 1.5$ with $C(\alpha, N, t = 0) = 1$. Other physical parameters are $J_0 = 1.0$ and $E = 0.1$.

When a pure straining flow with $Q = 0.2$, $B = G = 0$ is imposed, the evolution of the drop profile and the surfactant concentration on the interface are shown in

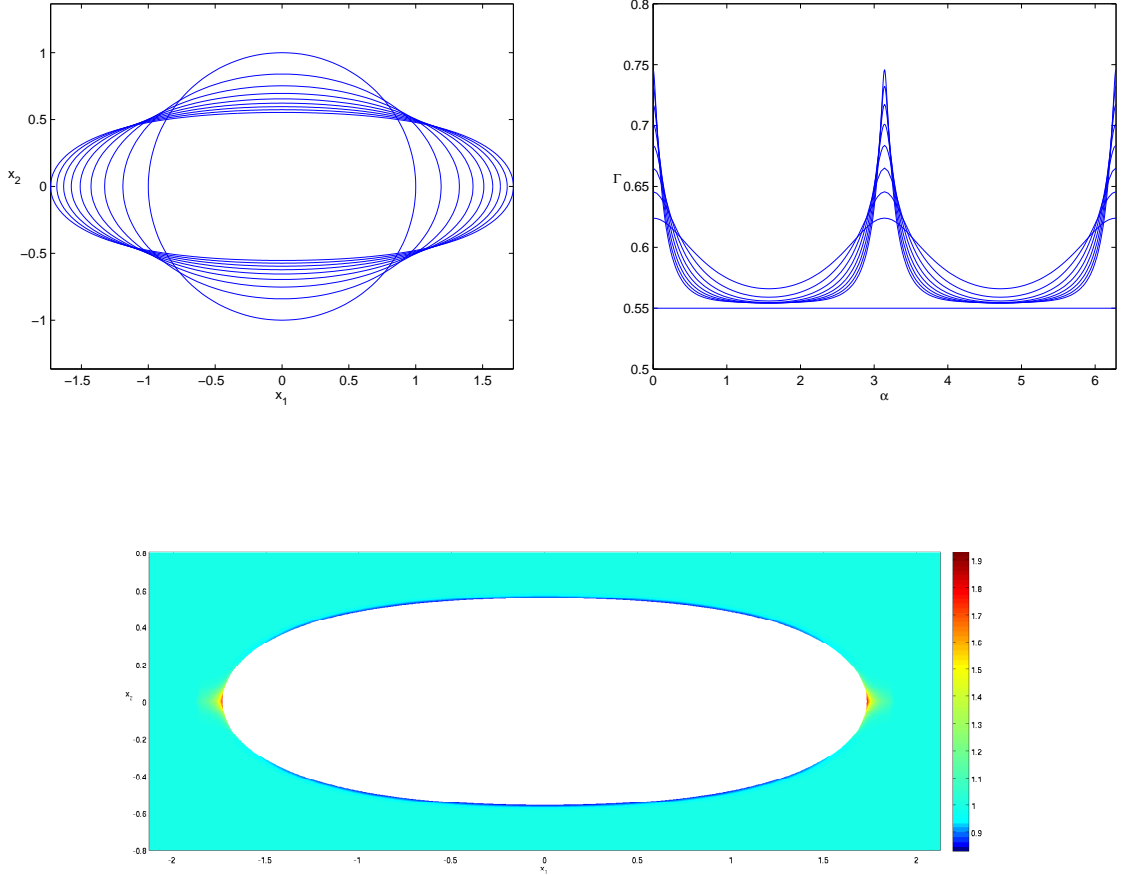


Figure 5.5 Scenario 2: A viscous drop in a pure strain with $Q = 0.2$. The interior-exterior viscosity ratio is $\lambda = 0.8$. The evolution of the bubble interface (upper left panel) and the surface surfactant concentration (upper right panel) are shown from $t = 0$ to $t = 8.0$ in increments of 1.0. The horizontal line in the upper right panel indicates the initial surfactant concentration on the interface. The bulk surfactant concentration C at $t = 8.0$ is shown in the lower panel for $Pe = 20,000$.

Figure 5.5 from $t = 0$ to $t = 8.0$ in time increments of 1.0. The simulation begins with 128 marker points on the interface, but at the end of the simulation, 1024 marker points are needed to resolve the interface, while we discretize the transition layer with $m = 64$ points in the normal direction. With the time step $\Delta t = 0.001$, the error of the drop area at the end of the simulation, when $t = 8.0$, is less than 10^{-8} , see Figure 5.6. The CPU time required for this simulation is 2.8 hours.

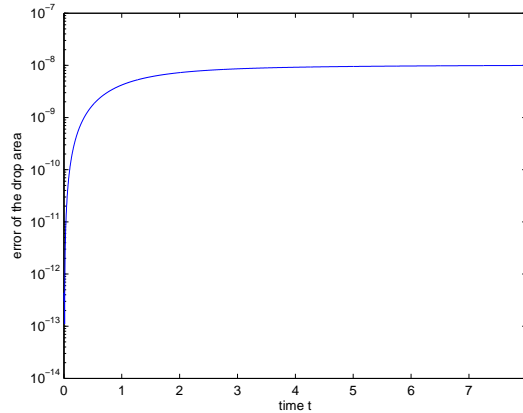


Figure 5.6 Scenario 2: The logarithm of the error in drop area versus time t .

In the data of Figure 5.5 we see that, with a viscous interior ($\lambda = 0.8 > 0$) the drop profile is no longer elliptical as time increases but is more “boxy” or square-shaped. At later times during the simulation, the exchange of surfactant due to solubility is as in Scenario 1, with surfactant entering the interface from the bulk at its flat middle part and leaving the interface at its ends. However, with the nonequilibrium initial data of this example, the evolution of the surface concentration Γ shown in the upper right panel of the figure is such that there is an initial uptake of surfactant everywhere on the interface at early times.

Scenario 3

In this example, we consider an inviscid drop, i.e., a bubble with $\lambda = 0$, subject to an imposed linear shear flow with $G = -2B = -0.5$ and $Q = 0$. The surface surfactant concentration $\Gamma(\alpha, t = 0) = 0.6$ and the bulk surfactant concentration $C(\alpha, N = 0, t = 0) = 1$ are in equilibrium at the initial time since $K = 1.5$. We set $J_0 = 1$ and $E = 0.1$. As noted in Scenario 1, since the interior is inviscid ($\lambda = 0$) the profile is elliptical for all times.

In Figure 5.7 we see that the bubble elongates, with an increase of surface surfactant concentration near the bubble ends and a decrease of the surface surfactant

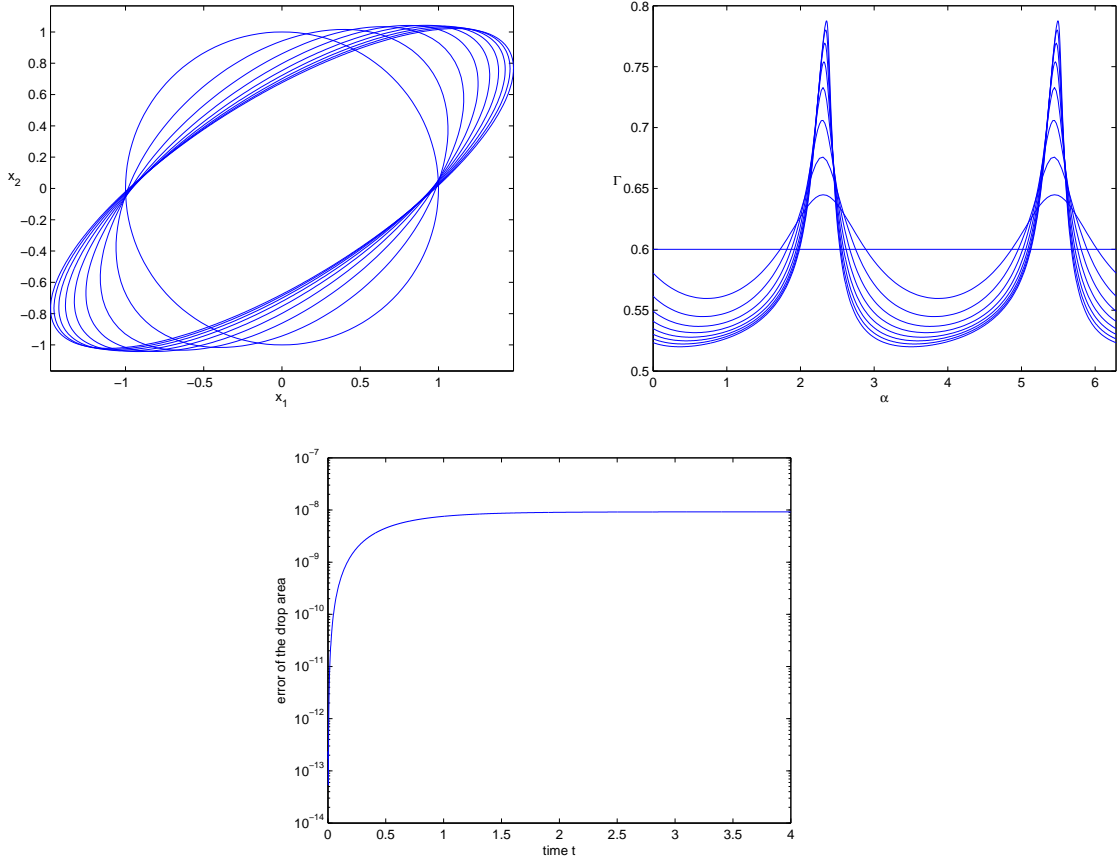


Figure 5.7 Scenario 3: An inviscid bubble is stretched by a linear shear flow with shear rate $G = -2B = -0.5$. The evolution of the bubble profile (upper left panel) and the surface surfactant concentration (upper right panel) are shown from $t = 0$ to $t = 4.0$ in increments of 0.5. The lower panel shows the logarithm of the error in drop area versus time t .

concentration near the middle of the bubble. This is consistent with the plot of the bulk surfactant concentration in the transition layer at the final time of the simulation $t = 4.0$ as shown in Figure 5.8, which is shown with the fairly moderate value $Pe = 8,000$ so that the transition is clearly visible. The number of marker points used in this simulation increases from $M = 128$ to $M = 512$ and the step size in time is $\Delta t = 0.001$. The drop area is conserved up to an error of about 10^{-9} , see Figure 5.7. The CPU time required for this simulation is 4.6 hours.

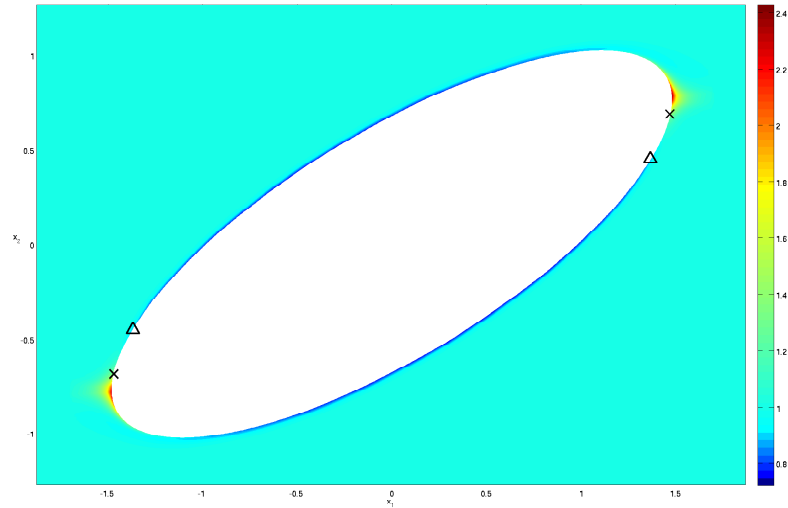


Figure 5.8 Scenario 3: Bulk surfactant concentration C at $t = 4.0$ with $Pe = 8,000$. The markers on the interface indicate the location of stagnation points. A cross indicates a stagnation point with converging flow on the interface and a triangle indicates a stagnation point with diverging flow on the interface.

It is a well-known feature, that when a drop or bubble is stretched in a linear shear flow the longer axis of the deformed shape is not aligned with the direction of the shear, as seen in Figures 5.7 and 5.8. Also, there is a nonzero vorticity associated with the imposed shear and a nonzero circulation around the bubble surface. The markers on the interface in Figure 5.8 indicate the presence and location of stagnation points in this example, so that there are two small regions on the interface where the circulation is seen to reverse from its usual clockwise direction to a counter-clockwise direction.

Scenario 4

Here we present a second example of a drop driven by a linear shear flow, but with $G = -2B = -1.0$ and $Q = 0$ the imposed shear is stronger, and now the ratio of the viscosity of the drop to that of the exterior fluid is $\lambda = 1.2$. As in the previous example, the initial surface surfactant concentration is $\Gamma(\alpha, t = 0) = 0.6$, the initial

bulk concentration is $C(\alpha, N, t = 0) = 1$, and $K = 1.5$ so that Γ and C are in equilibrium at the initial time. The values of J_0 and E are same as in the last three examples, i.e., $J_0 = 1$ and $E = 0.1$.

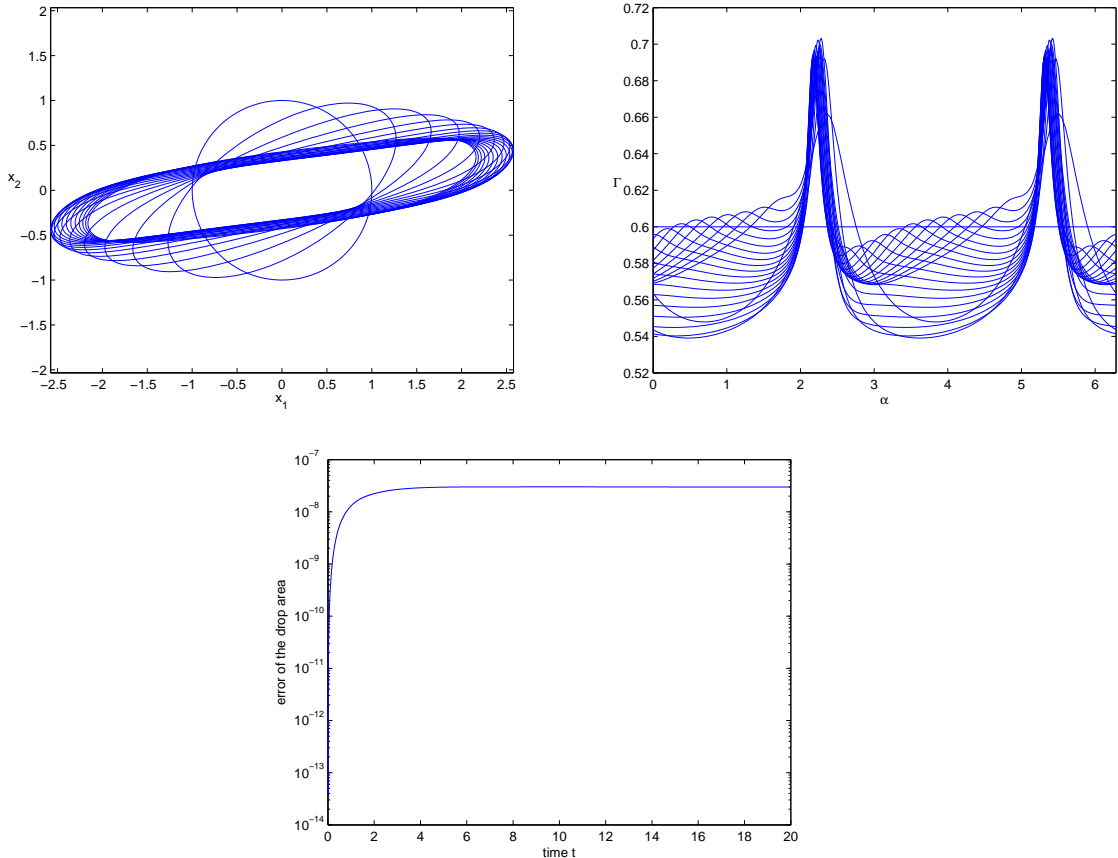


Figure 5.9 Scenario 4: A viscous drop is stretched by a linear shear flow with shear rate $G = -2B = -1$. The interior-exterior viscosity ratio is 1.2. The evolution of the bubble profile (left panel) and the surface surfactant concentration (right panel) are shown from $t = 0$ to $t = 20.0$ in increments of 1.0. The lower panel shows the logarithm of the error in drop area versus time t .

In Figure 5.9 we see that the drop elongates during the first half of the simulation but then decreases in length and increases in width during the second half of the simulation, i.e., its aspect ratio first increases and then decreases. In Figure 5.10, it is seen that the concentration of the bulk surfactant in the transition layer at the ends and at the waist of the drop are respectively higher and lower than the far field value

of the bulk concentration $C = 1$, as in Scenario 3. Here $Pe = 15,000$, which is quite realistic in applications. The number of the marker points used in this simulation increases from $M = 128$ to $M = 1024$ and the step size in time is $\Delta t = 0.001$. The drop area is conserved up to an error of about 10^{-9} , see Figure 5.9. The CPU time required for this simulation is 47.6 hours.

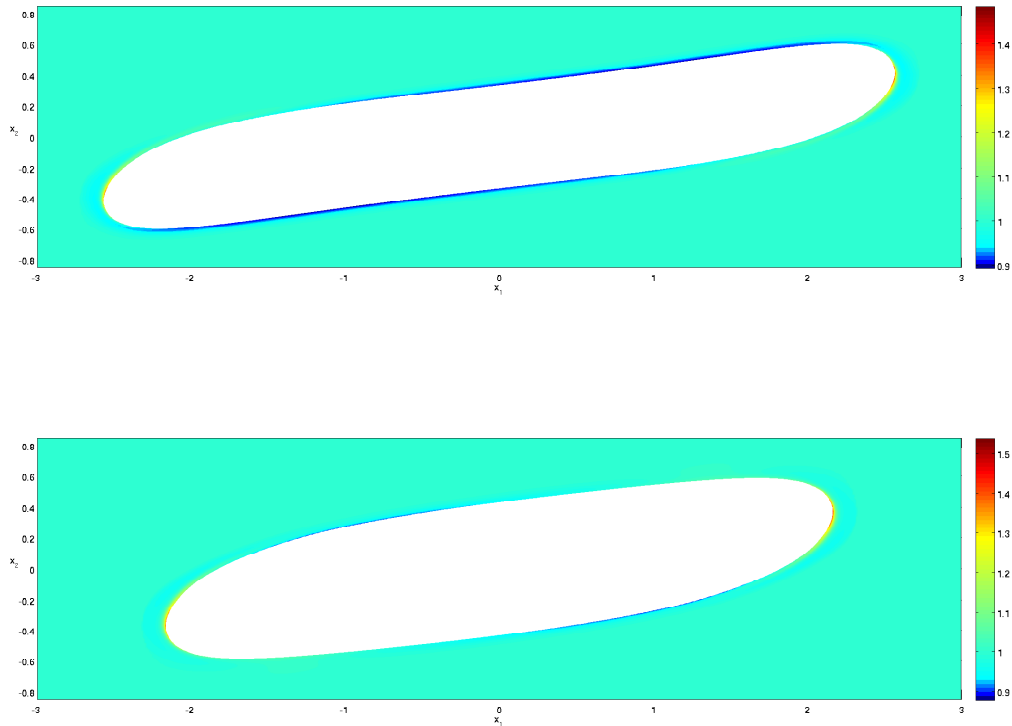


Figure 5.10 Scenario 4: Bulk surfactant concentration C at $t = 10.0$ (upper panel) and $t = 20.0$ (lower panel) for $Pe = 15,000$. Note the decrease in aspect ratio at later times.

We note that in this example, there are no stagnation points on the interface. That is, the circulation is always clockwise and the drop “tank-treads”. From the data for the surface surfactant concentration Γ shown in the upper right panel of Figure 5.9, it is seen that at early times in the initial stage of drop elongation, from time $t = 0$ to $t \simeq 3$ the surface surfactant concentration evolves in a way that is

qualitatively similar to that of the previous example, Scenario 3, in that Γ decreases over much of the flat section of the interface, where surfactant enters the interface from the bulk due to solubility, and Γ forms peaks or spikes at the curved drop ends, where surfactant leaves the interface for the bulk, although the magnitude of the peaks in Scenario 4 tends to be less than in Scenario 3.

However, during later times in the stage of drop elongation from $t \simeq 3$ to $t \simeq 8$ although the spikes remain at near-constant amplitude, everywhere on the troughs or regions of low Γ on the flat section of the interface the surface surfactant concentration of Scenario 4 steadily increases toward its equilibrium value of $\Gamma = 0.6$. For times greater than $t \simeq 8$ the second phase of the evolution occurs in which the drop length decreases or the drop retracts. The data of Figure 5.9 for Γ show that in this time interval Γ continues to increase over one part of the flat section of the interface but begins to decrease on another part, which steadily increases in size. At the same time, the magnitude of the peaks in Γ decreases and their width increases. The net result is that the drop profile retracts toward a less elongated and more circular shape at the same time as the surface surfactant concentration Γ becomes more evenly distributed. It is possible that the time scale of this second phase, i.e., of drop retraction, is related to the time scale of the interface tank-treading. This is a topic for continuing study.

CHAPTER 6

SOLUTION OF THE TRANSITION LAYER EQUATION VIA A GREEN'S FUNCTION

A computational profile analysis shows that when the numerical method described in Chapter 4 is used one of the most time-consuming parts of the numerical simulation is the computation of the bulk surfactant concentration C . This is due to the fact that first we need to discretize the computational domain of the transition layer for C with $M \times m$ points and then, to obtain second order accuracy in time, we compute $C_{i,j}$ via the two-step variation of the Crank-Nicolson method (4.26) and (4.27), which requires inverting the second derivative Chebyshev differentiation matrix D_{M+1}^2 twice for each time step. Moreover, the complexity increases significantly when M has to be doubled in order to resolve the interface shape and surface surfactant concentration accurately as the drop deformation increases.

At this point, we ask if there is an exact solution to the convection-diffusion problem (4.22a)-(4.22c). Since the problem is linear and has structure similar to the classical heat or diffusion equation, it seems likely that a solution to the problem can be found in terms of a fundamental solution or Green's function. If a Green's function representation of the solution can be found, then we can solve the problem for C by using information on the boundary alone without the need to build a mesh and solve throughout the computational domain, which lowers the dimension of the problem and significantly reduces the computational complexity.

Fortunately, such a “mesh-free” solution exists and we devote the first section of this chapter to its derivation. The numerical method using this solution is given in Section 2 of this chapter, and is followed by numerical results and discussion in Section 3.

6.1 The Analytical Solution by a Green's Function Representation

For convenience, we restate the problem (4.22a)-(4.22c) here.

$$\frac{\partial C}{\partial t} + v_s(s, t) \frac{\partial C}{\partial s} + \psi(s, t) N \frac{\partial C}{\partial N} = \frac{\partial^2 C}{\partial N^2}, \quad (6.1a)$$

$$\text{where } \psi(s, t) = - \left(\kappa u_n + \frac{\partial u_s}{\partial s} \right),$$

$$\text{initial condition: } C(s, N, t = 0) = 1, \quad (6.1b)$$

$$\text{boundary conditions: } C(s, N = 0, t) = \frac{\Gamma(s, t)}{K(1 - \Gamma(s, t))},$$

$$\text{and } C(s, N = \infty, t) = 1. \quad (6.1c)$$

The coordinate s is arc length along the interface (see Figure 4.1), N is normal distance from the interface, and t is time.

We introduce characteristic paths, which are defined as the solution of

$$\frac{\partial s}{\partial t} = v_s(s, t), \text{ with } s = s_0 \text{ at } t = 0, \quad (6.2)$$

and which are denoted by

$$s = f(s_0, t). \quad (6.3)$$

Since $v_s(s, t)$ is the tangential fluid velocity on the interface in the intrinsic coordinate frame, the characteristic coordinate s_0 is a label for material particle paths, i.e., s_0 is a Lagrangian coordinate on the interface. We now change variables from the coordinate frame (s, N, t) to the frame (s_0, N, t) using (6.3) with the normal coordinate N and time t unchanged. Under this transformation

$$\left. \frac{\partial}{\partial t} \right|_{s, N} \mapsto \left. \frac{\partial}{\partial t} \right|_{s_0, N} + \left. \frac{\partial s_0}{\partial t} \right|_{s, N} \left. \frac{\partial}{\partial s_0} \right|_{N, t} = \left. \frac{\partial}{\partial t} \right|_{s_0, N} - \left. \frac{v_s}{f_{s_0}} \frac{\partial}{\partial s_0} \right|_{N, t}, \quad (6.4a)$$

$$\left. \frac{\partial}{\partial s} \right|_{N, t} \mapsto \left. \frac{\partial s_0}{\partial s} \right|_{N, t} \left. \frac{\partial}{\partial s_0} \right|_{N, t} = \frac{1}{f_{s_0}} \left. \frac{\partial}{\partial s_0} \right|_{N, t}, \quad (6.4b)$$

$$\left. \frac{\partial}{\partial N} \right|_{s, t} \mapsto \left. \frac{\partial}{\partial N} \right|_{s_0, t}, \quad (6.4c)$$

where $f_{s_0} = \partial_{s_0} f$ and $v_s = \partial_t f$. The convective term $v_s \partial_s C$ of (6.1a) is absorbed into the time derivative in the new frame. The function $\psi(s, t)$ becomes

$$\psi(s_0, t) = \psi(s = f(s_0, t), t), \quad (6.5)$$

and (6.1a) to (6.1c) becomes

$$\frac{\partial C}{\partial t} + \psi(s_0, t) N \frac{\partial C}{\partial N} = \frac{\partial^2 C}{\partial N^2}, \quad (6.6a)$$

$$\text{initial condition: } C(s_0, N, t = 0) = 1, \quad (6.6b)$$

$$\text{boundary conditions: } C(s_0, N = 0, t) = \frac{\Gamma(s_0, t)}{K(1 - \Gamma(s_0, t))} \equiv h(s_0, t) + 1$$

$$\text{and } C(s_0, N = \infty, t) = 1. \quad (6.6c)$$

Here $\Gamma(s_0, t)$ is defined by $\Gamma(s_0, t) = \Gamma(s = f(s_0, t), t)$ analogously to (6.5).

As pointed out below equation (6.3) that this is a change of variables from arc length s to particle paths s_0 on the drop interface, i.e., s_0 is a Lagrangian coordinate on the interface, and in this frame $\frac{\partial C}{\partial t}$ is the time derivative along the particle paths, i.e., it is the material derivative. Since s_0 only appears parametrically in (6.6a) to (6.6c), we temporarily suppress the dependence on s_0 by putting

$$\psi_0(t) = \psi(s_0, t) \text{ and } h_0(t) = h(s_0, t). \quad (6.7)$$

Next we transform to homogeneous initial and far-field conditions by putting

$$\tilde{C} = C - 1 \quad (6.8)$$

and then drop the tilde, to find

$$\frac{\partial C}{\partial t} + \psi_0(t) N \frac{\partial C}{\partial N} = \frac{\partial^2 C}{\partial N^2}, \quad (6.9a)$$

$$\text{initial condition: } C(N, t = 0) = 0, \quad (6.9b)$$

$$\begin{aligned} \text{boundary conditions: } C(N = 0, t) &= h_0(t) \\ \text{and } C(N = \infty, t) &= 0. \end{aligned} \quad (6.9c)$$

To find the solution of (6.9a)-(6.9c) we use Duhamel's principle [22], [40], which states that the solution of (6.9a)-(6.9c) with its time-dependent boundary condition $C(N = 0, t) = h_0(t)$ can be expressed in terms of the solution of the problem with a piecewise constant step function boundary condition that is input at arbitrary time. This is the solution $u(N, t, \tau)$ of the problem

$$\frac{\partial u}{\partial t} + \psi_0(t) N \frac{\partial u}{\partial N} = \frac{\partial^2 u}{\partial N^2}, \quad (6.10a)$$

$$\text{with } u(N, t, \tau) = 0 \quad \text{for } 0 \leq t \leq \tau \quad (\tau \text{ arbitrary}), \quad (6.10b)$$

$$\begin{aligned} \text{boundary conditions: } u(N = 0, t, \tau) &= 1 \text{ for } 0 \leq \tau < t, \\ \text{and } u(N = \infty, t, \tau) &= 0. \end{aligned} \quad (6.10c)$$

In terms of $u(N, t, \tau)$ and $h_0(t)$, the solution of (6.9a)-(6.9c) is

$$\begin{aligned} C(N, t) &= \int_0^t u(N, t, \tau) \frac{\partial h_0}{\partial \tau}(\tau) d\tau + u(N, t, 0)h_0(0) \\ &= - \int_0^t \frac{\partial u}{\partial \tau}(N, t, \tau)h_0(\tau) d\tau, \end{aligned} \quad (6.11)$$

where τ is a dummy variable and integration by parts is used to obtain the last equation of (6.11).

To solve (6.10a)-(6.10c) we look for an error function-like solution and introduce a similarity variable

$$\eta(N, t) = \frac{N}{\gamma(t)}. \quad (6.12)$$

Here, $\gamma(t)$ is a function of time that is to be found. Although the data (6.10b)-(6.10c) for u is time-invariant, i.e., it does not change under a translation in t , the PDE (6.10a) is not time-invariant simply because of the time-dependence of $\psi_0(t)$. As a consequence, u and γ are functions of t and τ separately, not solely via the combination $t - \tau$. They are also dependent parametrically on s_0 , via the dependence of $\psi_0(t)$ on s_0 . By the chain rule, the derivatives with respect to t and N transform as

$$\partial_t \mapsto \partial_t - \frac{\eta}{\gamma} \gamma_t \partial_\eta \quad \text{and,} \quad \partial_N \mapsto \frac{1}{\gamma} \partial_\eta. \quad (6.13)$$

We look for a solution that depends on t through η alone, so that on substituting (6.13) into (6.10a) and then setting $\partial_t = 0$ we have

$$-\frac{\eta}{\gamma} \gamma_t u_\eta + \psi_0 \eta u_\eta = \frac{1}{\gamma^2} u_{\eta\eta}.$$

Multiplying both sides of the last equation by $\frac{\gamma^2}{\eta u_\eta}$, we find that the left hand side is a function of t alone and the right hand side is a function of η alone. Since η and t are independent variables here, both sides are equal to a constant, Θ . Namely,

$$\psi_0(t) \gamma^2 - \gamma \gamma_t = \frac{u_{\eta\eta}}{\eta u_\eta} = \Theta. \quad (6.14)$$

The value of Θ can be chosen arbitrarily, leading to a unique solution. This can be seen by noting that Θ is scaled out of (6.14) by setting $\eta' = \Theta^{\frac{1}{2}} \eta$ and $\gamma' = \Theta^{\frac{1}{2}} \gamma$, with $\eta' = N/\gamma'$. To facilitate the calculation, we set $\Theta = -2$, so that

$$\gamma \gamma_t - \psi_0(t) \gamma^2 = 2, \quad (6.15a)$$

$$u_{\eta\eta} + 2\eta u_\eta = 0. \quad (6.15b)$$

We anticipate an error function-like solution for u , where $\gamma = 0$ for $t \in [0, \tau]$ and $\gamma \rightarrow 0^+$ as $t \rightarrow \tau^+$. Putting $\Phi = \gamma^2$, we rewrite (6.15a) as

$$\Phi_t - 2\psi_0 \Phi = 4. \quad (6.16)$$

This can be integrated to give the solution

$$\Phi(t - \tau, \tau) = 4 \int_0^{t-\tau} e^{2 \int_{\tilde{t}}^{t-\tau} \psi_0(t'+\tau) dt'} d\tilde{t}, \quad (6.17)$$

which has the required behavior as $t \rightarrow \tau^+$. In terms of the function $a(t, \tau)$ defined by

$$a(t, \tau) = 2 \int_0^t \psi_0(t' + \tau) dt'. \quad (6.18)$$

the exponent in equation (6.17) is $a(t - \tau, \tau) - a(\tilde{t}, \tau)$ and the solution for γ can be written

$$\gamma(t - \tau, \tau) = 2 e^{\frac{1}{2}a(t-\tau, \tau)} \left(\int_0^{t-\tau} e^{-a(\tilde{t}, \tau)} d\tilde{t} \right)^{1/2}, \quad (6.19)$$

We note that the argument of ψ_0 in the solution (6.17) for Φ and in the definition (6.18) of a is advanced by τ . This is a consequence of the step function boundary data of (6.10b) and (6.10c) being zero for $t \in [0, \tau]$ and input to $u = 1$ at $t = \tau$, at which time $\psi_0(t) = \psi_0(\tau)$. In evaluating $\psi_0(t)$, we also note that during the interval $t \in [0, \tau]$ the original arc length coordinate $s = f(s_0, t)$ advances from its initial position $s = s_0 = f(s_0, 0)$ at time $t = 0$ to position $s = f(s_0, \tau)$ before the boundary data $u = 1$ is input at time $t = \tau$, and this is seen in the definition for $\psi_0(t) = \psi(s = f(s_0, t), t)$ of (6.5) and (6.7).

We now turn to (6.15b), which has the general solution

$$u(\eta) = c_1 \int_0^\eta e^{-\tilde{\eta}^2} d\tilde{\eta} + c_2. \quad (6.20)$$

The boundary conditions (6.10c) imply that for $t > \tau$ the solution is

$$u(\eta) = 1 - \frac{2}{\sqrt{\pi}} \int_0^\eta e^{-\tilde{\eta}^2} d\tilde{\eta} = 1 - \text{erf}(\eta),$$

where $\text{erf}(\eta) = -\frac{2}{\sqrt{\pi}} \int_0^\eta e^{-\tilde{\eta}^2} d\tilde{\eta}$ is the error function. The solution to the problem (6.10a)-(6.10c) with step function boundary condition is therefore

$$u(N, t, \tau) = 1 - \frac{2}{\sqrt{\pi}} \int_0^{\frac{N}{\gamma}} e^{-\tilde{\eta}^2} d\tilde{\eta} \quad \text{where } \gamma = \gamma(t - \tau, \tau), \quad (6.21)$$

the similarity variable $\eta = N/\gamma$ of (6.12) has been substituted, and $\gamma = \gamma(t - \tau, \tau)$ is given by (6.18) and (6.19).

Duhamel's principle (6.11) can now be applied. First, from (6.21), the time derivative of $u(N, t, \tau)$ is

$$\frac{\partial u}{\partial \tau}(N, t, \tau) = \frac{2N}{\sqrt{\pi}} e^{-\left(\frac{N}{\gamma}\right)^2} \frac{\partial_\tau \gamma}{\gamma^2} \quad \text{where } \gamma = \gamma(t - \tau, \tau) \quad (6.22)$$

then, changing the variable of integration in the convolution integral (6.11) from τ to $u = t - \tau$ and recalling (6.8), we have the solution of the problem (6.6a)-(6.6c) for C in the (s_0, N, t) Lagrangian frame in the form

$$C(s_0, N, t) = \frac{2N}{\sqrt{\pi}} \int_0^t e^{-\left(\frac{N}{\gamma}\right)^2} \frac{\partial_u \gamma}{\gamma^2} h_0(t - u) du + 1, \quad (6.23)$$

where $\gamma = \gamma(u, t - u)$.

It is worth summarizing that the parametric dependence of this solution on s_0 is given by the dependence of ψ_0 and h_0 on s_0 at equations (6.5), (6.6c), and (6.7), and by the dependence of a and γ on ψ_0 at (6.18) and (6.19). Also, in the limit when $\psi_0(t) = 0$ problem (6.6c) simplifies to the heat equation, and the expression for γ recovers the familiar result that $\gamma(u) = 4u$.

Since our ultimate goal is to find the normal derivative $\partial_N C$ at the interface in order to evaluate the bulk-interface surfactant exchange term, it is tempting to differentiate (6.23) directly under the integral sign and then take the limit as $N \rightarrow 0$. However, the limit can not be found in this way because of the behavior of $\gamma(u, t - u)$, which tends to zero as $u \rightarrow 0$. To circumvent this, we decompose the integral in

(6.23) in two parts, over $u \in [0, \delta]$ and $u \in [\delta, t]$ for some small $\delta > 0$, and treat each part separately. Before doing so, we first need the behavior of $\gamma(u, t - u)$ as $u \rightarrow 0$.

To find this, we note from equation (6.19) that

$$\gamma(u, t - u) = 2e^{\frac{1}{2}a(u, t-u)} \left(\int_0^u e^{-a(\tilde{t}, t-u)} d\tilde{t} \right)^{\frac{1}{2}}, \quad (6.24)$$

so that from the definition of a at (6.18), for small u ,

$$a(u, t - u) = 2 \int_0^u \psi_0(t' + t - u) dt' = 2\psi_0(t)u + O(u^2) \quad (6.25)$$

as $u \rightarrow 0$, with a similar result for $a(\tilde{t}, t - u)$. From these last results it follows that as $u \rightarrow 0$

$$\begin{aligned} \gamma(u, t - u) &= 2\sqrt{u} \left(1 + \frac{\psi_0(t)}{2}u + O(u^2) \right), \\ \gamma^2(u, t - u) &= 4u \left(1 + \psi_0(t)u + O(u^2) \right), \\ \partial_u \gamma(u, t - u) &= u^{-1/2} \left(1 + \frac{3\psi_0(t)}{2}u + O(u^2) \right). \end{aligned} \quad (6.26)$$

Now consider the contribution C_1 to the integral for C in (6.23) from $u \in [0, \delta]$ where δ is arbitrary but small and positive and $N \geq 0$. From (6.26), expansion of the integrand, assuming for example that h_0 is sufficiently smooth to have a Taylor expansion about $u = 0$, implies that

$$\begin{aligned} C_1(N, t) &= \frac{2Nh_0(t)}{\sqrt{\pi}} e^{\frac{\psi_0(t)N^2}{4}} \int_0^\delta \frac{e^{-\frac{N^2}{4u}}}{4u^{\frac{3}{2}}} (1 + O(u)) du \\ &= \frac{2h_0(t)}{\sqrt{\pi}} e^{\frac{\psi_0(t)N^2}{4}} \int_{\frac{N}{2\sqrt{\delta}}}^\infty e^{-s^2} \left(1 + O\left(\frac{N^2}{s^2}\right) \right) ds, \end{aligned}$$

where we have set $s = N/2\sqrt{u}$. In passing, we note that if we let $N \rightarrow 0$ in this last result the integral tends to $\sqrt{\pi}/2$ and C_1 approaches $h_0(t)$, so that C_1 recovers the boundary data for $C(s_0, N = 0, t) = 1 + h_0(t)$ of (6.10c). Returning to the derivative

$\partial_N C_1$, we find the contribution

$$\left. \frac{\partial C_1}{\partial N} \right|_{N=0} = -\frac{h_0(t)}{\sqrt{\pi\delta}} + O(\sigma^{\frac{1}{2}}). \quad (6.27)$$

To evaluate the contribution C_2 to the integral of (6.23) for $u \in [\delta, t]$, we note that since u is bounded away from zero $\gamma(u, t-u)$ is bounded away from zero, and the derivative with respect to N can be taken inside the integral directly. Then, letting $N \rightarrow 0$ and putting $\gamma^{-2}\partial_u\gamma = -\partial_u(\gamma^{-1})$ we have

$$\left. \frac{\partial C_2}{\partial N} \right|_{N=0} = -\frac{2}{\sqrt{\pi}} \int_{\delta}^t \frac{\partial}{\partial u} \left(\frac{1}{\gamma(u, t-u)} \right) h_0(t-u) du. \quad (6.28)$$

Integration by parts with the second of relations (6.26) for $\gamma(\delta, t-\delta)$ gives the contribution

$$\left. \frac{\partial C_2}{\partial N} \right|_{N=0} = \frac{h_0(t)}{\sqrt{\pi\delta}} + O(\delta^{\frac{1}{2}}) - \frac{2h_0(0)}{\sqrt{\pi}\gamma(t,0)} + \frac{2}{\sqrt{\pi}} \int_{\delta}^t \frac{1}{\gamma(u, t-u)} \frac{\partial}{\partial u} h_0(t-u) du. \quad (6.29)$$

The integral in this last expression converges when $\delta \rightarrow 0$, since $\gamma(u, t-u) \sim 2\sqrt{u}$ and the \sqrt{u} singularity is integrable. Combining the contributions (6.27) and (6.29), and then setting $\tau = t-u$ in the convolution integral, we find the result for the normal derivative of C at the interface, that

$$\left. \frac{\partial C}{\partial N} \right|_{N=0} = -\frac{2h_0(0)}{\sqrt{\pi}\gamma(t,0)} - \frac{2}{\sqrt{\pi}} \int_0^t \frac{\partial_{\tau} h_0(\tau)}{\gamma(t-\tau, \tau)} d\tau. \quad (6.30)$$

If the bulk and interface surfactant concentrations are in equilibrium initially, then $h_0(0) = 0$ and the first term of (6.30) is zero.

6.2 Numerical Method

In this section we present the numerical method that is used for updating the surface surfactant concentration $\Gamma(t)$ and for evaluating the convolution integral of equation (6.30) in the normal derivative of the bulk surfactant concentration at the interface

$\partial_N C|_{N=0}(s_0, t)$. The method uses a forward Euler scheme for stepping in time with integrals evaluated by the trapezoidal rule. It is therefore first order accurate in time.

We consider the general case when the interface and bulk surfactant concentrations are not in equilibrium at $t = 0$, that is when $h_0(0) \neq 0$ and the transition layer is deliberately excited or “tripped” by the initial data. For equilibrium initial data the method is simpler and is recovered as a special case of the method shown here by setting $h_0(0) = 0$. Also, in this section the dependence on the Lagrangian coordinate s_0 and specific indication that the derivative $\partial_N C$ is evaluated at $N = 0$ (i.e., on the interface $\partial\Omega$) is suppressed for simplicity, but we note that the time derivative $\partial_t \Gamma$ at equation (6.31) below is the time derivative following a particle path on the interface, i.e., at constant s_0 .

The system is written as

$$\frac{\partial \Gamma}{\partial t}(t) = \tilde{R}(t) + J_0 \frac{\partial C}{\partial N}(t), \quad (6.31)$$

$$\frac{\partial C}{\partial N}(t) = -\frac{2h_0(0)}{\sqrt{\pi}\gamma(t)} - \frac{2}{\sqrt{\pi}}I(t), \quad \text{where } I(t) = \int_0^t \frac{\partial_\tau h_0(\tau)}{\gamma(t-\tau, \tau)} d\tau, \quad (6.32)$$

$$\frac{\partial h_0}{\partial t}(t) = \frac{\partial_t \Gamma(t)}{K(1-\Gamma(t))^2}. \quad (6.33)$$

In equation (6.31), $\tilde{R}(t)$ contains the surface-flux, normal motion with curvature, and diffusive-flux contributions to the evolution of Γ of equation (2.24) as well as the modification necessary to transform to the Lagrangian frame. In other words $\tilde{R}(t)$ contains all contributions apart from the solubility or bulk-interface exchange term $J_0 \partial_N C$. In fact, for $\frac{\partial \Gamma}{\partial t}(t)$ in (6.31) to be the time derivative along particle paths, as required, in the parameterization $\mathbf{x} = \mathbf{X}(\xi, t)$ of the interface we simply set $\xi = s_0$. Then $\frac{\partial \mathbf{x}}{\partial t}|_{s_0}$ is the fluid velocity on the interface and $\frac{\partial \mathbf{x}}{\partial t}|_{s_0} \cdot \nabla_s \Gamma = \mathbf{u}_s \cdot \nabla_s \Gamma$. Therefore, $\tilde{R}(t)$ is

$$\tilde{R}(t) = \mathbf{u}_s \cdot \nabla_s \Gamma - \nabla_s \cdot (\Gamma \mathbf{u}_s) - \Gamma \kappa u_n + \frac{1}{Pe_s} \nabla_s^2 \Gamma.$$

Similarly, equation (6.33) follows on taking the time derivative of the definition of $h_0(t)$ along the particle paths.

Small time behavior. We need the behavior of the solution to the system (6.31) to (6.33) for small times both to compute the first time steps and, as we see below, to find the correct behavior of the convolution integral $I(t)$ in equation (6.32) that is needed to compute later time steps.

From the definition of $\gamma(t - \tau, \tau)$ at (6.24) and (6.25), its limiting behavior as $\tau \rightarrow t^-$ is given for any t by (6.24) as

$$\gamma(t - \tau, \tau) = 2(t - \tau)^{1/2}(1 + O(t - \tau)). \quad (6.34)$$

From this, considering t to be small and setting $\tau = 0$, if $h_0(0) \neq 0$, equation (6.32) implies that $\partial_N C(t)$ has the leading order behavior $\partial_N C(t) \sim -h_0(0)/(\sqrt{\pi}t^{1/2})$. We find that this in turn leads to a correction or remainder term that is $O(1)$ and given by the integral $I(t)$, since, from equations (6.31) and (6.33), we have the leading order behavior

$$\partial_N C(t) = -\frac{h_0(0)}{\sqrt{\pi}t^{1/2}} + O(1) \quad (6.35)$$

$$\partial_t \Gamma(t) = -\frac{J_0 h_0(0)}{\sqrt{\pi}t^{1/2}} + O(1) \quad (6.36)$$

$$\partial_t h_0(t) = -\frac{J_0 h_0(0)}{\sqrt{\pi}K(1 - \Gamma(0))^2 t^{1/2}} + O(1) \quad (6.37)$$

as $t \rightarrow 0$. This last result states that $\partial_t h_0(t)$ has an integrable $t^{-1/2}$ singularity at $t = 0$, or equivalently, the term $\partial_\tau h_0(\tau)$ in the integrand of $I(t)$ at equation (6.32) behaves like $\tau^{-1/2}$ as $\tau \rightarrow 0^+$. Combining this with the behavior of $\gamma(t - \tau, \tau)$ given at (6.34), we find that the integrand of $I(t)$ also has an integrable $(t - \tau)^{-1/2}$ singularity as $\tau \rightarrow t^-$. In other words, the integrand of $I(t)$ has integrable singularities at both end-points, $\tau = 0$ and $\tau = t$, and this holds for general or arbitrary times $t = O(1)$.

However, from (6.34) and (6.37), when t and hence $\tau \in [0, t]$ are both small, the integrand of $I(t)$ at (6.32) has the behavior

$$\frac{\partial_\tau h_0(\tau)}{\gamma(t-\tau, \tau)} = \frac{A_0}{2\tau^{1/2}(t-\tau)^{1/2}} + O((t-\tau)^{-1/2}, ((t-\tau)/\tau)^{1/2}), \quad (6.38)$$

$$\text{where } A_0 = -\frac{J_0 h_0(0)}{\sqrt{\pi} K(1-\Gamma(0))^2},$$

so that A_0 is the coefficient of the leading term on the right hand side of (6.37). Then, since

$$\int_0^t \frac{d\tau}{\tau^{1/2}(t-\tau)^{1/2}} = \pi,$$

we have

$$I(t) = \frac{A_0 \pi}{2} + O(t^{1/2}), \quad (6.39)$$

as $t \rightarrow 0$. This evaluates the $O(1)$ remainder term at (6.35) and leads to the following sequence of improved small time estimates:

$$\partial_N C(t) = -\frac{h_0(0)}{\sqrt{\pi} t^{1/2}} - \sqrt{\pi} A_0 + O(t^{1/2}), \quad (6.40)$$

$$\partial_t \Gamma(t) = -\frac{J_0 h_0(0)}{\sqrt{\pi} t^{1/2}} + (\tilde{R}(0) - \sqrt{\pi} J_0 A_0) + O(t^{1/2}), \quad (6.41)$$

$$\Gamma(t) = \Gamma(0) - \frac{2J_0 h_0(0)}{\sqrt{\pi}} t^{1/2} + (\tilde{R}(0) - \sqrt{\pi} J_0 A_0) t + O(t^{3/2}), \quad (6.42)$$

$$\partial_t h_0(t) = \frac{A_0}{t^{1/2}} + A_1 + O(t^{1/2}), \quad (6.43)$$

$$\text{where } A_1 = \frac{1}{K(1-\Gamma(0))^2} \left\{ \tilde{R}(0) + \frac{J_0^2 h_0(0)}{(1-\Gamma(0))} \left(\frac{1}{K(1-\Gamma(0))} + \frac{4h_0(0)}{\pi} \right) \right\}. \quad (6.44)$$

These results follow on noting that (6.32) with (6.34) and (6.39) implies (6.40), then (6.31) and (6.40) imply (6.41), which gives (6.42) on integration with respect to t , and then (6.33) with (6.41) and (6.42) implies (6.43) and (6.44).

Time step. The time step is taken using the forward Euler method,

$$\Gamma((n+1)\Delta t) = \Gamma(n\Delta t) + \partial_t \Gamma(n\Delta t) \Delta t, \quad (6.45)$$

where the derivative $\partial_t \Gamma(n\Delta t)$ is evaluated via the system (6.31) to (6.33).

Evaluation of the convolution integral

$$I(n\Delta t) = \int_0^{n\Delta t} \frac{\partial_\tau h_0(\tau)}{\gamma(t-\tau, \tau)} d\tau \quad (6.46)$$

in equation (6.32) is an important component of this. As just noted above, the integrand has integrable singularities due to the behavior (6.43) of $\partial_\tau h_0(\tau)$ as $\tau \rightarrow 0^+$ and the behavior (6.34) of $\gamma(t-\tau, \tau)$ as $\tau \rightarrow t^-$, so that the integration is carried out by the trapezoidal rule with the desingularization method of [35] applied at the end-points. We therefore decompose $I(n\Delta t)$ into the sum of three parts, and evaluate each part separately.

At the left hand end-point, the desingularization is given using the behavior (6.43) of $\partial_\tau h_0(\tau)$ as $\tau \rightarrow 0^+$, so that

$$\begin{aligned} I_1(n\Delta t) &\equiv \int_0^{\Delta t} \frac{\partial_\tau h_0(\tau)}{\gamma(n\Delta t - \tau, \tau)} d\tau \\ &= \int_0^{\Delta t} \frac{\partial_\tau h_0(\tau)}{\gamma(n\Delta t - \tau, \tau)} - \frac{1}{\gamma(n\Delta t, 0)} \left(\frac{A_0}{\tau^{1/2}} + A_1 \right) d\tau \\ &\quad + \frac{1}{\gamma(n\Delta t, 0)} \int_0^{\Delta t} \frac{A_0}{\tau^{1/2}} + A_1 d\tau \end{aligned} \quad (6.47)$$

$$= \frac{\partial_t h_0(\Delta t) \Delta t}{2\gamma((n-1)\Delta t, \Delta t)} + \frac{1}{2\gamma(n\Delta t, 0)} (3A_0(\Delta t)^{1/2} + A_1 \Delta t), \quad (6.48)$$

where the first (desingularized) integral at (6.47) is evaluated by the trapezoidal rule and the second integral is evaluated analytically. Similarly, at the right hand end-point, the desingularization is given using the behavior (6.34) of $\gamma(t-\tau, \tau)$ as

$\tau \rightarrow t^-$, so that

$$\begin{aligned}
I_3(n\Delta t) &\equiv \int_{(n-1)\Delta t}^{n\Delta t} \frac{\partial_\tau h_0(\tau)}{\gamma(n\Delta t - \tau, \tau)} d\tau \\
&= \int_{(n-1)\Delta t}^{n\Delta t} \frac{\partial_\tau h_0(\tau)}{\gamma(n\Delta t - \tau, \tau)} - \frac{\partial_t h_0(n\Delta t)}{2(n\Delta t - \tau)^{1/2}} d\tau \\
&\quad + \partial_t h_0(n\Delta t) \int_{(n-1)\Delta t}^{n\Delta t} \frac{d\tau}{2(n\Delta t - \tau)^{1/2}} \\
&= \frac{\partial_t h_0((n-1)\Delta t) \Delta t}{2\gamma(\Delta t, (n-1)\Delta t)} + \frac{3}{4} \partial_t h_0(n\Delta t) (\Delta t)^{1/2}. \tag{6.49}
\end{aligned}$$

Over the rest of the domain, the integrand is non-singular, and the trapezoidal rule gives

$$\begin{aligned}
I_2(n\Delta t) &\equiv \int_{\Delta t}^{(n-1)\Delta t} \frac{\partial_\tau h_0(\tau)}{\gamma(n\Delta t - \tau, \tau)} d\tau \\
&= \Delta t \left(\sum_{j=1}^{n-1} \frac{\partial_t h_0((n-j)\Delta t)}{\gamma(j\Delta t, (n-j)\Delta t)} - \frac{\partial_t h_0(\Delta t)}{2\gamma((n-1)\Delta t, \Delta t)} - \frac{\partial_t h_0((n-1)\Delta t)}{2\gamma(\Delta t, (n-1)\Delta t)} \right). \tag{6.50}
\end{aligned}$$

Summing (6.48) to (6.50) gives an expression for $I(t)$, namely

$$\begin{aligned}
I(n\Delta t) &= \frac{1}{2\gamma(n\Delta t, 0)} (3A_0(\Delta t)^{1/2} + A_1\Delta t) \\
&\quad + \Delta t \sum_{j=1}^{n-1} \frac{\partial_t h_0((n-j)\Delta t)}{\gamma(j\Delta t, (n-j)\Delta t)} + \frac{3}{4} \partial_t h_0(n\Delta t) (\Delta t)^{1/2}, \tag{6.51}
\end{aligned}$$

for $n = 2, 3, \dots$. Notice that this contains the derivative $\partial_t h_0(n\Delta t)$ at $t = n\Delta t$.

When the expression (6.51) for $I(n\Delta t)$ is substituted in equation (6.32) to find $\partial_N C(n\Delta t)$, equation (6.31) provides a linear relation between $\partial_t \Gamma(n\Delta t)$ and $\partial_t h_0(n\Delta t)$. After simple algebraic manipulation, on defining

$$\begin{aligned}
F(n\Delta t) &= -\frac{2J_0}{\sqrt{\pi}} \left(\frac{1}{\gamma(n\Delta t, 0)} \left[h_0(0) + \frac{3A_0(\Delta t)^{1/2}}{2} + \frac{A_1\Delta t}{2} \right] \right. \\
&\quad \left. + \Delta t \sum_{j=1}^{n-1} \frac{\partial_t h_0((n-j)\Delta t)}{\gamma(j\Delta t, (n-j)\Delta t)} \right), \tag{6.52}
\end{aligned}$$

this relation can be written as

$$\partial_t \Gamma(n\Delta t) = (\tilde{R}(n\Delta t) + F(n\Delta t)) - \frac{3J_0(\Delta t)^{1/2}}{2\sqrt{\pi}} \partial_t h_0(n\Delta t). \quad (6.53)$$

A second relation between $\partial_t \Gamma(n\Delta t)$ and $\partial_t h_0(n\Delta t)$ is given by equation (6.33) with $t = n\Delta t$. Elimination of $\partial_t h_0(n\Delta t)$ then gives the required result, that

$$\partial_t \Gamma(n\Delta t) = (\tilde{R}(n\Delta t) + F(n\Delta t)) \left(1 + \frac{3J_0(\Delta t)^{1/2}}{2\sqrt{\pi}K(1 - \Gamma(n\Delta t))^2} \right)^{-1} \quad (6.54)$$

$$\text{and } \partial_t h_0(n\Delta t) = \frac{\partial_t \Gamma(n\Delta t)}{K(1 - \Gamma(n\Delta t))^2}. \quad (6.55)$$

The time step for $\Gamma(n\Delta t)$ is given by (6.45) with (6.54), which requires the evaluation of $F(n\Delta t)$ as defined by (6.52). This expression for $F(n\Delta t)$ contains $\gamma(j\Delta t, (n-j)\Delta t)$ for $j = 1, \dots, n$, where the terms for $j = 1, \dots, n-1$ appear in the sum and the term for $j = n$ is outside the sum. Equivalently, it contains $\gamma((n-j)\Delta t, j\Delta t)$ for $j = 0, \dots, n-1$. To update these quantities we use the forward Euler method and trapezoidal rule. Introducing $L(t - \tau, \tau)$ given by

$$L(t - \tau, \tau) = \int_0^{t-\tau} e^{-a(\tilde{t}, \tau)} d\tilde{t},$$

$$\text{so that } \gamma(t - \tau, \tau) = 2e^{a(t-\tau, \tau)/2} (L(t - \tau, \tau))^{1/2}$$

from (6.19), the definition (6.18) for $a(t - \tau, \tau)$ gives the following scheme for the time update:

$$a((n+1-j)\Delta t, j\Delta t) = a((n-j)\Delta t, j\Delta t) + 2\psi_0(n\Delta t) \Delta t,$$

$$L((n+1-j)\Delta t, j\Delta t) = L((n-j)\Delta t, j\Delta t) + \frac{\Delta t}{2} \left(e^{-a((n+1-j)\Delta t, j\Delta t)} + e^{-a((n-j)\Delta t, j\Delta t)} \right),$$

$$\gamma((n+1-j)\Delta t, j\Delta t) = 2e^{a((n+1-j)\Delta t, j\Delta t)/2} (L((n+1-j)\Delta t, j\Delta t))^{1/2}.$$

The expression for $F(n\Delta t)$ also contains $\partial_t h_0(j\Delta t)$ for $j = 0, \dots, n-1$, for which the time update is given by (6.54) and (6.55).

The small time solution is used to start the computation. Equations (6.42) and (6.43) with $t = \Delta t$ give $\Gamma(\Delta t)$ and $\partial_t h_0(\Delta t)$ at the first time step. Equation (6.41) gives $\partial_t \Gamma(\Delta t)$ and the forward Euler scheme (6.45) is used to find $\Gamma(2\Delta t)$ at the second time step. The time stepping scheme of (6.52) and (6.54) can then be implemented to find $\partial_t \Gamma(2\Delta t)$ and to proceed to later times.

Remark. The computation of the sum that appears in $F(n\Delta t)$ of equation (6.52) can require a substantial amount of storage. Each term in the sum depends on the current time step via n and therefore needs to be recomputed at each step. This is an unavoidable consequence of carrying out a direct evaluation of the convolution integral $I(t)$ of equation (6.32). In the computations of Chapter 5 that use the Green's function method, we noted that typically $M = 200$ interface marker points are used with a time step of $\Delta t = 10^{-3}$ and a final run time of about $t = 3$. Toward the end of such a run, this requires storage of data across 200 marker points for each of 3,000 time steps.

Moreover, since the computation of Γ is along material particle paths, at each time step it is necessary to interpolate between the data for Γ on particle paths and the data at the marker points of the equal arc length frame that is used for the BIM fluid solver. This is done using a nonuniform fast Fourier transform or NUFFT, see [12], [13], and [20], which adds to the computational cost of the method. The need for interpolation can be circumvented if the BIM fluid solver also uses marker points that are particle paths, but then the spectral accuracy of the equal arc length frame is lost.

6.3 Results and Comparison of Numerical Simulations

In this section, we present the results of two numerical simulations that are obtained with the algorithm proposed in Section 6.2 and compare them with the results obtained by the mesh-based method of Chapter 5.

To implement the algorithm, as explained at the end of the last section, we need the values of $\gamma((n-j)\Delta t, j\Delta t)$, $h_t(j\Delta t)$, $a((n-j)\Delta t, j\Delta t)$, and $L((n-j)\Delta t, j\Delta t)$ for each j , with $0 \leq j \leq n$, along the particle paths. This requires a large amount of data storage. Further, when the equal arc length frame of Section 4.1.1 is used, we need to interpolate the values of each of the above quantities for each of n and j along each particle path by using the information we have at the equal arc length, equally distributed marker points. If the interpolation is done by using the nonuniform fast Fourier transform (NUFFT), the algorithm is extremely expensive due to an extra computational complexity caused by the interpolation tasks that is $O(n^2 M \log M)$.

Since our current objective is to verify the analytical solution of Section 6.1 and the algorithm of Section 6.2, we abandon the equal arc length frame and, instead, use computational marker points that track particle paths. Although this does not reduce the need for data storage, it significantly reduces the operation count associated with interpolation.

However, a drawback of using particle paths as marker points is their tendency to cluster in some places and become sparse in other places on the interface as the deformation increases. To overcome this, we use a strategy for redistributing the marker points that is due to Pozrikidis [33, 34].

According to this, after each time step we examine the distribution of marker points, and compute (a) the angle subtended by the circular arc passing through each successive triplet of marker points, and (b) the separation between any two successive marker points. If the angle subtended is too large, we increase the number of marker points locally by replacing the middle point with two evenly spaced points. Similarly,

if the separation between two successive points is too large we introduce a new point in the middle. On the other hand, if the separation between two successive points is too small, we replace the two points by a single point in the middle. The last operation is possible only if the resulting point distribution does not violate the first two criteria. This is an economical approach, which guarantees that the number of marker points throughout the course of the simulation remains nearly steady - unless the total interface arc length increases substantially. Moreover, it assures that all the above quantities $\gamma((n-j)\Delta t, j\Delta t)$ etc. are evaluated directly on the particle paths, hence avoiding interpolation between frames at each time step.

When a new marker point is introduced, the time history along the corresponding particle path is needed but this is computed efficiently by low order interpolation from the stored data.

Scenario 1

We return to the first Scenario of Chapter 5, for which the viscosity ratio $\lambda = 0$, the imposed flow is a pure strain with $Q = 0.25$, and other parameter values and initial conditions are as given there. Using the Green's function-based method of this chapter with the above method for following particle paths, we obtain the mesh-free data set for bubble shape and surface surfactant concentration that is shown by red solid markers in Figure 6.1.

In this simulation, we set the tolerance θ_{max} for the maximum angle subtended by the circular arc through successive triplet of marker points to be 0.25π and the upper and lower thresholds, S_{max} and S_{min} for distance between two successive marker points to be 0.1 and 0.04, respectively. We start the simulation with 128 marker points, and this number decreases to 108 by the end of the simulation. The time step we use is 0.01.

The data show that the results of the two methods are in very good visual agreement. Comparison of the data files for surface surfactant concentration shows

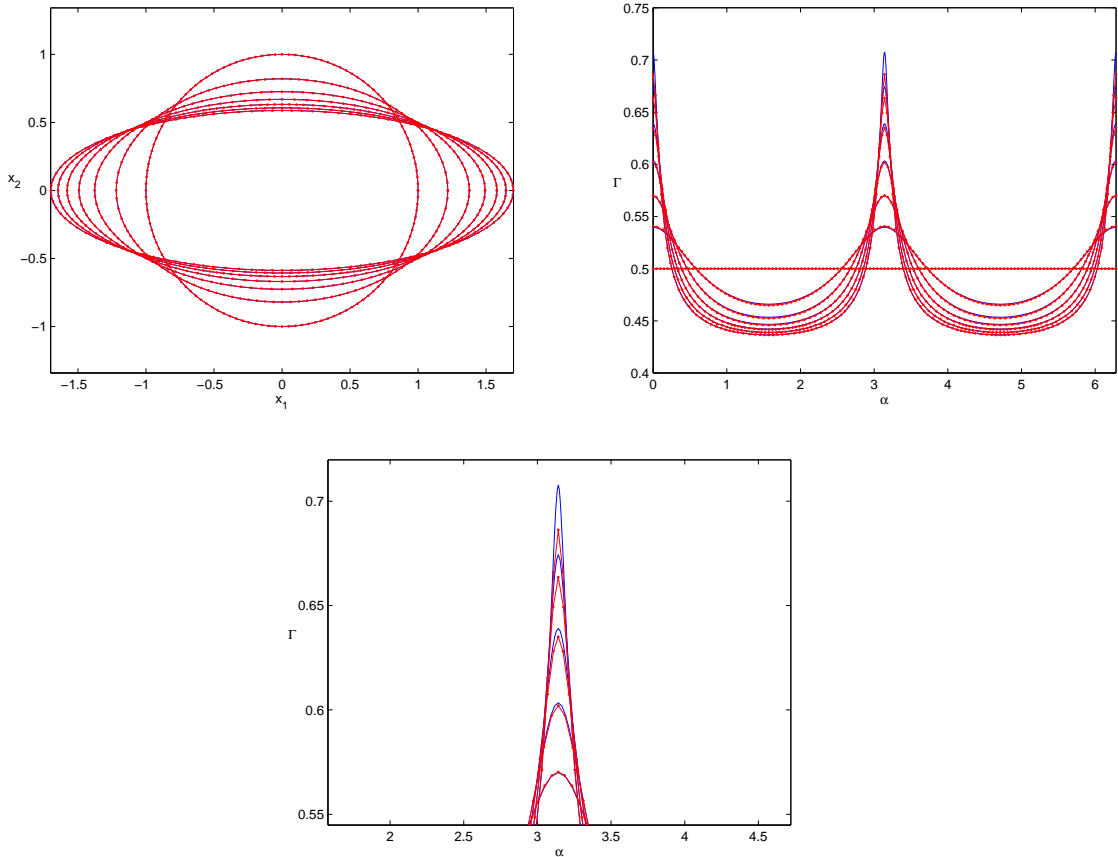


Figure 6.1 A return to Scenario 1 of Chapter 5. Comparison of simulation results using the Green's function method with simulation using the mesh-based method. The mesh-based method is shown by blue solid lines and the Green's function method is shown by red solid markers. The evolution of the bubble interface (upper left panel) and the surface surfactant concentration (upper right panel) are plotted from $t = 0$ to $t = 3.0$ in increments of 0.5. The lower panel gives a closeup of the spikes in Γ .

that the agreement between the results of the two methods is within 10^{-2} for all points on the interface except near the bubble end points for all times up to the final time $t = 3.0$ of the simulation run. The discrepancy in surfactant concentration is greater near the bubble ends and is caused by a low resolution of the spikes in Γ , see in the upper right panel of Figure 6.1. A closeup of this is shown in the lower panel of Figure 6.1. In principle, a combination of factors may impact the accuracy of the simulation, including the total number of marker points, the values of the tolerances

θ_{max} , S_{max} , and S_{min} , and the size of the time step. We suggest that the accuracy can be enhanced by using a finer discretization of the interface and a smaller time step, recalling as noted above that the current implementation of the mesh-free method is first order accurate in both space and time.

Scenario 2

Here we revisit the third scenario of Chapter 5, for which the viscosity ratio $\lambda = 0$, the imposed flow is a linear shear with $G = -2B = -0.5$, $Q = 0$, and other parameter values and initial conditions are as given there. Using the Green's function-based method of this chapter with the above method for following particle paths, we obtain the mesh-free data set for bubble shape and surface surfactant concentration shown by red solid markers in Figure 6.2.

In this simulation, we set the tolerance $\theta_{max} = 0.125\pi$, $S_{max} = 0.05$, and $S_{min} = 0.02$ respectively. The simulation starts with 256 marker points, and the number of the marker points decreases to 224 by the end of the simulation $t = 4.0$. The time step is 0.0025.

The data show that the results of the two methods are again in good visual agreement. Comparison of the data files for surface surfactant concentration shows that the difference between the results of the two methods is less than 10^{-2} for all points on the interface, except near the bubble end points, for all times up to the final time of the simulation run. The discrepancy in surfactant concentration is greatest near the bubble ends, due to low resolution of the spikes in Γ , see in the upper right panel of Figure 6.1 and a closeup of this in the lower panel of Figure 6.1.

Overall, the comparison of the two methods for the two given scenarios validates the analytical solution we derived in Section 6.1 and the proposed numerical algorithm suggested in Section 6.2.

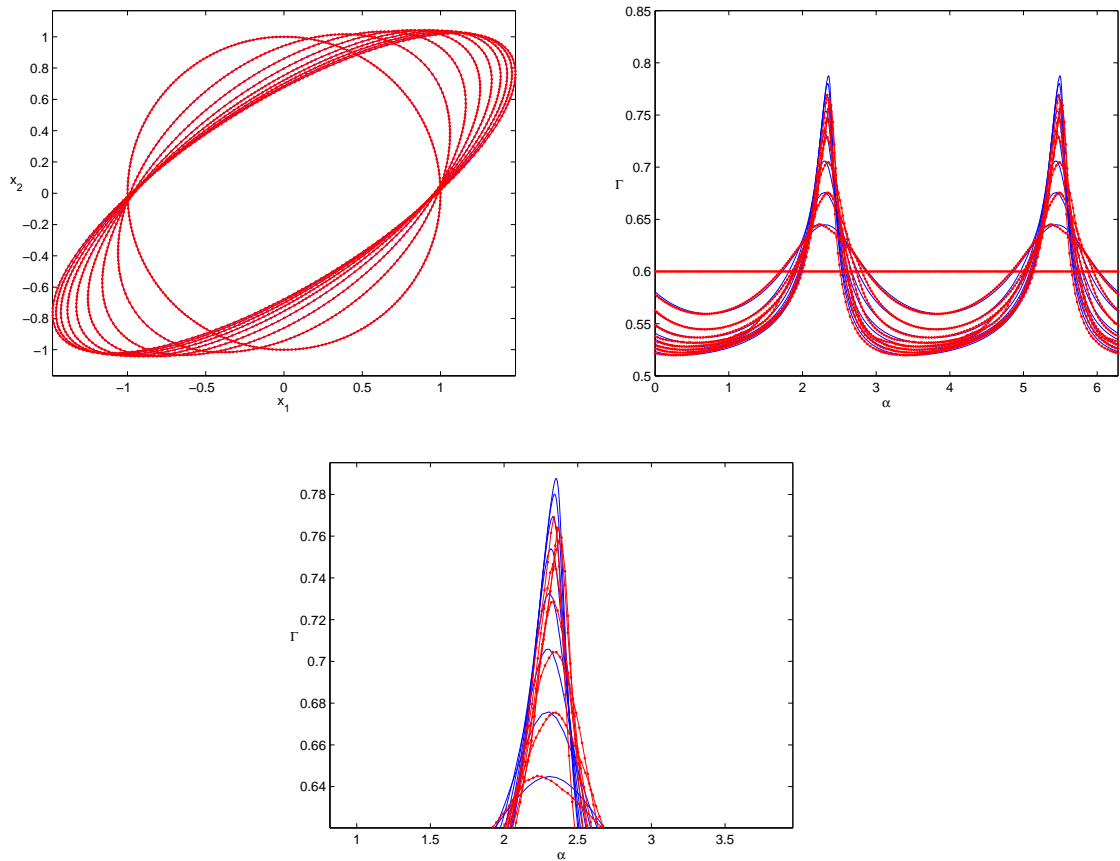


Figure 6.2 A return to Scenario 3 of Chapter 5. Comparison of simulation results using the Green's function method with simulation using the mesh-based method. The mesh-based method is shown by blue solid lines and the Green's function method is shown by red solid markers. The evolution of the bubble interface (upper left panel) and the surface surfactant concentration (upper right panel) are plotted from $t = 0$ to $t = 4.0$ in increments of 0.5. The lower panel gives a closeup of the spikes in Γ .

CHAPTER 7

CONCLUDING REMARKS AND FUTURE DIRECTIONS

In this dissertation, we have formulated a mathematical model for two-phase flow in the presence of soluble surfactant. In applications, the bulk Péclet number can be as large as 10^5 to 10^6 , so that a thin transition layer may form near a fluid interface in which the concentration gradient of dissolved surfactant is large. Successfully resolving the surfactant concentration in this slender layer is both difficult and computationally expensive when a traditional numerical method is applied. Following [7], the approach taken here is based on a leading order singular perturbation reduction of the conservation equation for dissolved surfactant. It is this leading order transition layer equation that is solved to find the dissolved surfactant concentration adjacent to the interface. The resulting equation can be solved numerically at relatively small cost since the singular perturbation rescaling implies that there is no large gradient of bulk surfactant concentration expected in the rescaled computational domain of the transition layer.

Two versions of the boundary integral equation for two-phase Stokes flow have been presented. To accurately solve the boundary integral equation, we maintain an equal arc length frame along the interface, which allows us to evaluate the resulting integrals with spectral accuracy. Chebyshev-Lobatto collocation points are introduced to discretize the computational domain of the transition layer in the direction normal to the interface. This enables spectral accuracy to be achieved in the normal direction with only a moderate number of marker points. All time-dependent quantities are updated using a second order time marching scheme.

The number of marker points is doubled when higher resolution for either the interface or the profile of the surface surfactant concentration is needed. Filter

techniques are applied to smooth the interface at each time step. The numerical method is overall spectrally accurate in space and of second order in time.

Various numerical examples have been given in Chapter 5 for different viscosity ratios, imposed far-field flows, initial conditions, and equilibrium partition coefficients, etc.

In Chapter 6, we have reported a newly-derived analytical solution to the equation for the bulk surfactant concentration in the transition layer. This is based on a Green's function representation which, in essence, solves for the spatial structure in the normal direction analytically and expresses the bulk-interface surfactant exchange term as a convolution integral over time. This makes possible a numerical method that is mesh-free in the normal direction. An algorithm for computing this solution has been developed and has led to faithful numerical simulations. We compare numerical results of the mesh-free method with the results of the mesh-based method of Chapter 5. Their consistency validates both methods and promises the potential for developing a faster version of the algorithm in the future.

From the numerical point of view, our future work may include implementation of the fast multipole method (FMM) to significantly speed up the solution of the boundary integral equation. This fast summation technique enables a boundary integral equation to be solved in only a small fraction of the CPU time that is taken when FMM is not implemented. It is expedient to employ such a fast algorithm especially when a parameter study is needed that requires a large number of runs.

The algorithm that has been proposed here to evaluate the Green's function solution for the transition layer equation is not highly efficient. To evaluate the convolution integral that appears in this solution, we have to update information along the particle paths at each time step and sum over the entire time history. Fast numerical algorithms for computing convolution integrals for the heat equation have been successfully developed in the last two decades, see for example [43, 21, 48, 49].

The similarity between the heat equation and the present transition layer equation suggests that, by analogy, there may be a fast numerical method for computing the convolution that appears here. Therefore, a faster version of the numerical algorithm for the Green's function solution is another promising direction for development of the numerical method.

Understanding the impact of surfactant solubility is important from both a physical and a practical point of view. Parameter studies should help us to explain properly how the evolution of a fluid interface with soluble surfactant differs from that either with insoluble surfactant or without surfactant, but these must now be left for future work.

APPENDIX A

SHERMAN-LAURICELLA FORMULATION: THE PHYSICAL QUANTITIES IN TERMS OF GOURSAT FUNCTIONS

In this appendix we give a derivation of the expressions for the pressure, velocity, vorticity, and the necessary terms in the rate of strain tensor in terms of Goursat functions. The results can also be found in [28] but are given there without derivation.

In the exterior region Ω , the Stokes equation and the incompressibility condition (2.7a) hold. For convenience, we repeat them here,

$$\nabla^2 \mathbf{u} = \nabla p, \tag{A.1a}$$

$$\nabla \cdot \mathbf{u} = 0. \tag{A.1b}$$

In the interior region Ω^i the corresponding equations are

$$\lambda \nabla^2 \mathbf{u}^i = \nabla p^i, \tag{A.2a}$$

$$\nabla \cdot \mathbf{u}^i = 0. \tag{A.2b}$$

It follows that expressions for flow quantities in the interior region are given by the same expressions that hold in the exterior region on replacing p by $\frac{p}{\lambda}$ and adding an i -superscript.

We introduce the stream function for the exterior flow $W(x_1, x_2)$, in terms of which the velocity components are

$$u_1 = W_{x_2}, \quad u_2 = -W_{x_1}, \tag{A.3}$$

and the incompressibility condition is satisfied automatically. Further, by substituting (A.3) into the curl of the Stokes equation (A.1a), we find that $W(x_1, x_2)$ satisfies the

biharmonic equation

$$\nabla^4 W = 0. \quad (\text{A.4})$$

Since $W(x_1, x_2)$ is biharmonic, it can be expressed in terms of Goursat functions $f(z)$ and $h(z)$, where $z = x_1 + ix_2$, [10]. That is,

$$W(x_1, x_2) = \text{Re}(\bar{z}f(z) + h(z)), \quad (\text{A.5})$$

or equivalently

$$W(x_1, x_2) = \frac{1}{2} \left(\bar{z}f(z) + h(z) + z\overline{f'(z)} + \overline{h(z)} \right). \quad (\text{A.6})$$

Let $h'(z) = g(z)$ for convenience, then

$$W_{x_1}(x_1, x_2) = \frac{1}{2} \left(f(z) + \bar{z}f'(z) + \overline{f'(z)} + z\overline{f''(z)} + g(z) + \overline{g(z)} \right), \quad (\text{A.7a})$$

$$W_{x_2}(x_1, x_2) = \frac{i}{2} \left(-f(z) + \bar{z}f'(z) + \overline{f'(z)} - z\overline{f''(z)} + g(z) - \overline{g(z)} \right). \quad (\text{A.7b})$$

Therefore, from (A.3) the velocity of the exterior flow is given by

$$-u_2 + iu_1 = W_{x_1} + iW_{x_2} = f(z) + z\overline{f''(z)} + \overline{g(z)}. \quad (\text{A.8})$$

The vorticity $q = \partial_{x_1} u_2 - \partial_{x_2} u_1$ is given in terms of the stream function $W(x_1, x_2)$ from (A.3) by

$$q = -\nabla^2 W. \quad (\text{A.9})$$

Further, it follows from (A.7a) and (A.7b) that

$$W_{x_1 x_1}(x_1, x_2) = \frac{1}{2} \left(2f''(z) + \bar{z}f'''(z) + 2\overline{f''(z)} + z\overline{f''''(z)} + g'(z) + \overline{g'(z)} \right) \quad (\text{A.10a})$$

$$W_{x_2 x_2}(x_1, x_2) = \frac{1}{2} \left(2f''(z) - \bar{z}f'''(z) + 2\overline{f''(z)} - z\overline{f''''(z)} - g'(z) - \overline{g'(z)} \right) \quad (\text{A.10b})$$

$$W_{x_1 x_2}(x_1, x_2) = \frac{i}{2} \left(\bar{z}f'''(z) - z\overline{f''''(z)} + g'(z) - \overline{g'(z)} \right). \quad (\text{A.10c})$$

Substituting (A.10a) and (A.10b) into (A.9) we find an expression for the vorticity in terms of $f(z)$ and $g(z)$, viz.

$$q = -4\text{Re}(f'(z)) . \quad (\text{A.11})$$

From (A.3) and (A.9), the components of (A.1a) imply that

$$q_{x_1} = p_{x_2} , \quad q_{x_2} = -p_{x_1} , \quad (\text{A.12})$$

that is, q and p satisfy the Cauchy-Riemann equations. Assuming that the first derivatives of q and p are also continuous, we see that q and p are the real and imaginary parts of an analytic function, and hence from (A.11) the exterior pressure is given by

$$p = -4\text{Im}(f'(z)) . \quad (\text{A.13})$$

The components e_{11} and e_{12} of the rate of strain tensor can be written in terms of $W(x_1, x_2)$ from (A.3) and then in terms of $f(z)$ and $g(z)$ from (A.10a) to (A.10c), to give

$$e_{11} = W_{x_1x_2} = \frac{i}{2} \left(\bar{z}f''(z) - z\overline{f''(z)} + g'(z) - \overline{g'(z)} \right) , \quad (\text{A.14a})$$

$$e_{12} = \frac{1}{2} (W_{x_2x_2} - W_{x_1x_1}) = -\frac{1}{2} \left(\bar{z}f''(z) + z\overline{f''(z)} + g'(z) + \overline{g'(z)} \right) . \quad (\text{A.14b})$$

Then we have

$$e_{11} + ie_{12} = -i \left(z\overline{f''(z)} + \overline{g'(z)} \right) , \quad (\text{A.15})$$

and since $e_{21} = e_{12}$ and $e_{11} = -e_{22}$, we have

$$e_{11} + ie_{12} = -e_{22} + ie_{21} . \quad (\text{A.16})$$

Table A.1 Expressions for Physical Quantities in the Exterior Region Ω and Interior Region Ω^i

quantity	exterior $z \in \Omega$	interior $z \in \Omega^i$
stream function	$W = Re(\bar{z}f(z) + h(z))$	$W^i = Re(\bar{z}f^i(z) + h^i(z))$
velocity	$u_1 + iu_2$ $= -i\left(f(z) + z\overline{f'(z)} + \overline{g(z)}\right)$	$u_1^i + iu_2^i$ $= -i\left(f^i(z) + z\overline{f^{i'}(z)} + \overline{g^i(z)}\right)$
vorticity	$q = -4Re(f'(z))$	$q^i = -4Re(f^{i'}(z))$
pressure	$p = -4Im(f'(z))$	$p^i = -4\lambda Im(f^{i'}(z))$
rate of strain tensor	$e_{11} + ie_{12}$ $= -e_{22} + ie_{21}$ $= -i\left(z\overline{f''(z)} + \overline{g'(z)}\right)$	$e_{11}^i + ie_{12}^i$ $= -e_{22}^i + ie_{21}^i$ $= -i\left(z\overline{f^{i''}(z)} + \overline{g^{i'}(z)}\right)$

Table A.1 summarizes all physical quantities associated with the exterior and interior flow regions in terms of the corresponding Goursat functions.

APPENDIX B

REMOVABLE SINGULARITIES AND CAUCHY PRINCIPAL VALUE INTEGRALS IN THE BOUNDARY INTEGRAL EQUATIONS

We consider two points y and x on the drop interface $\partial\Omega$, where x is fixed and y approaches x from either side. As described in Section 4.1.1, the interface $\partial\Omega$ can be parameterized by the renormalized arc length $\alpha \in [0, 2\pi)$, so that we can write $x = x(\alpha^*) = x_1(\alpha^*) + ix_2(\alpha^*)$ and $y = x(\alpha) = x_1(\alpha) + ix_2(\alpha)$ where α^* is fixed and $\alpha \rightarrow \alpha^*$. In this appendix, a prime denotes a derivative with respect to α , κ is the local curvature of $\partial\Omega$, and σ is the surface tension which depends on the surface surfactant concentration Γ (see (2.9)). Since Γ is a function of location along the interface $\partial\Omega$, we use $\sigma(\alpha)$ to denote its dependence on α . As in previous chapters, the arc length is denoted by s and we note that $s_\alpha = |x_\alpha|$.

Proof of (4.17a)

$$\begin{aligned} L_1 &= \lim_{y \rightarrow x} d \ln \frac{y-x}{\bar{y}-\bar{x}} \\ &= \lim_{y \rightarrow x} \left(\frac{y_\alpha}{y-x} - \frac{\bar{y}_\alpha}{\bar{y}-\bar{x}} \right) d\alpha \\ &= \lim_{\alpha \rightarrow \alpha^*} \frac{2i [x'_2(\alpha)(x_1(\alpha) - x_1(\alpha^*)) - x'_1(\alpha)(x_2(\alpha) - x_2(\alpha^*))]}{[x_1(\alpha) - x_1(\alpha^*)]^2 + [x_2(\alpha) - x_2(\alpha^*)]^2} d\alpha \end{aligned}$$

Using L'Hospital's rule twice, we have

$$\begin{aligned} L_1 &= \lim_{\alpha \rightarrow \alpha^*} \frac{i [x''_2(\alpha)(x_1(\alpha) - x_1(\alpha^*)) - x''_1(\alpha)(x_2(\alpha) - x_2(\alpha^*))]}{x'_1(\alpha)[x_1(\alpha) - x_1(\alpha^*)] + x'_2(\alpha)[x_2(\alpha) - x_2(\alpha^*)]} d\alpha \quad (\text{L'Hospital rule}) \\ &= \frac{i [x''_2(\alpha^*)x'_1(\alpha^*) - x''_1(\alpha^*)x'_2(\alpha^*)]}{x'^2_1(\alpha^*) + x'^2_2(\alpha^*)} d\alpha \quad (\text{L'Hospital rule again}) \\ &= \frac{i [x''_2(\alpha)x'_1(\alpha) - x''_1(\alpha)x'_2(\alpha)]}{[x'^2_1(\alpha) + x'^2_2(\alpha)]^{\frac{3}{2}}} \sqrt{x'^2_1(\alpha) + x'^2_2(\alpha)} d\alpha \\ &= -i\kappa s_\alpha d\alpha \quad \text{at } \alpha = \alpha^*. \end{aligned}$$

Proof of (4.17b)

$$\begin{aligned}
L_2 &= \lim_{y \rightarrow x} d \frac{y-x}{\bar{y}-\bar{x}} \\
&= \lim_{y \rightarrow x} \left(\frac{y_\alpha}{\bar{y}-\bar{x}} - \frac{\bar{y}_\alpha (y-x)}{(\bar{y}-\bar{x})^2} \right) d\alpha \\
&= \lim_{\alpha \rightarrow \alpha^*} \frac{y_\alpha (\bar{y}-\bar{x}) - \bar{y}_\alpha (y-x)}{(\bar{y}-\bar{x})^2} d\alpha \\
&= \lim_{\alpha \rightarrow \alpha^*} \frac{2i [x'_2(\alpha)(x_1(\alpha) - x_1(\alpha^*)) - x'_1(\alpha)(x_2(\alpha) - x_2(\alpha^*))]}{[(x_1(\alpha) - iy(\alpha)) - (x_1(\alpha^*) - iy(\alpha^*))]^2} d\alpha
\end{aligned}$$

Using L'Hospital's rule twice, we have

$$\begin{aligned}
L_2 &= \lim_{\alpha \rightarrow \alpha^*} \frac{i [x''_2(\alpha)(x_1(\alpha) - x_1(\alpha^*)) - x''_1(\alpha)(x_2(\alpha) - x_2(\alpha^*))]}{[x'_1(\alpha) - iy'(\alpha)] [(x_1(\alpha) - iy(\alpha)) - (x_1(\alpha^*) - iy(\alpha^*))]^2} d\alpha \quad (\text{L'Hospital rule}) \\
&= \frac{i [x''_2(\alpha^*)x'_1(\alpha^*) - x''_1(\alpha^*)x'_2(\alpha^*)]}{[x'_1(\alpha^*) - iy'(\alpha^*)]^2} d\alpha \quad (\text{L'Hospital rule again}) \\
&= \frac{i [x''_2(\alpha^*)x'_1(\alpha^*) - x''_1(\alpha^*)x'_2(\alpha^*)]}{[x'_1(\alpha^*)^2 + x'_2(\alpha^*)^2]^{\frac{3}{2}}} \frac{[x'_1(\alpha^*) + iy'(\alpha^*)]^2}{[x'_1(\alpha^*)^2 + x'_2(\alpha^*)^2]^{\frac{1}{2}}} d\alpha \\
&= -i\kappa \frac{y_\alpha^2}{s_\alpha} d\alpha \quad \text{at } \alpha = \alpha^*.
\end{aligned}$$

Proof of (4.17c)

$$\begin{aligned}
L_3 &= \lim_{y \rightarrow x} \frac{x-y}{\bar{x}-\bar{y}} ds(y) \\
&= \lim_{\alpha \rightarrow \alpha^*} \frac{x_\alpha(\alpha)}{\bar{x}_\alpha(\alpha)} ds(\alpha) \quad (\text{L'Hospital rule}) \\
&= \frac{y_\alpha}{y_\alpha} ds(\alpha) \quad \text{at } \alpha = \alpha^* \\
&= \frac{y_\alpha^2}{s_\alpha} d\alpha \quad \text{at } \alpha = \alpha^*.
\end{aligned}$$

Proof of (4.18)

We first consider $\int_{\partial\Omega} \frac{\sigma y_s}{y-x} dy$ by successively subtracting singular terms.

$$\begin{aligned}
& \int_{\partial\Omega} \frac{\sigma y_s}{y-x} dy \\
&= \int_{\partial\Omega} \frac{\sigma(\alpha) x_\alpha^2(\alpha)}{s_\alpha(\alpha) [x(\alpha) - x(\alpha^*)]} d\alpha \\
&= \int_{\partial\Omega} \frac{\sigma(\alpha) x_\alpha^2(\alpha)}{s_\alpha(\alpha)} \left[\frac{1}{x(\alpha) - x(\alpha^*)} - \frac{1}{x_\alpha(\alpha^*)(\alpha - \alpha^*)} \right] d\alpha \\
&\quad + \int_{\partial\Omega} \frac{1}{x_\alpha(\alpha^*)(\alpha - \alpha^*)} \left[\frac{\sigma(\alpha) x_\alpha^2(\alpha)}{s_\alpha(\alpha)} - \frac{\sigma(\alpha^*) x_\alpha^2(\alpha^*)}{s_\alpha(\alpha^*)} \right] d\alpha \\
&\quad\quad\quad + \frac{\sigma(\alpha^*) x_\alpha(\alpha^*)}{s_\alpha(\alpha^*)} \int_{\partial\Omega} \frac{1}{\alpha - \alpha^*} d\alpha \tag{B.1}
\end{aligned}$$

The last term in (B.1) is zero when the integral is evaluated in the sense of a Cauchy principal value integral. The integrands of the first two integrals in (B.1) appear singular as α tends to α^* but the singularities are removable, as seen taking the limit as $\alpha \rightarrow \alpha^*$, that is,

$$\begin{aligned}
& \lim_{\alpha \rightarrow \alpha^*} \frac{\sigma(\alpha) x_\alpha^2(\alpha)}{s_\alpha(\alpha)} \left[\frac{1}{x(\alpha) - x(\alpha^*)} - \frac{1}{x_\alpha(\alpha^*)(\alpha - \alpha^*)} \right] \\
&= \frac{\sigma(\alpha^*) x_\alpha^2(\alpha^*)}{s_\alpha(\alpha^*)} \cdot \left(-\frac{x_{\alpha\alpha}(\alpha^*)}{2x_\alpha^2(\alpha^*)} \right) = -\frac{\sigma(\alpha^*) x_{\alpha\alpha}(\alpha^*)}{2s_\alpha(\alpha^*)}, \tag{B.2}
\end{aligned}$$

$$\begin{aligned}
& \lim_{\alpha \rightarrow \alpha^*} \frac{1}{x_\alpha(\alpha^*)(\alpha - \alpha^*)} \left(\frac{\sigma(\alpha) x_\alpha^2(\alpha)}{s_\alpha(\alpha)} - \frac{\sigma(\alpha^*) x_\alpha^2(\alpha^*)}{s_\alpha(\alpha^*)} \right) \\
&= \frac{\sigma_\alpha(\alpha^*) x_\alpha(\alpha^*)}{s_\alpha(\alpha^*)} + \frac{2\sigma(\alpha^*) x_{\alpha\alpha}(\alpha^*)}{s_\alpha(\alpha^*)} - \frac{\sigma(\alpha^*) x(\alpha^*) s_{\alpha\alpha}(\alpha^*)}{s_\alpha^2(\alpha^*)}. \tag{B.3}
\end{aligned}$$

The last term in (B.3) vanishes when the equal arc length frame described in 4.1.1 is adopted, since $s_{\alpha\alpha} = 0$ everywhere along $\partial\Omega$. If we discretize the interface $\partial\Omega$ by M marker points that are equally spaced in arc length s and use the trapezoidal rule, a spectrally accurate quadrature is obtained by a combination of (B.1)-(B.3), [46], viz.

$$\int_{\partial\Omega} \frac{\sigma y_s}{y-x} dy = h \sum_{\substack{k=1 \\ k \neq j}}^M \frac{\sigma_k(x_\alpha)_k^2}{s_\alpha} \left(\frac{1}{x_k - x_j} \right) + \frac{h(\sigma_\alpha)_j(x_\alpha)_j}{s_\alpha} + \frac{3h\sigma_j(x_{\alpha\alpha})_j}{2s_\alpha}. \tag{B.4}$$

Now we turn to the evaluation of $\int_{\partial\Omega} \frac{\sigma y_s}{\bar{y} - \bar{x}} d\bar{y}$. The same strategy for desingularization leads to

$$\begin{aligned}
& \int_{\partial\Omega} \frac{\sigma y_s}{\bar{y} - \bar{x}} d\bar{y} \\
&= \int_{\partial\Omega} \frac{\sigma(\alpha) |x_\alpha(\alpha)|^2}{s_\alpha(\alpha)} \frac{1}{\bar{x}(\alpha) - \bar{x}(\alpha^*)} d\alpha \\
&= \int_{\partial\Omega} \frac{\sigma(\alpha) |x_\alpha(\alpha)|^2}{s_\alpha(\alpha)} \left[\frac{1}{\bar{x}(\alpha) - \bar{x}(\alpha^*)} - \frac{1}{\overline{x_\alpha(\alpha^*)}(\alpha - \alpha^*)} \right] d\alpha \\
&\quad + \int_{\partial\Omega} \frac{1}{\overline{x_\alpha(\alpha^*)}(\alpha - \alpha^*)} \left(\frac{\sigma(\alpha) |x_\alpha(\alpha)|^2}{s_\alpha(\alpha)} - \frac{\sigma(\alpha^*) |x_\alpha(\alpha^*)|^2}{s_\alpha(\alpha^*)} \right) d\alpha \\
&\quad + \frac{\sigma(\alpha^*) |x_\alpha(\alpha^*)|^2}{s_\alpha(\alpha^*) \overline{x_\alpha(\alpha^*)}} \int_{\partial\Omega} \frac{1}{\alpha - \alpha^*} d\alpha, \tag{B.5}
\end{aligned}$$

where the integral in the last term is zero since it is interpreted as a Cauchy principal value integral. The integrands in the first two integrals have the following limits as α goes to α^* ,

$$\lim_{\alpha \rightarrow \alpha^*} \frac{\sigma(\alpha) |x_\alpha(\alpha)|^2}{s_\alpha(\alpha)} \left[\frac{1}{\bar{x}(\alpha) - \bar{x}(\alpha^*)} - \frac{1}{\overline{x_\alpha(\alpha^*)}(\alpha - \alpha^*)} \right] = - \frac{\sigma(\alpha^*) \overline{x_{\alpha\alpha}(\alpha^*)} x_\alpha(\alpha^*)}{2s_\alpha(\alpha^*) \overline{x_\alpha(\alpha^*)}}, \tag{B.6}$$

$$\begin{aligned}
& \lim_{\alpha \rightarrow \alpha^*} \frac{1}{\overline{x_\alpha(\alpha^*)}(\alpha - \alpha^*)} \left(\frac{\sigma(\alpha) |x_\alpha(\alpha)|^2}{s_\alpha(\alpha)} - \frac{\sigma(\alpha^*) |x_\alpha(\alpha^*)|^2}{s_\alpha(\alpha^*)} \right) \\
&= \frac{\sigma(\alpha^*) x_{\alpha\alpha}(\alpha^*)}{s_\alpha(\alpha^*)} + \frac{\sigma(\alpha^*) \overline{x_{\alpha\alpha}(\alpha^*)} x_\alpha(\alpha^*)}{s_\alpha(\alpha^*) \overline{x_\alpha(\alpha^*)}} + \frac{\sigma_\alpha(\alpha^*) x_\alpha(\alpha^*)}{s_\alpha(\alpha^*)} - \frac{\sigma(\alpha^*) s_{\alpha\alpha}(\alpha^*) x_\alpha(\alpha^*)}{s_\alpha^2(\alpha^*)}, \tag{B.7}
\end{aligned}$$

where the last term is zero when s_α is constant along $\partial\Omega$. Substituting (B.6) and (B.7) into (B.5) we have the spectrally accurate quadrature

$$\int_{\partial\Omega} \frac{\sigma y_s}{\bar{y} - \bar{x}} d\bar{y} = h \sum_{\substack{k=1 \\ k \neq j}}^M \frac{\sigma_k |x_\alpha|_k^2}{s_\alpha} \left(\frac{1}{\bar{x}_k - \bar{x}_j} \right) + \frac{h((\sigma x_\alpha)_\alpha)_j}{s_\alpha} + \frac{h\sigma_j (\overline{x_{\alpha\alpha}})_j (x_\alpha)_j}{2s_\alpha(\overline{x_\alpha})_j}. \tag{B.8}$$

Finally, we verify (4.18) by summing (B.4) and (B.8).

REFERENCES

- [1] A. Acrivos. The breakup of small drops and bubbles in shear flows. *Annals of the New York Academy of Sciences*, 404:1–11, 1983.
- [2] S. Anna and H. Mayer. Microscale tipstreaming in a microfluidic flow focusing device. *Physics of Fluids*, 18:121512, 2006.
- [3] G. Baker and A. Nachbin. Stable methods for vortex sheet motion in the presence of surface tension. *SIAM Journal on Scientific Computing*, 19:1737–1766, 1998.
- [4] O. Basaran. Small-scale free surface flows with breakup: drop formation and emerging applications. *AIChE*, 48:1842–1848, 2002.
- [5] G. Batchelor. *An Introduction to Fluid Dynamics*. Cambridge University Press, Cambridge, 1967.
- [6] M. Booty and M. Siegel. Steady deformation and tip-streaming of a slender bubble with surfactant in an extensional flow. *Journal of Fluid Mechanics*, 544:243–275, 2005.
- [7] M. Booty and M. Siegel. A hybrid numerical method for interfacial fluid flow with soluble surfactant. *Journal of Computational Physics*, 229:3864–3883, 2010.
- [8] J. Buckmaster and J. Flaherty. The bursting of two-dimensional drops in slow viscous flow. *Journal of Fluid Mechanics*, 60:625–639, 1973.
- [9] C. Canuto, M. Hussaini, A. Quarteroni, and T. Zang. *Spectral Methods: Fundamentals in Single Domains*. Springer, Berlin, 2006.
- [10] G. Carrier, M. Krook, and C. Pearson. *Functions of A Complex Variable*. McGraw-Hill Book Company, New York, 1966.
- [11] C.-H Chang and E. Franses. Adsorption dynamics of surfactants at the air/water interface: a critical review of mathematical models, data, and mechanisms. *Colloids Surfaces A*, 100:1–45, 1995.
- [12] A. Dutt and V. Rokhlin. Fast Fourier transforms for nonequispaced data. *SIAM Journal on Scientific Computing*, 14:1368–1393, 1993.
- [13] A. Dutt and V. Rokhlin. Fast Fourier transforms for nonequispaced data, II. *Applied and Computational Harmonic Analysis*, 2:85–100, 1995.
- [14] D. Edwards, H. Brenner, and D. Wasan. *Interfacial Transport Processes and Rheology*. Butterworth-Heinemann, Boston, 1991.
- [15] J. Eggers. Nonlinear dynamics and breakup of free-surface flows. *Reviews of modern physics*, 69:865–929, 1997.

- [16] C. Eggleton, Y. Pawar, and K. Stebe. Insoluble surfactants on a drop in an extensional flow: a generalization of the stagnated surface limit to deforming interfaces. *Journal of Fluid Mechanics*, 385:79–99, 1999.
- [17] C. Eggleton, T. Tsai, and K. Stebe. Tip streaming from a drop in the presence of surfactant. *Physical review letters*, 87(4):048302, 2001.
- [18] A. Greenbaum, L. Greengard, and A. Mayo. On the numerical solution of the biharmonic equation in the plane. *Physica D*, 60:216–225, 1992.
- [19] L. Greengard, M. Kropinski, and A. Mayo. Integral equation methods for Stokes flow and isotropic elasticity in the plane. *Journal of Computational Physics*, 125:403–414, 1996.
- [20] L. Greengard and J. Lee. Accelerating the nonuniform fast Fourier transform. *SIAM Review*, 46:443–454, 2004.
- [21] L. Greengard and J. Strain. A fast algorithm for the evaluation of heat potentials. *Communications on Pure and Applied Mathematics*, 43:949–963, 1990.
- [22] B. Gustafsson, H. Kreiss, and J. Oliger. *Time Dependent Problems and Difference Methods*. Wiley, New York, 1995.
- [23] T. Hou, J. Lowengrub, and M. Shelley. Removing the stiffness from interfacial flows with surface tension. *Journal of Computational Physics*, 114:312–338, 1994.
- [24] F. Jin, N. Gupta, and K. Stebe. The detachment of a viscous drop in a viscous solution in the presence of a soluble surfactant. *Physics of Fluids*, 18:022103, 2006.
- [25] R. Krasny. A study of singularity formation in a vortex sheet by the point-vortex approximation. *Journal of Fluid Mechanics*, 167:65–93, 1986.
- [26] M. Kropinski. An efficient numerical method for studying interfacial motion in two-dimensional creeping flows. *Journal of Computational Physics*, 171:479–508, 2001.
- [27] M. Kropinski. Numerical methods for multiple inviscid interfaces in creeping flows. *Journal of Computational Physics*, 180:1–24, 2002.
- [28] W. Langlois. *Slow Viscous Flow*. Macmillan, New York, 1964.
- [29] M. Matalon, C. Cui, and J. K. Bechtold. Hydrodynamic theory of premixed flames: effects of stoichiometry, variable transport coefficients and arbitrary reaction orders. *Journal of Fluid Mechanics*, 487:179–210, 2003.
- [30] S. Mikhlin. *Integral Equations and Their Applications to Certain Problems in Mechanics, Mathematical Physics and Technology*. The MacMillan Company, New York, 1964.

- [31] W. Milliken and L. Leal. The influence of surfactant on the deformation and breakup of viscous drop: the effect of the surfactant solubility. *Journal of Colloid and Interface Science*, 166:275–285, 1994.
- [32] M. Muradoglu and G. Tryggvason. A front-tracking method for computation of interfacial flows with soluble surfactants. *Journal of Computational Physics*, 227:2238–2262, 2008.
- [33] C. Pozrikidis. *Boundary Integral and Singularity Methods for Linearized Viscous Flow*. Cambridge University Press, Cambridge, 1992.
- [34] C. Pozrikidis. Numerical studies of singularity formation at free surfaces and fluid interfaces in two-dimensional Stokes flow. *Journal of Fluid Mechanics*, 331:145–167, 1997.
- [35] D. Pullin. Numerical studies of surface-tension effects in nonlinear Kelvin-Helmholtz and Rayleigh-Taylor instability. *Journal of Fluid Mechanics*, 119:507–532, 1982.
- [36] A. Quere. Fluid coating on a fiber. *Annual Review of Fluid Mechanics*, 31:347–384, 1999.
- [37] J. Rallison. The deformation of small viscous drops and bubbles in shear flows. *Annual Review of Fluid Mechanics*, 16:45–66, 1984.
- [38] M. Siegel. Influence of surfactant on rounded and pointed bubbles in two-dimensional Stokes flow. *SIAM Journal on Applied Mathematics*, 59:1998–2027, 1999.
- [39] M. Siegel. Cusp formation for time-evolving bubbles in two-dimensional Stokes flow. *Journal of Fluid Mechanics*, 412:227–257, 2000.
- [40] I. Stakgold. *Green's Functions and Boundary Value Problems*. Wiley, New York, 1979.
- [41] H. Stone. Dynamics of drop deformation and breakup in viscous fluids. *Annual Review of Fluid Mechanics*, 26:65–102, 1994.
- [42] H. Stone and L. Leal. The effects of surfactants on drop deformation and breakup. *Journal of Fluid Mechanics*, 220:161–186, 1990.
- [43] J. Strain. Fast adaptive methods for the free-space heat equation. *SIAM Journal on Scientific Computing*, 15:185–206, 1994.
- [44] S. Tanveer and G. Vasconcelos. Time-evolving bubbles in two-dimensional Stokes flow. *Journal of Fluid Mechanics*, 301:325–344, 1995.
- [45] G. Taylor. The formation of emulsions in definable fields of flow. *Proceedings of the Royal Society of London Series A*, 146:501–523, 1934.
- [46] L. Trefethen. *Spectral Methods in MATLAB*. Society for Industrial and Applied Mathematics, Philadelphia, PA, 2000.

- [47] R. van der Sman and S. van der Graaf. Diffuse interface model of surfactant adsorption onto flat and droplet interfaces. *Rheologica acta*, 46:3–11, 2006.
- [48] S. Veerapaneni and G. Biros. A high-order solver for the heat equation in 1d domains with moving boundaries. *SIAM Journal on Scientific Computing*, 29:2581–2606, 2007.
- [49] S. Veerapaneni and G. Biros. The Chebyshev fast gauss and nonuniform fast Fourier transforms and their application to the evaluation of distributed heat potentials. *Journal of Computational Physics*, 227:7768–7790, 2008.
- [50] H. Wong, D. Rumschitzki, and C. Maldarelli. On the surfactant mass balance at a deforming fluid interface. *Physics of Fluids*, 8:3203–3204, 1996.
- [51] J. Yao and S. Stewart. On the dynamics of multi-dimensional detonation. *Journal of Fluid Mechanics*, 309:225–275, 1996.
- [52] J. Zhang, D. Eckmann, and P. Ayyaswamy. A front tracking method for a deformable intravascular bubble in a tube with soluble surfactant transport. *Journal of Computational Physics*, 214:366–396, 2006.